To bind or not to bind

DNA mediated multivalent interactions lead to superselectivity

Linne, C.

DOI
10.4233/uuid:d2dbc4aa-02f5-43a1-a48c-b7ba1ad8ad67

Publication date
2022

Document Version
Final published version

Citation (APA)
Linne, C. (2022). *To bind or not to bind: DNA mediated multivalent interactions lead to superselectivity*. [Dissertation (TU Delft), Delft University of Technology]. https://doi.org/10.4233/uuid:d2dbc4aa-02f5-43a1-a48c-b7ba1ad8ad67

TO BIND OR NOT TO BIND

DNA MEDIATED MULTIVALENT INTERACTIONS LEAD TO SUPERSELECTIVITY

TO BIND OR NOT TO BIND

DNA MEDIATED MULTIVALENT INTERACTIONS LEAD TO SUPERSELECTIVITY

Dissertation

for the purpose of obtaining the degree of doctor
at Delft University of Technology
by the authority of the Rector Magnificus prof.dr.ir. T.H.J.J. van der Hagen
chair of the Board for Doctorates
to be defended publicly on
Monday 11 April 2022 at 10:00 o'clock

by

Christine LINNE

Master of Science in Physics
Georg August Universität Göttingen, Germany
Born in Oldenburg, Germany

The dissertation has been approved by the promotors.

promotor: Dr. D. J. Kraft
copromotor: Dr. ir. L. Laan

Composition of the doctoral committee:

Rector Magnificus,	chairperson
Dr. D. J. Kraft	Leiden University
Dr. ir. L. Laan	Delft University of Technology
Independent members:	
Prof. dr. D. Frenkel	University of Cambridge
Dr. L. Di Michele	University of Cambridge
Prof. dr. A. M. Dogterom	Delft University of Technology
Prof. dr. C. Dekker	Delft University of Technology
Reserve member:	
Dr. M.-E. Aubin-Tam	Delft University of Technology
Other member:	
Dr. J. Zwanikken	Delft University of Technology

Dr. J. Zwanikken has contributed greatly to the preparation of this dissertation.

Keywords: colloids, DNA nanostars, membrane, diffusion

Printed by: Gildeprint

Front & Back: Tobias Uhlig

Casimir PhD Series, 2022-06

ISBN 978-90-8593-517-9

An electronic version of this dissertation is available at
http://repository.tudelft.nl/.

CONTENTS

SUMMARY

To bind two entities together, an attractive interaction is needed. In biological systems, such interactions are often between ligands and receptors. But this interaction constantly breaks and forms because it is (too) weak. To ensure a lasting bond, the system can form multiple weak bonds that form an overall strong bond – similar to velcro. An interesting feature of a weak multivalent system is the sharp discrimination between surfaces based on receptor density. That means that when multivalent particles encounter surfaces with the specific receptor but different densities, they will most likely bind to the surface with the highest density, because it has the highest binding probability. This phenomenon is called superselectivity and emerges from the large entropic contribution in a multivalent system: The more ligands and receptors are involved in the binding, the more possibilities the system has to form a bond and hence a large entropy. In this thesis we investigate how the interaction strength and entropy influences superselective binding. In doing so, we study superselective binding of microparticles with hundreds of interactions and, additionally, particles with only few interactions of the size of nanometers.

First, we looked at a system with fully mobile ligands and receptors, where hundreds of interactions participate in the bond. **Chapter 2** describes an experimental model system consisting of micrometer sized spherical particles that can bind to a target surface. DNA molecules mediate the interactions between particle and surface with their specific basepair matching. A fluorescent molecule on each DNA strand allows for the visualization of the receptor and ligand interactions, because we only detect a signal when receptor and ligand bind. We test how many particles can bind for different interaction strength between ligand and receptor. We find that the system becomes more superselective, the weaker the interactions between the individual receptor and ligand.

This was the first time to directly visualize a multivalent bond in a superselective system on the molecular level. The possibility to locate the DNA between the particle and surface made it possible to investigate the formation of the bond and the bond itself. In **chapter 3**, we visualize and track the receptor and ligand recruitment towards the colloid-surface contact area during bond formation. We observe that particles bound to the surface can still diffuse. But this motion depends on the interaction strength and the number of interacting ligand-receptor pairs in the bond. We show that the particle motion reduces with increasing number of interactions in the contact area.

After intensive study of a multivalent system with hundreds of interactions, we introduce in **chapter 4** a DNA construct on the nanoscale. The construct is a DNA "nanostar" that results from the complementary interactions between multiple DNA strands, forming a star-like shape with multiple branches (arms). Each arm has a free end that can interact with a complementary DNA strand. We use the DNA nanostar to study superselectivity for a precisely defined number of $(1-10)$ interactions. In doing so, each DNA nanostar has a fluorescent molecule such that we can visualize its binding to a sur-

face covered with receptors. We find that the DNA nanostars can bind superselectively and that the superselectivity increases with weaker interactions. The superselectivity increases even more when the surface contains DNA that cannot specifically bind to the DNA nanostars. This observation indicates that there seems to be an additional binding mode that binds the DNA nanostars to the surface, which has a strong impact on the superselectivity of the system.

In **chapter 5**, we investigate the motion of receptors inside a membrane. We observe that the receptor motion reduces with increasing number of biomolecules integrated in the membrane. Moreover, after adding DNA nanostars to the system, we observe a clear decrease in receptor motion, because the binding to the nanostar limits the receptor diffusion.

Alltogether, the results in this thesis show that a large entropy and weak interactions are necessary for superselective binding. The insights gained in this thesis will hopefully help to improve the design of drugs, where the precise targeting of surfaces is crucial.

SAMENVATTING

Om twee objecten samen te binden is een attractieve interactie nodig. In biologische systemen zijn deze attractieve interacties vaak tussen liganden en receptoren. Maar deze binding wordt herhalend gevormd en weer verbroken wanneer zij (te) zwak is. Om toch een blijvende binding aan te gaan, kan het systeem meerdere zwakke bindingen gebruiken die samen sterk zijn - zoals bijvoorbeeld bij klittenband. Een deeltje is multivalent als het meerdere liganden heeft en daarmee aan meerdere receptoren op een oppervlakte bindt. Een interessante eigenschap van multivalent deeltjes met zwakke bindingen is hun scherpe onderscheidsvermogen tussen oppervlakken waarvan de dichtheid van receptoren verschilt. Dit betekent dat een multivalent deeltje bij voorkeur aan het oppervlak met het hoogste aantal receptoren bindt, omdat daar de kans voor binding exceptioneel hoog is. Dit fenomeen wordt superselectiviteit genoemd en is een gevolg van een groot entropisch effect in multivalente systemen: het aantal mogelijkheden, en daarmee de kans, om te binden neemt toe als meer liganden en receptoren onderdeel zijn van een system. In deze dissertatie bestuderen we hoe superselectiviteit van systemen wordt beïnvloed door de sterkte van interacties en de entropie van het systeem. Daarvoor bestuderen we de superselectiviteit van deeltjes met honderden interacties ter grootte van micrometers en ook deeltjes met slechts enkele interacties ter grootte van nanometers.

Als eerste hebben we een systeem met mobiele liganden en receptoren bestudeerd, waar honderden interacties samen de binding vormen. **Hoofdstuk 2** beschrijft een experimenteel modelsysteem met ronde deeltjes op de schaal van een micrometer die aan een oppervlakte kunnen binden. De binding tussen het deeltje en oppervlak komt tot stand door de specifieke interacties van DNA strengen die basenparen vormen. Door een fluorescerend molecuul op elke DNA streng kunnen we de specifieke interacties tussen de receptor en ligand met een microscoop zien, omdat deze alleen fluoresceren als receptor en ligand aan elkaar gebonden zijn. We testen dan het aantal deeltjes dat kan binden voor variërende sterktes van de interactie tussen ligand en receptor. We ontdekten dat het systeem meer superselectief wordt als de interacties tussen receptoren en liganden zwakker zijn.

Deze experimenten maakten voor de eerste keer een multivalente binding in een superselectief systeem zichtbaar. Het kunnen observeren van de verdeling van DNA tussen het deeltje en oppervlakte maakte het mogelijk om het ontstaan van de verbinding en de verbinding zelf te bestuderen. In **hoofdstuk 3** volgen en visualiseren we de accumulatie van receptoren en liganden in het contactgebied tussen het deeltje en oppervlak tijdens het ontstaan van de binding. We ontdekten dat deeltjes die aan het oppervlakte gebonden zijn zich nog steeds over het oppervlak kunnen bewegen. Maar deze beweging hangt af van de sterkte en het aantal interacties in de binding. We demonstreren bijvoorbeeld dat de beweging van deeltjes afneemt als het aantal interacties of hun sterkte toeneemt.

Na deze studie over multivalente systemen met honderden interacties, introduceren

we in **hoofdstuk 4** een DNA constructie op de schaal van een nanometer. De constructie is een DNA "nanosterretje", dat gebruik makend van de complementaire interacties tussen meerdere DNA strengen een stervormig construct vormt met verschillende aftakkingen (armen). Iedere arm heeft een einde dat vrij is om interacties met andere moleculen aan te gaan. We gebruiken het nanosterretje om superselectiviteit te bestuderen voor een precies gedefinieerd aantal (1 tot 10) verbindingen. Daarvoor heeft elk nanosterretje een fluorescerend molecuul dat alleen fluoresceert als het gebonden is aan de specifieke receptoren op een oppervlak. We ontdekten dat de nanosterretjes superselectief kunnen binden en dat de superselectiviteit toeneemt bij zwakkere interacties. De superselectiviteit neemt verder toe als het oppervlak ook DNA bevat dat niet aan het nanosterretje kan binden. Tot slot lijkt het erop dat de nanosterretjes ook op een tot nu toe onbekende manier aan het oppervlakte binden, en deze onbekende manier van binden heeft een grote invloed op de superselectiviteit van het system.

In **hoofdstuk 5** bestuderen we de beweging van receptoren in een membraan. We zien dat de mobiliteit van receptoren vermindert als het aantal biomoleculen in het membraan toeneemt. Na het toevoegen van nanosterretjes aan het oppervlak neemt de beweging van gebonden receptoren in het membraan af, omdat deze nu ook vast zitten aan het nanosterretjes.

Samen laten deze observaties zien dat een grote entropie en zwakke interacties nodig zijn voor een superselectieve binding. De bevindingen in deze dissertatie kunnen worden gebruikt om het ontwerp te verbeteren van medicijnen waarvoor binding aan het juiste oppervlak van groot belang is.

1

INTRODUCTION

As little kids we learned about shapes and forms. With puzzles as illustrated in Fig. 1.1a we trained our understanding of different forms and after some frustration accepted that the square does not fit into the round opening. This specificity plays an important role in interactions at the molecular level too, where receptors and ligands follow the "lock" and "key" metaphor [1]: two complementary geometric shapes that fit can bind, see Fig. 1.1b. Depending on the situation, ligand and receptor refers to different components in the system. Here, we refer to ligands as the binding sites on an object that target receptors on a different object. These objects can have different geometries and sizes: e.g a spherical particle coated with ligands, which can bind to receptors on a surface, see Fig. 1.1c. A particle selectively targets the surface when it recognizes the right receptor type and thus does not distinguish between the number of receptors. Let us complicate the system by introducing eight ligands of the same type on the particle, see Fig. 1.1d. In addition, this multivalent particle can feature different binding strengths. Either every interaction is weak, similar to velcro where individual weak interactions form a strong bond, see Fig. 1.1e. Or the interactions can be strong as super glue. The definition of strong and weak is not definite. Generally, van der Waals and hydrogen-bonds govern the interaction strength between ligands and receptors [2, 3]. Therefore, typical interaction strength ranges from weak to strong are a few $-k_BT$ up to $-20\ k_BT$ [4, 5].

Now, let's consider that the particle has a choice between a surface with a low or a high density of receptors, as shown in Fig. 1.1f. Where does the multivalent particle bind to? Does it make a difference if the interactions are strong or weak? If the interactions are strong, one single bond is enough to bind the multivalent particle, similar to a monovalent particle, and hence the particle has a high binding probability to both surfaces. But weak multivalent particles have the unique property that their binding probability increases significantly at a specific receptor density. This increase can almost be like an on-off behavior and is known as superselectivity [6]. In the following, we want to take the reader into the world of weak interactions and multivalency in biology and explain this interesting phenomena called superselectivity in more detail. This thesis unravels the strength of weak interactions and concludes that strong is not always better.

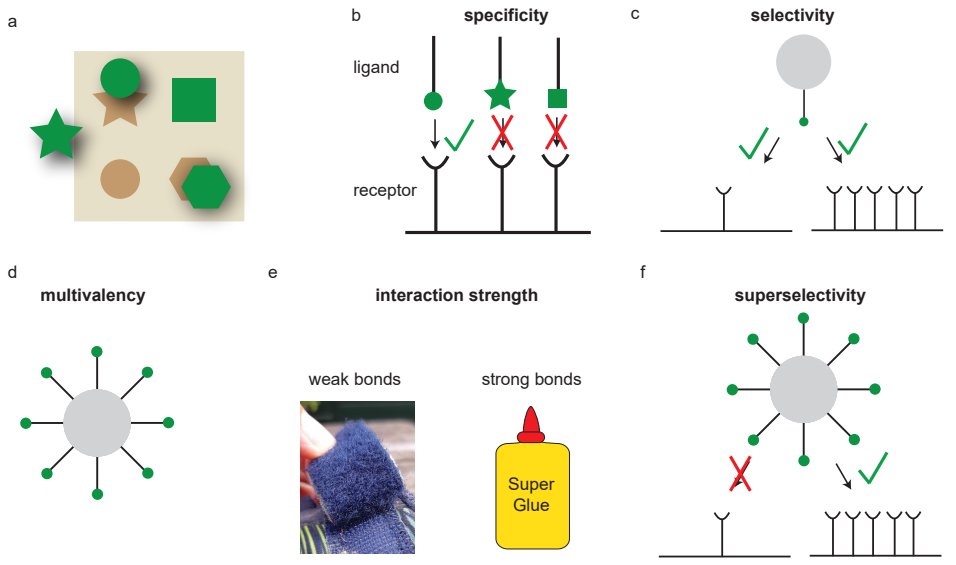

Figure 1.1: **Motivation.** a) The shapes only fit into the matching openings. b) Matching receptors and ligands mediate specific interactions in biology. c) A particle with one ligand that matches a receptor type can select for surfaces with that specific receptor. d) Multivalent particle features eight ligands of the same type on its surface. e) On the one hand, receptor and ligand interactions can be weak and reversible, comparable to velcro: Many weak interactions form an overall strong bond. On the other hand, the interactions can be strong and irreversible, similar to super glue: One small drop is enough to adhere two surfaces together. Copyright 2021 Liedewij Laan. f) A weak multivalent particle distinguishes sharply between surfaces based on receptor density, known as superselectivity.

1.1. MULTIVALENT INTERACTIONS IN BIOLOGICAL SYSTEMS

Multivalent interactions between two surfaces [10] are involved in many biological processes: polarity establishment [11], antibodies [12, 13], cell-cell adhesion [7, 14, 15], proteins [9, 16–19] and virus-host invasion [20, 21], see Fig. 1.2a-c.

Cell-cell adhesion is crucial for the formation of tissues and organs. The size of a cell is typically on the order of a micrometer and their surface is covered with adhesion mediating proteins, see Fig. 1.2a. As a result, the final bond consists of many interaction sites in the contact area. Moreover, cells often have a fluidic membrane that provides full mobility of receptors. This property leads to receptor clustering upon binding, inducing signal transduction [15, 22] or transport along the cell membrane [23].

On the nanoscale, multivalent binding occurs when virus particles target and invade host cells for replication of its genome. Compared to cell-cell adhesion, the superselective targeting involves only a few ligand and receptor interactions. In addition, the small number of interaction sites allows the virus to diffuse on the cell surface prior to uptake [20]. The uptake into the cell is governed by different mechanisms, depending on the virus type [24]. Influenza viruses internalize by endocytosis: The virus particle is wrapped by the cell membrane and enters the cell. The initiation of endocytosis is a result of receptor clustering induced by multivalent virus interactions [25].

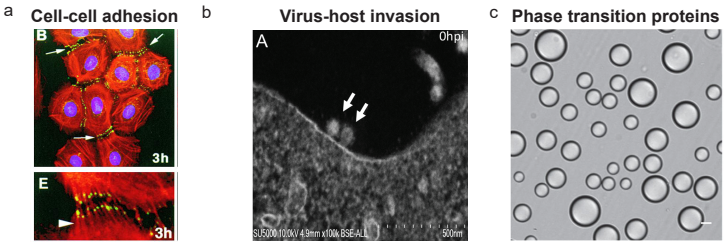

Figure 1.2: **Multivalency in biology.** a) Specific receptors mediate the adhesion between epithelial cells. Reprinted from [7], with permission from Elsevier. b) Virus particles superselectively target cells before internalization. Adapted from [8] (CC BY 4.0). c) The multivalent nature of proteins can lead to phase transition. Reprinted by permission from Springer Nature [9], copyright Springer Nature 2012.

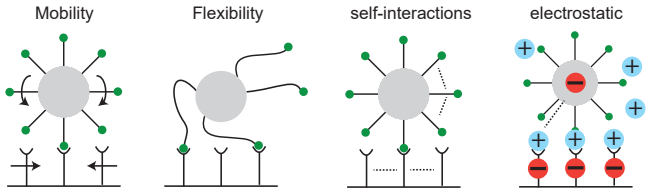

Figure 1.3: **Physical properties of ligands and receptors.** a) Mobile receptors and ligands that diffuse towards the contact area to increase the number of bonds. b) The longer and more flexible the ligands are, the more freely they can explore space and reach receptors in close proximity. c) In some systems, receptors and ligands can self-interact (dashed line). d) Ions that are essential for biological systems can adsorb to charged ligands and receptors leading to aspecific interactions.

The multivalent systems presented so far mediate interactions via receptors and ligands. If we zoom into the structure of a receptor or ligand, we note that they themselves typically consist of multidomain proteins, which can be multivalent as well [16, 26]. Proteins are involved in many processes inside the cell and hence a high specificity is important to recognize the right molecules. The recognition of specific proteins is crucial for ubiquitylation, where proteins are labeled with ubiquitin to trigger signals in the cell[19]. In addition to high selectivity, a high affinity is needed, which is usually accomplished by many weak interactions rather than by one strong interaction. This multivalent behavior can also lead to liquid-liquid phase transitions in protein systems [9, 18], see Fig. 1.2c. This interesting observation can explain the formation of subcellular compartments. To study multivalent effects on the molecular scale, theoretical work provides exciting insights into the binding dynamics, by taking experimental monovalent binding kinetics and expanding it to multivalency [17]. So far, mostly theoretical studies provide insights in the multivalent nature of protein binding. Experimental measurements with the required spatial and temporal resolutions are challenging, especially under native conditions. Proteins are very complex in their shapes and their interactions are highly dynamic, which makes it difficult to measure experimentally. There is great interest in the design of engineered proteins for use in targeted therapy. However, how to achieve a high specificity in protein-protein interactions is not well understood. Therefore, it is

important to expand experimental model systems to investigate selectivity with few interactions.

These examples show that multivalency can occur on different length scales: particles can be nanometer or micrometer in size and hence the number of interacting ligands and receptors can range from a few to up to hundreds. Furthermore, physical properties of the ligands and receptors have an impact on the multivalent character, see Fig. 1.3. Receptors and ligands that are integrated in surfaces with fluidic properties can freely diffuse and accumulate at the particle-surface contact area. The flexibility of ligands and receptors sets the space that they can explore in space before binding [27]. In addition to specific ligand and receptor interactions, it can occur that the binding sites are self-interacting, which can hinder the particle from binding due to initial bond-breaking before the ligand can bind to a receptor [28]. Similar to self-interactions, ions in solution can lead to aspecific binding caused by bridging effects [29]. This section has presented multivalent binding in biological systems. Next, we present the underlying theory for superselectivity.

1.2. SUPERSELECTIVITY

Only multivalent particles can sharply discriminate between surfaces based on receptor density. A particle that features more than one binding site can bind in more than one way, i.e. with different numbers and combinations of its binding sites. The more ligands and receptors are involved in the bond, the larger the combinatorial factor (combinatorial entropy) and the more favorable binding will occur. Apart from the entropic gain, the bond formation has to compensate for entropic losses [27]. This entropy is the sum of entropies with respect to the receptor, ligand and after receptor-ligand binding. Several studies have developed a theoretical description of the entropic contributions in a multivalent system for surface mobile receptors S_R and ligands S_L on spherical particles [30, 31]. They define the entropies as surface ratios concerning the bond area A_b, where ligands and receptors interact:

$$S_{R/L} = \mathrm{k_B} \log\left(\frac{\mathrm{A_b}}{\mathrm{A_{R/L}}}\right), \tag{1.1}$$

where $\mathrm{k_B}$ is the Boltzmann constant, $A_{R/L}$ is the surface area that the receptor/ligand can explore if unbound. That means that these entropies represent the cost to localize a receptor or ligand, given a certain area. The cost after bond formation due to hindrance in motion after binding is:

$$\Delta S^{conf} = \mathrm{k_B} \log\left(\rho_0 \mathrm{L A_b}\right), \tag{1.2}$$

where ρ_0 is a reference concentration and L is the ligand/receptor length. Finding the right interplay of enthalpy and entropy is important to obtain a superselective system. In the following, we will present the theory developed by Frenkel and coworkers [6] that demonstrates the design rules for superselectivity. First, we present the theory described in terms of chemical rate constants and subsequently describe the same system using statistical physics. Although, both perspectives describe the same system, they provide different insights into the parameters of the system.

Chemical kinetics Reversible ligand and receptor binding can be expressed by an equilibrium rate function with the on-rate k_{on} describing the bond formation and the off-rate k_{off} describing the bond breaking rate, see Fig. 1.4a. If the association constant $K_A = \frac{k_{on}}{k_{off}}$ is large, the receptors and ligands have a high affinity, and hence, a higher binding probability. Increasing the receptor density on a surface smoothly increases the binding probability, see Fig. 1.4a.

A well known model for the adsorption and binding probability Θ of a monovalent particle is the Langmuir isotherm:

$$\Theta = \frac{\rho K_A}{1 + \rho K_A}, \tag{1.3}$$

where ρ is the concentration of particles in solution. Increasing the number of ligands k on the particle changes the adsorption from one-step adsorption to multiple steps. After forming the first bond, the particle can form subsequent bonds with receptors in close proximity, see Fig. 1.4a. The subsequent bond formation is described by the equilibrium constant K_{intra}, which does not account for the number of ligands. To describe the combinatorial effects in multivalent binding, we introduce the avidity equilibrium constant K_A^{av} [32] that contains multiple affinities and describes an ensemble of interactions:

$$K_A^{av} \approx \frac{K_A}{K_{intra}} \left[(1 + \sigma_R K_{intra})^k - 1 \right], \tag{1.4}$$

where σ_R is the receptor density and k is the number of ligands. The expression within the squared brackets accounts for the bond formation on the surface once the particle has formed the first bond. Now, the binding probability does not only depend on K_A, but also on K_{intra}, giving it a characteristic sigmoidal shape with a sharp transition from unbound to bound, see Fig. 1.4b. How sharp this transition becomes depends on the particle concentration ρ, the number of ligands k and the interaction strength K_A. To quantify the selectivity α, we compute the relative change in Θ with σ_R, which resembles the slope of Θ on a log-log scale:

$$\alpha = \frac{d \ln \Theta}{d \ln \sigma_R}. \tag{1.5}$$

A system is superselective if $\alpha > 1$ and the highest selectivity can be achieved by lowering ρ and K_A, while increasing k. As a result, the ideal superselective particle has many binding sites that are as weak as possible.

Statistical physics The derivation of the adsorption of a multivalent particle can also be done with a statistical physics ansatz [6]:

$$\Theta = \frac{qZ}{1 + qZ}, \tag{1.6}$$

where q is the activity of the system, which scales with the particle concentration ρ and Z is the state partition function. The state partition function includes all possible binding states of an individual multivalent particle and for $\sigma_R >> k$ can be described with:

$$Z = (1 + \sigma_R \exp(-\Delta G_{bond} / k_B T))^k - 1, \tag{1.7}$$

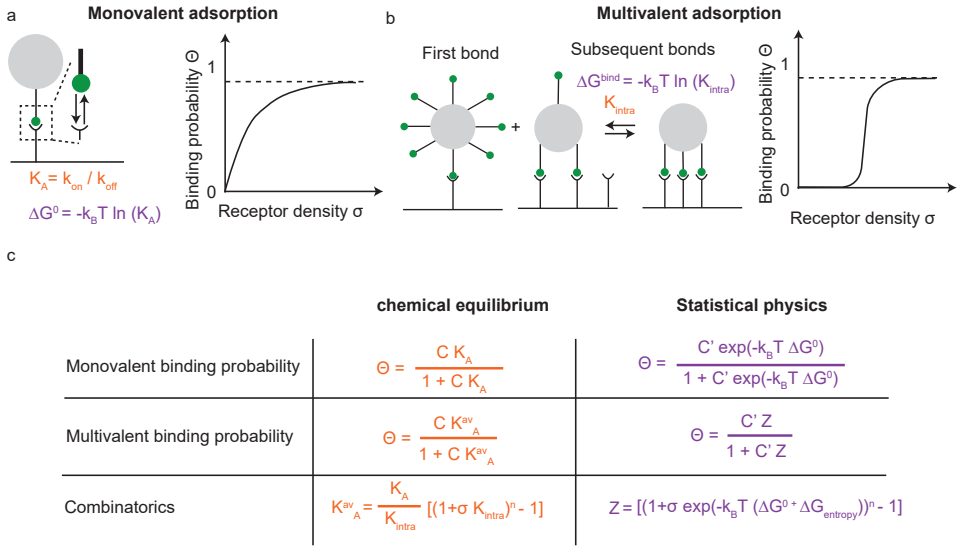

	chemical equilibrium	Statistical physics
Monovalent binding probability	$\Theta = \frac{C K_A}{1 + C K_A}$	$\Theta = \frac{C' \exp(-k_B T \Delta G^0)}{1 + C' \exp(-k_B T \Delta G^0)}$
Multivalent binding probability	$\Theta = \frac{C K^{av}_A}{1 + C K^{av}_A}$	$\Theta = \frac{C' Z}{1 + C' Z}$
Combinatorics	$K^{av}_A = \frac{K_A}{K_{intra}} [(1+\sigma K_{intra})^n - 1]$	$Z = [(1+\sigma \exp(-k_B T (\Delta G^0 + \Delta G_{entropy}))^n - 1]$

Figure 1.4: **Variables for model.** Parameters to describe a mathematical model for monovalent (a) and multivalent (b) adsorption. c) The resulting equations can be translated between chemical equilibrium constants (orange) and statistical physics (purple) with the relation $K = \exp(-\Delta G/k_B T)$.

where ΔG_{bond} is the binding free energy and includes the enthalpic ΔG^0 and entropic contributions $\Delta G_{entropy}$. In this thesis we look at particles adsorbing to surfaces, where the surface area and hence the number of receptors is much larger compared to the number of ligands, which is why Eq. 1.7 is valid in the subsequent chapters. With the relation $K = \exp(-\Delta G/k_B T)$ the statistical mechanics terms translate into chemical equilibrium constants, see Fig. 1.4c.

1.3. MULTIVALENT EXPERIMENTAL MODEL SYSTEMS

During the past years various experimental model systems have been introduced to study superselectivity. Because superselectivity is very sensitive to the systems parameters like interaction strength and entropic contributions, a high experimental control of the number of binding sites and their enthalpy is needed.

The first experimental model system that provided insights in the predicted design rules of a superselective system was multivalent polymer adsorption [33, 34]. The modification of polymers with hyaluron (HA) that bind to CD44 surface receptors allowed for the tunability of various system parameters that were predicted from the model to influence the selectivity. By using quartz crystal microbalance measurements they could precisely measure the polymer surface adsorption. By varying systems parameters, they

demonstrated that the right polymer concentration, interaction strength and number of binding sites can significantly increase the superselectivity. Another example of an ex-

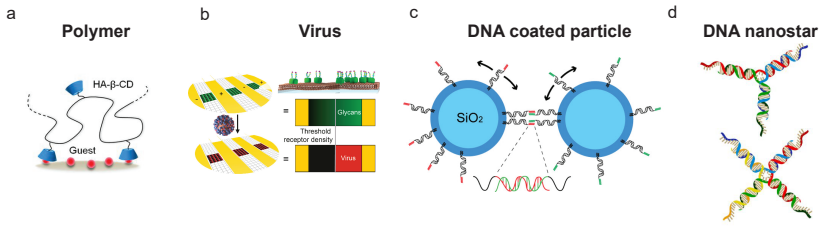

Figure 1.5: **Experimental model systems.** a) Polymer surface adsorption induced by hyaluron and CD44 interactions. Adapted from [34]. b) Virus particles superselectively bind to glycocalyx coated surfaces. Reprinted with permission from [35]. Copyright 2021 American Chemical Society. c) Particles with surface mobile DNA linkers. Particles with the complementary DNA sequence can interact. Reprinted with permission from [36]. Copyright 2013 American Chemical Society. d) Star shaped junctions of DNA strands. Each arm features a single stranded overhang that allows for hybridization with the complementary sequence. Adapted from [37].

perimental multivalent model system to study superselectivity, which occurs in nature, is virus particles [21, 35]. The system consists of influenza A virus particles where adhesion is mediated by the surface proteins hemagglutinin and neuraminidase interacting with the glycocalyx. The binding itself is a very dynamic and complex process and the exact number of interactions between virus and cell surface receptors is unknown [20]. The multivalent interactions of the virus particle makes it superselective with values of approximately $\alpha = 11$ [21]. This selectivity is remarkable as the polymer model system only reached maximum selectivities close to 3. This difference in selectivity shows that nature uses additional tools that are not yet captured by current experimental model systems. In the following, we will present two well established experimental model systems based on Deoxyribonucleic acid (DNA) interactions, which are used in this thesis.

DNA functionalised particles DNA is a powerful tool to use as a receptor and ligand system, see Fig. 1.5c. DNA consists of the four basepairs Guanine (G), Adenine (A), Thymine (T) and Cytosine (C), where G specifically binds to C and A to T, known as Watson-Crick pairing. By designing a single stranded DNA (ssDNA) and its complementary sequence, they can hybridize and form the characteristic helical shape. By changing the length of the ssDNA, the flexibility can be tuned and the sequence determines the enthalpy and defines how strong the two ssDNA are bound. The flexibility, after hybridization to a double stranded DNA (dsDNA), is reduced and depends on the persistence length of the dsDNA [38, 39]. If the dsDNA is smaller than the persistence length, the dsDNA behaves like a rigid rod. Furthermore, companies produce synthetic DNA with high precision and many modifications, for example with cholesterol moieties and fluorophores. Due to the high experimental control of its molecular properties, DNA is a powerful tool to study multivalent interactions on the molecular level.

To date, colloid-colloid and colloid-surface interactions have been extensively studied with surface anchored [40–42] and with surface mobile DNA [43–45]. Depending on the length scale and physical properties of the experimental system, different biologi-

cal processes can be studied and a choice of surface anchored or surface mobile DNA strands can be made.

Surface mobile DNA allows for the investigation of multivalent interactions just like they occur in cell-cell adhesion. The integration of DNA molecules on giant unilamellar vesicles, additionally, showed that deformation of the GUV expands the surface contact area and increases the number of interactions [46, 47]. To avoid the deformation of the membrane, studies use membrane coated silica particles with anchored DNA that provides full mobility of the binding sites [48, 49].

The experimental model systems introduced so far mimic multivalency on the microscale and between membranes. Mixing two different populations of multivalent objects with one being on the micrometer scale with mobile receptors and the other consisting of nanometer objects with surface anchored DNA linkers resembles virus-cell interactions. With experimental techniques like dynamic light scattering, it is possible to measure the binding kinetics of the nanoparticles to the larger vesicles in solution [50]. Furthermore, this system allows for the investigation of surface targeting and confirmed that the interactions strength and DNA density are crucial parameters to tune the selectivity [51]. In addition to their high selectivity, virus particles also diffuse along the cell membrane after binding [52], which we will discuss in the following.

Next to surface targeting, studying the diffusion of surface bound particles is important as it is also a common property during particle-cell adhesion. DNA coated nanoparticles [53] and small unilamellar vesicles [54] showed that the number of interactions dictates the diffusive behavior of the adsorbed particle. How many interactions are made between the particle and surface depends on the DNA density and length [55].

These experimental model systems have added to the fundamental understanding of multivalency. DNA functionalised particles are an effective tool to study multivalent binding, as they have high control of physical properties of the system and are easy to visualize. To explore multivalent effects on a smaller lengthscale, we present an experimental model system that can overcome the limitations of the above mentioned systems and allows quantitative insights on the ligand-receptor level.

DNA nanostars DNA hybridization can be used to design nanostructures with very high precision, also known as DNA origami. Here, we employ a very simple structure that consists only of a few ssDNA strands and results in a star shaped geometry, also known as DNA nanostar [37, 56], see Fig. 1.5d. At the end of each arm is a ssDNA (sticky end) that can hybridise with the complementary sequence similar to the DNA coated colloids.

Their design with multiple binding arms makes DNA nanostars a multivalent system. Several studies, for instance have demonstrated phase transitions [37, 57] and the formation of DNA hydrogels [57, 58]. Alltogether, these studies show the high experimental control of DNA nanostars mimicking multivalency with valencies below 10. Furthermore, next to the number of arms and interaction strength, the flexibility of the arms can be controlled, which influences the self-assembly of DNA nanostars [59].

Present experimental model systems consisting of polymers, colloidal particles and viruses contributed significantly to our understanding of multivalency. However, these model systems lack the possibility of engineering a multivalent object with few ligands

on its surface. In addition, dynamic information of ligand and receptor interactions is still missing. Also, how does the bond form between ligands and receptors anchored to two fluid surfaces? A dynamic picture of the bond formation can give insights into the diffusion of micrometer-sized colloids as a function of the formed bonds. But, there is a lack of engineering multivalent particles with fully flexible ligands to study superselective surface adsorption with few ligands on the order of $1-10$ as it was presented by Frenkel and coworkers [6].

Throughout this thesis we use different experimental model systems and techniques to address these questions. We present a study of multivalent interactions and superselective surface targeting. By using linkers based on DNA-DNA interactions, we can precisely tune the density and interaction strength, which are crucial parameters for selectivity, as predicted by theory. Using fluorescent microscopy, we can directly visualise the bond formation and study the dynamic binding and unbinding of ligands and receptors.

1.4. OUTLINE OF THIS THESIS

Chapter 2 page 15: "Direct visualization of superselective colloid surface binding mediated by multivalent interactions"

In chapter 2 we present an experimental model system to study superselective colloid-surface binding between two fluidic surfaces. Using membrane coated surfaces, functionalised with DNA linkers, we ensure full mobility of the ligands and receptors. Because each ligand and receptor is equipped with a fluorophore, we can directly visualize the interactions and final bond in the colloid-surface contact area. We investigate the change in superselectivity while tuning the enthalpy by changing the sequence of the sticky ends and by varying the density of both ligands and receptors. Lastly, we visualize the dynamic binding and unbinding in the multivalent bond. We find that the weaker the interactions and therefore more dynamically unbind and bind, the more selective the system.

Chapter 3 page 41: "Bond formation and diffusion of multivalent colloidal particles"

In chapter 3 we study the dynamic multivalent bond formation with the same experimental model system as described in chapter 2. Simultaneous tracking of the spatial coordinates of the bond and intensity gives insights in the diffusive motion as a function of bonds. Furthermore, we visualize and measure patch sizes in the dynamic equilibrium resulting from different sticky ends at varying DNA densities on the colloid. Finally, we track colloids with a fully established bond and compare the diffusion coefficient with the size of the bonds. We find that the colloid diffusion decreases with a growing number of interactions in the patch. Moreover, we observe that a high ligand density hinders the formation of interactions and leads to a decrease in patch size.

Chapter 4 page 57: "Superselective DNA nanostar adsorption"

In chapter 4 we introduce a new experimental model system to study superselective surface binding of entities with up to 10 bonds using DNA nanostars. With fluorescent microscopy we can directly visualize the adsorption of nanostars to a surface and study

the change in adsorption for different sticky ends and number of arms. Moreover, we measure the dynamic binding and unbinding of the DNA nanostars using fluorescent recovery after photobleaching, which provides insights into the number of bonds formed. We find that during the multivalent bond formation, a weak first bond and a high probability for subsequent bonds is needed to achieve a high superselectivity.

Chapter 5 page 81: "Preliminary work and conclusion"

In chapter 5 we present preliminary experiments on the diffusive properties of membrane anchored receptors. A combination of fluorescent recovery after photobleaching and fluorescent microscopy allows for the evaluation of the diffusion coefficient of the surface mobile receptors. We investigated how additional inert strands influence the diffusion of receptors and how nanostar binding changes the receptors diffusion. We find that additional biomolecules in the supported lipid bilayer and the multivalent binding between receptors and nanostars drastically slow down the receptor diffusion.

REFERENCES

[1] E. Fischer, *Einfluss der configuration auf die wirkung der enzyme,* Berichte der deutschen chemischen Gesellschaft **27**, 2985 (1894).

[2] G. A. Jeffrey and W. Saenger, *Hydrogen Bonding in Biological Structures* (Springer-Verlag, Berlin, 1994).

[3] M. C. Wahl and M. Sundaralingam, *Ch…o hydrogen bonding in biology,* Trends in Biochemical Sciences **22**, 97 (1997).

[4] S. Miyamoto and P. A. Kollman, *What determines the strength of noncovalent association of ligands to proteins in aqueous solution?* PNAS **90**, 8402 (1993).

[5] V. T. Moy, E. L. Florin, and H. E. Gaub, *Intermolecular forces and energies between ligands and receptors,* Science **266**, 257 (1994).

[6] F. J. Martinez-Veracoechea and D. Frenkel, *Designing super selectivity in multivalent nano-particle binding,* PNAS **108**, 10963 (2011).

[7] V. Vasioukhin, C. Bauer, M. Yin, and E. Fuchs, *Directed actin polymerization is the driving force for epithelial cell–cell adhesion,* Cell **100**, 209 (2000).

[8] D. Brahim Belhaouari, A. Fontanini, J. P. Baudoin, G. Haddad, M. Le Bideau, J. Y. Bou Khalil, D. Raoult, and B. La Scola, *The Strengths of Scanning Electron Microscopy in Deciphering SARS-CoV-2 Infectious Cycle,* Frontiers in Microbiology **11**, 2014 (2020).

[9] P. Li, S. Banjade, H. C. Cheng, S. Kim, B. Chen, L. Guo, M. Llaguno, J. V. Hollingsworth, D. S. King, S. F. Banani, P. S. Russo, Q. X. Jiang, B. T. Nixon, and M. K. Rosen, *Phase transitions in the assembly of multivalent signalling proteins.* Nature **483**, 336 (2012).

[10] J. Huskens, *Multivalent interactions at interfaces,* Current opinion in chemical biology **10**, 537 (2006).

[11] J. Meca, A. Massoni-Laporte, D. Martinez, E. Sartorel, A. Loquet, B. Habenstein, and D. McCusker, *Avidity-driven polarity establishment via multivalent lipid–gtpase module interactions,* The EMBO Journal **38**, e99652 (2019).

[12] Ángel M. Cuesta, N. Sainz-Pastor, J. Bonet, B. Oliva, and L. Álvarez Vallina, *Multivalent antibodies: when design surpasses evolution,* Trends in biotechnology **28**, 355 (2010).

[13] B. M. G. Janssen, E. H. M. Lempens, L. L. C. Olijve, I. K. Voets, J. L. J. van Dongen, T. F. A. de Greef, and M. Merkx, *Reversible blocking of antibodies using bivalent peptide–dna conjugates allows protease-activatable targeting,* Chemical Science **4**, 1442 (2013).

[14] L. Shapiro, A. M. Fannon, P. D. Kwong, A. Thompson, M. S. Lehmann, G. Gerhard, J. Als-Nielsen, J. Als-Nielsen, D. R. Colman, and W. A. Hendrickson, *Structural basis of cell-cell adhesion by cadherins,* Nature **374**, 327 (1995).

[15] V. M. Braga, *Cell–cell adhesion and signalling,* Current Opinion in Cell Biology **14**, 546 (2002).

[16] X. Du, Y. Li, Y.-L. Xia, S.-M. Ai, J. Liang, P. Sang, X.-L. Ji, and S.-Q. Liu, *Insights into protein–ligand interactions: Mechanisms, models, and methods,* International Journal of Molecular Sciences **17**, 144.

[17] W. J. Errington, B. Bruncsics, and C. A. Sarkar, *Mechanisms of noncanonical binding dynamics in multivalent protein–protein interactions,* PNAS **116**, 25659 (2019).

[18] S. Banjade and M. K. Rosen, *Phase transitions of multivalent proteins can promote clustering of membrane receptors,* eLife **3**, e04123 (2014).

[19] F. Liu and K. J. Walters, *Multitasking with ubiquitin through multivalent interactions.* Trends in biochemical sciences **35**, 352 (2010).

[20] M. Müller, D. Lauster, H. H. Wildenauer, A. Herrmann, and S. Block, *Mobility-based quantification of multivalent virus-receptor interactions: New insights into influenza a virus binding mode,* Nano Letters **19**, 1875 (2019).

[21] N. J. Overeem, E. van der Vries, J. Huskens, N. J. Overeem, J. Huskens, and E. van der Vries, *A dynamic, supramolecular view on the multivalent interaction between influenza virus and host cell,* Small **17**, 2007214 (2021).

[22] A. S. Perelson, *Receptor clustering on a cell surface. iii. theory of receptor cross-linking by multivalent ligands: Description by ligand states,* Mathematical Biosciences **53**, 1 (1981).

[23] B. Becker, M. R. Shaebani, D. Rammo, T. Bubel, L. Santen, and M. J. Schmitt, *Cargo binding promotes kdel receptor clustering at the mammalian cell surface,* Scientific Reports **6**, 1 (2016).

[24] F. S. Cohen, *How viruses invade cells,* Biophysical Journal **110**, 1028 (2016).

[25] C. Sieben, E. Sezgin, C. Eggeling, and S. Manley, *Influenza a viruses use multivalent sialic acid clusters for cell binding and receptor activation,* PLOS Pathogens **16**, e1008656 (2020).

[26] R. Perozzo, G. Folkers, and L. Scapozza, *Thermodynamics of protein–ligand interactions: History, presence, and future aspects,* Journal of Receptors and Signal Transduction **24**, 1 (2004).

[27] F. J. Martinez-Veracoechea and M. E. Leunissen, *The entropic impact of tethering, multivalency and dynamic recruitment in systems with specific binding groups,* Soft Matter **9**, 3213 (2013).

[28] A. N. Weber, M. C. Moncrieffe, M. Gangloff, J. L. Imler, and N. J. Gay, *Ligand-receptor and receptor-receptor interactions act in concert to activate signaling in the drosophila toll pathway,* Journal of Biological Chemistry **280**, 22793 (2005).

[29] Z. Zhang, Y. Wu, K. Xi, J. Sang, and Z. Tan, *Divalent ion-mediated dna-dna interactions: A comparative study of triplex and duplex,* Biophysical Journal **113**, 517 (2017).

[30] P. Varilly, S. Angioletti-Uberti, B. M. Mognetti, and D. Frenkel, *A general theory of dna-mediated and other valence-limited colloidal interactions,* The Journal of Chemical Physics **137**, 094108 (2012).

[31] B. M. Mognetti, P. Cicuta, and L. D. Michele, *Programmable interactions with biomimetic dna linkers at fluid membranes and interfaces,* Reports on progress in physics **82** (2019).

[32] V. M. Krishnamurthy, L. A. Estroff, and G. M. Whitesides, *Multivalency in ligand design,* Fragment-based Approaches in Drug Discovery **34**, 11 (2006).

[33] G. V. Dubacheva, T. Curk, B. M. Mognetti, R. Auzély-Velty, D. Frenkel, and R. P. Richter, *Superselective targeting using multivalent polymers,* Journal of the American Chemical Society **136**, 1722 (2014).

[34] G. V. Dubacheva, T. Curk, R. Auzély-Velty, D. Frenkel, and R. P. Richter, *Designing multivalent probes for tunable superselective targeting,* PNAS **112** (2015).

[35] N. J. Overeem, P. H. E. Hamming, M. Tieke, E. van der Vries, and J. Huskens, *Multivalent affinity profiling: Direct visualization of the superselective binding of influenza viruses,* ACS Nano **15**, 8525 (2021).

[36] S. A. V. D. Meulen and M. E. Leunissen, *Solid colloids with surface-mobile dna linkers,* Journal of the American Chemical Society **135**, 15129 (2013).

[37] S. Biffi, R. Cerbino, F. Bomboi, E. M. Paraboschi, R. Asselta, F. Sciortino, and T. Bellini, *Phase behavior and critical activated dynamics of limited-valence dna nanostars,* PNAS **110**, 15633 (2013).

[38] P. J. Hagerman, *Flexibility of dna,* Ann. Rev. Biophys. Biophys. Chern **17**, 265 (1988).

[39] J. A. Schellman, *Flexibility of dna,* Biopolymers **13**, 217 (1974).

[40] Y. Wang, Y. Wang, X. Zheng, Étienne Ducrot, J. S. Yodh, M. Weck, and D. J. Pine, *Crystallization of dna-coated colloids,* Nature Communications **6**, 1 (2015).

[41] M. E. Leunissen, R. Dreyfus, F. C. Cheong, D. G. Grier, R. Sha, N. C. Seeman, and P. M. Chaikin, *Switchable self-protected attractions in dna-functionalized colloids,* Nature Materials (2009).

[42] L. D. Michele and E. Eiser, *Developments in understanding and controlling self assembly of dna-functionalized colloids,* Physical Chemistry Chemical Physics (2013).

[43] R. W. Verweij, P. G. Moerman, L. P. Huijnen, N. E. Ligthart, I. Chakraborty, J. Groenewold, W. K. Kegel, A. van Blaaderen, and D. J. Kraft, *Conformations and diffusion of flexibly linked colloidal chains,* JPhys Materials **4** (2021).

[44] I. Chakraborty, D. J. G. Pearce, R. W. Verweij, S. C. Matysik, L. Giomi, and D. J. Kraft, *Self-assembly dynamics of reconfigurable colloidal molecules,* (2021), arXiv:2110.04843 [cond-mat.soft] .

[45] I. Chakraborty, V. Meester, C. V. D. Wel, and D. J. Kraft, *Colloidal joints with designed motion range and tunable joint flexibility,* Nanoscale **9**, 7814 (2017).

[46] S. J. Bachmann, J. Kotar, L. Parolini, A. Šarić, P. Cicuta, L. D. Michele, and B. M. Mognetti, *Melting transition in lipid vesicles functionalised by mobile dna linkers,* (2016).

[47] S. F. Shimobayashi, B. M. Mognetti, L. Parolini, D. Orsi, P. Cicuta, and L. D. Michele, *Direct measurement of dna-mediated adhesion between lipid bilayers,* Physical Chemistry Chemical Physics **17**, 15615 (2015).

[48] M. Rinaldin, R. W. Verweij, I. Chakraborty, and D. J. Kraft, *Colloid supported lipid bilayers for self-assembly,* Soft Matter **15**, 1345 (2019).

[49] R. W. Verweij, P. G. Moerman, N. E. Ligthart, L. P. Huijnen, J. Groenewold, W. K. Kegel, A. V. Blaaderen, and D. J. Kraft, *Flexibility-induced effects in the brownian motion of colloidal trimers,* Physical Review Research **2** (2020).

[50] R. Lanfranco, P. K. Jana, L. Tunesi, P. Cicuta, B. M. Mognetti, L. D. Michele, and G. Bruylants, *Kinetics of nanoparticle-membrane adhesion mediated by multivalent interactions,* Langmuir **35**, 2002 (2019).

[51] M. R. W. Scheepers, L. J. van IJzendoorn, and M. W. J. Prins, *Multivalent weak interactions enhance selectivity of interparticle binding,* PNAS **10**, 202003968 (2020).

[52] T. Sakai, S. I. Nishimura, T. Naito, and M. Saito, *Influenza a virus hemagglutinin and neuraminidase act as novel motile machinery,* Scientific Reports **7**, 1 (2017).

[53] S. Merminod, J. R. Edison, H. Fang, M. F. Hagan, and W. B. Rogers, *Avidity and surface mobility in multivalent ligand–receptor binding,* Nanoscale **13**, 12602 (2021).

[54] S. Block, V. P. Zhdanov, and F. Höök, *Quantification of multivalent interactions by tracking single biological nanoparticle mobility on a lipid membrane,* Nano Letters **16**, 4382 (2016).

[55] A. McMullen, S. Hilgenfeldt, and J. Brujic, *Dna self-organization controls valence in programmable colloid design,* PNAS **118** (2021).

[56] N. C. Seeman, *Nucleic acid junctions and lattices,* Journal of theoretical biology **99**, 237 (1982).

[57] L. Rovigatti, F. Smallenburg, F. Romano, and F. Sciortino, *Gels of dna nanostars never crystallize,* ACS Nano **8**, 3567 (2014).

[58] F. Spinozzi, M. G. Ortore, G. Nava, F. Bomboi, F. Carducci, H. Amenitsch, T. Bellini, F. Sciortino, and P. Mariani, *Gelling without structuring: A saxs study of the interactions among dna nanostars,* Langmuir **36**, 10387 (2020).

[59] R. A. Brady, W. T. Kaufhold, N. J. Brooks, V. Fodera, and L. D. Michele, *Flexibility defines structure in crystals of amphiphilic dna nanostars,* Journal of Physics: Condensed Matter **31**, 074003 (2019).

2

DIRECT VISUALIZATION OF SUPERSELECTIVE COLLOID-SURFACE BINDING MEDIATED BY MULTIVALENT INTERACTIONS

Reliably distinguishing between cells based on minute differences in receptor density is crucial for cell-cell or virus-cell recognition, the initiation of signal transduction and selective targeting in directed drug delivery. Such sharp differentiation between different surfaces based on their receptor density can only be achieved by multivalent interactions. Several theoretical and experimental works have contributed to our understanding of this "superselectivity", however a versatile, controlled experimental model system that allows quantitative measurements on the ligand-receptor level is still missing. Here, we present a multivalent model system based on colloidal particles equipped with surface-mobile DNA linkers that can superselectively target a surface functionalized with the complementary mobile DNA-linkers. Using a combined approach of light microscopy and Foerster Resonance Energy Transfer (FRET), we can directly observe the binding and recruitment of the ligand-receptor pairs in the contact area. We find a non-linear transition in colloid-surface binding probability with increasing ligand or receptor concentration. In addition, we observe an increased sensitivity with weaker ligand-receptor interactions and we confirm that the time-scale of binding reversibility of individual linkers has a strong influence on superselectivity. These unprecedented insights on the ligand-receptor level provide new, dynamic information into the multivalent interaction between two fluidic membranes mediated by both mobile receptors and ligands and will enable future work on the role of spatial-temporal ligand-receptor dynamics on colloid-surface binding.

2.1. INTRODUCTION

Processes at biological interfaces are often governed by multivalent interactions. They play a key role in signal transduction, through inhibition and activation of signaling complexes, recognition and interactions between viruses and cells, as well as cell-cell adhesion [1–5]. Multivalent bonds consist of a large number of weak bonds instead of a single strong one, which creates an interaction that is not only strong but also highly selective. The selectivity in multivalent systems goes beyond the correct recognition of a single ligand-receptor pair and allows "superselective" binding only to surfaces that exceed a critical receptor concentration. This allows for a sharp differentiation of surfaces that consist of the same receptor type but vary in receptor density. Integrating this powerful feature into drug delivery systems would enable highly selective targeting of diseased cells [6–8], for example, in cancer therapy [9–11] where tumor cells over-express receptors on their surface [12, 13], or to target viral infections [14].

For multivalent recognition and particle uptake in biological settings, as well as for applications such as directed drug delivery, the binding affinity to the target surfaces needs to be precisely tuned. To this end, the bond should be selective and strong yet weak enough to be reversible to, for example, facilitate endocytosis [15]. Specifically, theoretical studies have shown that the ligand density as well as interaction strength need to be adjusted with respect to the receptor density to increase the selective surface binding [16–18]. In addition, receptor mobility on the target surface - a key feature of membranes - leads to receptor clustering that can enhance the surface binding at low receptor concentrations [19–21].

These theoretical predictions have inspired the design of various experimental systems that can be used to investigate superselective surface binding. The ideal system for understanding superselectivity in a biological context should mimic the lateral mobility of the ligands and receptors, and provide full control over their interaction strength and surface densities, as well as yield quantitative insights into the bond formation and dynamics. Experimentally, superselective surface binding has been demonstrated for systems that consisted of ligand-bearing polymers [19, 22, 23], DNA-coated particles [20, 24], Influenza virus particles [25], as well as small and giant unilamellar vesicles [21]. These experiments confirmed theoretical predictions that a low binding affinity and high valency are crucial for obtaining superselectivity, and furthermore showed that lateral mobility of receptors on the target surface can induce clustering of the ligands or receptors in the bond area, which enhances superselectivity [19].

However, despite these intriguing observations, to date no system exists that captures the key features of biological interfaces, with both mobile ligands and receptors hosted by a lipid membrane, nor one that combines fluidic interfaces and the possibility for direct visualization of binding dynamics with a tunable interaction strength and ligand/receptor densities. This lack of a fully tunable model system prevents us from developing a comprehensive framework for multivalent interactions in biologically relevant settings. In particular, we expect that direct visualization of the spatial distribution of surface-mobile ligands and receptors will provide insights into their dynamics and impact on superselective surface binding.

This chapter has been published as: C. Linne, D. Visco, S. Angioletti-Uberti, L. Laan and D. J. Kraft, Direct visualization of superselective colloid-surface binding mediated by multivalent interactions, *PNAS* **36** (2021)

Here, we introduce a colloid-based model system that allows direct investigation of the individual ligand-receptor interactions in a multivalent bond and their collective binding behaviour to a target surface. We achieve this using fluorescently labelled double-stranded DNA with a single stranded overhang that can hybridize with the complementary sequence, anchored in a lipid membrane both on the colloids as well as the target surface. We observe that the colloid-target surface binding is mediated by the accumulation of receptors and ligands in the contact area. Interestingly, on the multivalent interaction timescale, individual ligand-receptor bonds dissolve and reform repeatedly. This dynamic reversibility confirms that the individual interactions are weak, in agreement with our observation of superselective binding at a critical ligand and receptor density. Our results motivate the development of novel theoretical models that link individual ligand-receptor dynamics to colloid-membrane binding and to reconcile effects taking place on the molecular scale with those on the micrometer scale.

2.2. RESULTS

2.2.1. MULTIVALENT BOND DESIGN AND VISUALIZATION

Our multivalent experimental model system consists of colloidal probe particles functionalized with ligands and a surface featuring complementary receptors, see Fig. 2.1a. Both the colloidal probe particles (2.12 ± 0.06 μm silica spheres) and the glass surface are coated with a supported lipid bilayer (SLB) and functionalized with DNA linkers as the ligand-receptor system. Each DNA linker consists of a 77bp double stranded stem, which is modified with cholesterol on one 5′ end to facilitate the anchoring in the lipid membrane. Attached to the double stranded stem, the linkers feature a single-stranded overhang (sticky end) whose length and complementary base-pair sequence provide precise control over the tuneability of the hybridisation free energy. See Materials and Methods and Supplementary Information for details. The integration into a lipid membrane both on the colloidal probe and the surface provides full mobility of ligands and receptors if the lipid membrane is in the fluid state [26].

To visualize and quantify the multivalent colloid-surface binding, we employ a combination of total internal reflection fluorescence microscopy (TIRFM) with Foerster Resonance Energy Transfer (FRET) [27]. We place fluorophores, which are also FRET pairs, on the 3′ end of the complementary DNA linkers, see Fig. 2.1a, and use dual color imaging with alternating laser excitation to investigate the DNA-DNA interactions in the colloid-surface contact area. The separate imaging of the channels provides information on the ligand and receptor distribution on the surface, see Fig. 2.1b. Upon binding, the intensity of the ligand and receptor signal increases both on the colloid and surface, and, importantly, a FRET signal appears. See Fig. 2.1b. We verify that the FRET signal corresponds to the presence of a colloidal probe by overlaying it with a bright field image, see Fig. 2.1b. The detection of the fluorescent and FRET signal is crucial to distinguish bound from unbound particles. The extended fluorescent patch in the contact area implies a local increase in the concentration of ligands and receptors, and originates from the recruitment of the surface-mobile DNA linkers to the contact area. The simultaneous appearance of the FRET signal indicates that there are multiple ligand-receptor interactions between the colloidal probe and the surface and shows that our system is

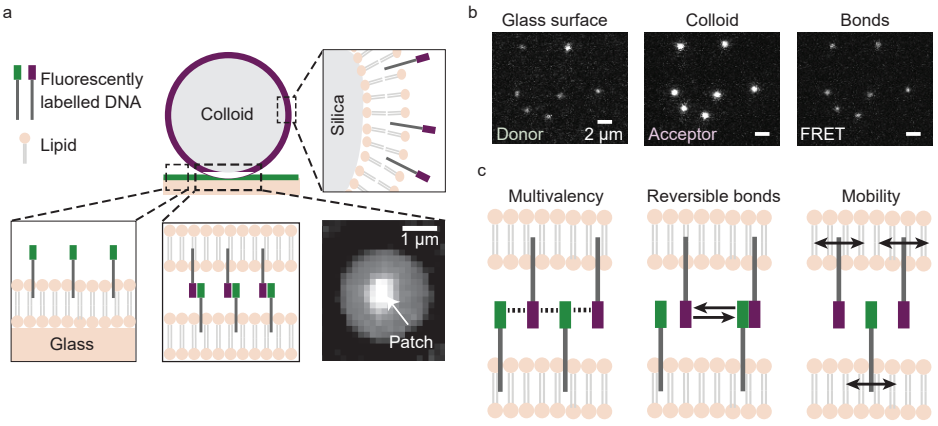

Figure 2.1: **Experimental model system.** (a) The two-dimensional experimental system consists of 2.12μm silica colloids functionalized with double-stranded DNA stems with a single-stranded linker overhang as the ligand and receptor system. The DNA strands are anchored in a lipid membrane on both the colloid and flat glass surface which ensures their full mobility on the surface. (b) We separately detect the fluorescent signal of the receptor (left) and ligand (middle) DNA strands, as well as the FRET signal emitted by bound ligand-receptor pairs (right). The presence of a bright patch in the FRET channel indicates that a multivalent bond has been formed between the colloid and the surface. (c) Our model system features surface mobility of both ligands and receptors and allows us to tune the number of ligands and receptors (valency) as well as the interaction strength to systematically study superselective colloid-surface binding on the ligand-receptor level.

multivalent. With this experimental setup, which combines tunable ligand and receptor densities, mobile binding sites and adjustable interaction strength (see Fig. 2.1c), we can control and investigate the thermodynamic parameters relevant for superselective binding of multivalent colloids to a target surface and gain insights on the ligand-receptor dynamics on the molecular level.

2.2.2. NON-LINEAR BINDING PROBABILITY AS A FUNCTION OF LIGAND DENSITY

The hallmark of superselective binding is a sharp, nonlinear change of the binding probability in a specific ligand or receptor density range. We start by investigating the colloid-surface binding probability with increasing ligand density, σ_L, while keeping the receptor density, σ_R, on the surface fixed. Furthermore, we keep the overall DNA density constant on the colloidal probe and the target surface by the addition of 77bp double stranded DNA that does not possess a sticky end. This ensures a constant concentration of cholesterol in the lipid membrane and hence constant membrane properties [10, 28, 29]. At low σ_L the fluorescent signal is homogeneously distributed over the colloid and the target surface and we do not observe fluorescent patches or a FRET signal (see Fig. 2.2a). This indicates that binding does not occur despite the availability of DNA linkers on both colloid and surface. An increase of the ligand density on the colloid leads to the formation of patches on some probe particles, which implies that a fraction of the colloids in the sample are bound to the surface. Upon a further increase in σ_L we observe

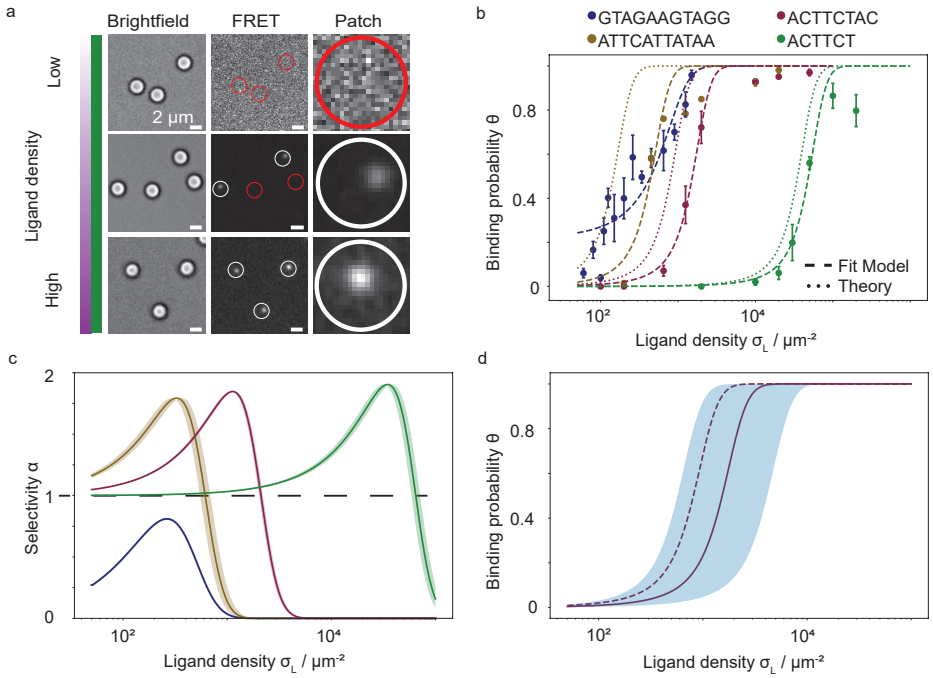

Figure 2.2: **Superselective surface binding.** (a) Combining the information of the colloid position obtained from brightfield imaging with the FRET signal from bonded ligand-receptor allows us to discriminate whether a colloid-surface bond, a patch, has been formed. With increasing ligand density on the colloids larger and more bond patches are formed, implying an increase in the binding probability Θ. The dynamic range between FRET images was individually adjusted to achieve an optimal visualization of the patch. (b) Measured colloid-surface binding probability Θ as a function of ligand density σ_L for different ligand-receptor interaction strengths tuned by varying the length of the single-stranded end. Dashed lines are least-square fits to the model from Frenkel and co-workers [16]; dotted lines represent the adsorption profile obtained using a theoretically computed ΔG_{tot}. The data with the longest sticky end GTAGAAGTAGC is fitted with a logistics function. Increasing binding strength shifts the curves to the lower ligand densities. The good agreement between fitting and theoretical evaluation is even more remarkable considering that errors in binding energies are greatly amplified. The errorbars represent the standard error of at least three individual experiments. (c) The change in binding probability with ligand density can be measured by the selectivity parameter $\alpha = \frac{d\ln(\Theta)}{d\ln(\sigma_L)}$ and was derived from the fits in 2.2 b). The shaded region shows the upper and lower boundary of α, resulting from the least square fit error for the binding free energy $\Delta G^{\text{fit}}_{\text{bond}}$. (d) Sensitivity of fitting model The solid and dashed line are the same as in b); the shaded region shows the error bar for an uncertainty of $\pm 1 k_B T$.

that all colloids that are in close proximity to the membrane display a patch. The intensity of the patch differs between colloids, which is possibly due to the variability of ligand density between the functionalized colloids [30, 31]. Additionally, the size of the patch at the highest ligand density shown in Fig. 2.2a spans an area of approximately $\approx 0.37 \mu m^2$. If we expect the patch to be circular, we can estimate the patch area $A_p = 2\pi R_c L$, where R_c is the colloid radius and L the total bond length, yielding $A_p \approx 0.37 \mu m^2$, which agrees

very well with the measured patch area. The binding probability increases with the ligand concentration, however, superselectivity requires this transition to be non-linear.

Therefore, we determine the number of bound particles, N_B, relative to the total number of colloids, N_C, to measure the binding probability, $\Theta = \frac{N_B}{N_C}$. A value of Θ equal to 0 implies that no colloids are bound, whereas the upper limit of $\Theta = 1$ is set by all colloids being bound to the surface. Besides varying the ligand density on the colloidal probe, we tested the binding behaviour for four different interaction strengths, i.e. for four different sticky ends. We find that the binding probability smoothly transitions from an unbound to a bound state and saturates at high ligand densities, shown in Fig. 2.2b. Unexpectedly, saturation occurs slightly below $\Theta = 1$, even for very high ligand densities. A possible explanation for this observation is that at a certain ligand density, the binding free energy increases slower compared to the steric repulsion of the receptors, leading to a maximum Θ smaller than one, [7], and even an eventual drop instead of saturation.

The range of ligand densities where the transition occurs depends on the interaction strength: the higher the interactions strength, or, the longer the sticky end, the fewer ligands are required for binding the colloid to the surface. In addition, the slope of this transition becomes steeper for weaker ligand-receptor interactions, indicating a higher sensitivity of the binding probability to the ligand density.

We examined the selectivity of the colloid binding for each binding probability curve by evaluating the relative change in binding probability with respect to a change in the ligand density σ_L , also known as the selectivity parameter $\alpha = \frac{\mathrm{d}\ln(\Theta)}{\mathrm{d}\ln(\sigma_L)}$ [16]. The system is superselective in a specific ligand density range if $\alpha \gg 1$. In order to evaluate α for the different sticky ends, we first need a mathematical description of $\Theta(\sigma_L)$. A physically-justified analytical form based on statistical mechanics considerations can be built by adapting a model first described by Martinez-Veracoechea and Frenkel [16]. In this model, the binding probability Θ is written as:

$$\Theta = \frac{zq(N_L, N_R, G_{\mathrm{bond}})}{1 + zq(N_L, N_R, G_{\mathrm{bond}})}, \tag{2.1}$$

where $z = \rho_B \upsilon_{\mathrm{bind}}$ is the multivalent particle activity in a (diluted) solution, ρ_B being its bulk density and υ_{bind} the binding volume, that is, the volume the particle centre of mass can move in while being able to form bonds to the surface. In this expression, a central role is that of $q(N_L, N_R, G_{\mathrm{bond}})$, the ratio between the partition function in the bound and unbound state, which depends on the total number of ligands on the colloid and receptors on the surface, N_L and N_R, respectively, as well as their binding (free)-energy, G_{bond}. In our case, a simple mean-field approximation (see details in the Supplementary Information) leads to the formula:

$$q(N_L, N_R, G_{\mathrm{bond}}) = \left[1 + N_R \exp\left(-\beta G_{\mathrm{bond}}\right)\right]^{N_L} - 1, \tag{2.2}$$

with $\beta = k_B T$ where k_B is the Boltzmann constant and T is the temperature. Introducing a threshold detection value for the number of ligand-receptor bonds to the theory does not change the results in any statistically significant way, i.e. its effect is below the noise introduced by experiments. Therefore, we here used the simpler version of the model (see Supplementary Information). In this model, a bound state is any state where at least one bond is present, as we measure in our experiments. The binding strength of

the multivalent system is incorporated in q, which takes into account all possible binding configurations of the ligands and receptors, as well as information regarding the average strength of a single ligand-receptor bond, measured by $\exp\left(-\beta G_{\text{bond}}\right)$. Notably, in our system the bond strength is affected by experimental parameters such as the size of the rigid, double-stranded stem of the DNA, the sequence of the single-stranded part (sticky end) as well as DNA mobility on the colloid [32]. In particular, the latter introduces a dependence of the effective bond strength on the colloids area, as well as on that of the surface on which receptors are grafted [33]. The exact value of G_{bond} can be calculated via detailed molecular simulations or experiments. Here, we leave it as a fitting parameter, and then compare the fitted value with an approximate theoretical expression derived by Mognetti et al [34] for mobile ligands and receptors and adapted here for our system. Within this framework, we obtain:

$$G_{\text{bond}} = G_0 + G_{\text{conf}} = G_0 + k_B T \log\left(2 R_c A_{\text{tot}} \rho^{\circ}\right), \tag{2.3}$$

where G_0 is the binding energy of the sticky end of the DNA in solution (which can be accurately estimated via Santalucia's nearest-neighbour rules [35]) and G_{conf} is the so-called configurational contribution to the bond energy [32]. In our system, this last term turns out to be only dependent on the colloid radius, R_c, the total binding surface A_{tot}, and the reference molar concentration $\rho^{\circ} = 1M$, see details in the Supplementary Information. Importantly, using Eq. 2.3 the binding probability Θ is fully determined, leaving no fitting parameter.

The results of fitting the experimental data on the binding probability as a function of the ligand density is reported in Fig. 2.2, along with the experimental data, using both the expression where G_{bond} is left as a fitting parameter, which we will refer to as the free model, as well as the full theory. The fabrication process of ligand-coated colloids leads to a variability in the number of ligands per particle. Although including the effect of variability in the analytical model could be done in principle (see e.g. [16]), to avoid introducing artefacts the measured distribution should be used instead of assuming a specific analytical form, which is not known for our samples. At the same time, the inclusion of a probability distribution describing the variability would not change the trends that we observe. Because of these reasons, we neglect ligands fluctuations in our model. In the steep regime where α is determined, the free model nicely captures the experimental data for all sticky end sequences but the strongest one. For the strongest binding sequence ($\Delta G^0 = -17 k_B T$), however, the predicted trend is steeper than what is observed experimentally and for this reason the theoretical model cannot be relied on to calculate the value of the superselectivity parameter α. Thus we use an empirical logistic function with two parameters for this case, see Fig. 2.2b. The decrease in predictive power of the theoretical expression for increasing bond strengths is expected because the theoretical model is based on equilibrium considerations, where we assumed that binding and unbinding is fast enough for a colloid to fully sample all its possible binding configurations. However, this assumption becomes less and less justified as the bond lifetime increases, an increase expected to be exponential in terms of G_0.

For the range of parameter in which the equilibrium model well describes the experimental data, we can compare the free model with the full theory, see Table 2.1. The agreement is remarkable, as the full theory provides a value for the only fitting parame-

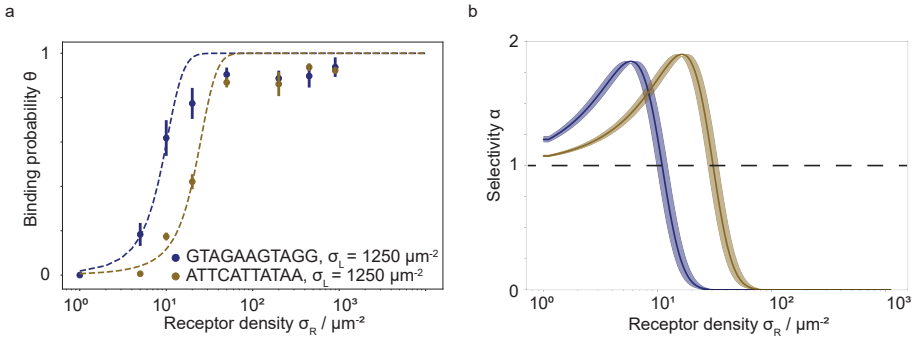

Figure 2.3: **Multivalent binding as a function of the receptor density.** (a) Binding probability as a function of the receptor density for the 11 bp sticky ends GTAGAAGTAGG and ATTCATTATAA at fixed ligand density of $1250\mu m^{-2}$. The errorbars represent the standard error of at least three individual experiments. (b) Selectivity parameter α resulting from a fit with the physical model shows a superselective regime with $\alpha > 1$ for both sticky ends. The shaded region shows the upper and lower boundary of α, resulting from the least square fit error for the binding free energy $\Delta G^{\text{fit}}_{\text{bond}}$.

ter in the free model, the bond energy G_{bond}, which only deviates from the one obtained through least-squares fitting by $\approx 1k_BT$. Notably, even such a small discrepancy can result in a relatively large shift of the predicted adsorption probability because of the extreme sensitivity of the latter to G_{bond}, as illustrated in Fig. 2.2d, where the shaded region corresponds to the predicted curve obtained given an uncertainty of $1k_BT$ on the bond energy.

Having fitted the data with an analytical form, we can easily compute the selectivity α, see Fig. 2.2c. Each sticky end shows a maximum selectivity for a specific ligand density. For the three sticky ends ATTCATTATAA ($\Delta G^0 = -13k_BT$), ACTTTCTAC ($\Delta G^0 = -11k_BT$) and ACTTCT ($\Delta G^0 = -7k_BT$) we observe $\alpha \gg 1$, indicating that the colloid-surface binding is superselective. We note that a distribution in the number of ligands per particle across the sample decreases the slope in the binding probability curve. Hence, finding superselective behavior on our sample of colloids with such a distribution implies evidence that the superselectivity parameter α for a sample with a narrower distribution is in fact even higher. The longest and hence strongest-binding sticky end GTAGAAGTAGG ($\Delta G^0 = -17k_BT$) however, does not exceed $\alpha = 1$ and is thus not superselective. The results of the binding probability for different ligand densities and interaction strength show the relevance of employing weak interaction to achieve superselective binding in multivalent systems, as previously pointed out by Martinez-Veracoechea et al. [16].

2.2.3. NON-LINEAR BINDING PROBABILITY AS A FUNCTION OF RECEPTOR DENSITY

Increasing the number of receptors on the flat surface changes the entropic effects upon binding and can increase the sensitivity of colloid-surface binding, similar to a change in ligand density. Here, we tune the selectivity of colloid-surface binding by changing

the receptor density on the surface, while keeping the ligand density constant and at the same time investigating if the colloids indeed bind superselectively to a surface. We quantify the binding probability for two 11 bp sticky ends ATTCATTATAA ($\Delta G^0 = -13 k_B T$) and GTAGAAGTAGG ($\Delta G^0 = -17 k_B T$) at a fixed ligand density of $1250 \mu m^{-2}$, see Fig. 2.3 a. Similar to a change in ligand density, we observe an increase of the binding probability until it saturates around $\Theta = 1$.

We use the same physical model to evaluate the binding probability as well as the superselectivity parameter by fitting the experimental data, finding again good agreement between theory and experiments, see Fig. 2.3a. We note that in this case the selectivity parameter for both 11 bp sticky ends are larger than 1 in a specific receptor density range, and thus both systems are behaving superselectively. Interestingly, in this case the sticky end GTAGAAGTAGG binds superselectively, whereas this was not observed in the system with fixed receptor density and varying ligand density. We hypothesize that the asymmetry of the experimental system in combination with the surface mobility of the DNA linkers can explain these observations: the maximum number of ligands available for binding is constrained by the finite surface area of the colloid whereas the number of receptors that can be recruited to the binding area is only limited by the geometric constraints in the binding area itself. This should affect the combinatorial entropy contribution and hence the superselective binding behavior in two ways: (1) directly, through fewer available binding partners at a given ligand density compared to the same receptor density; but also (2) indirectly, when the timescale for sampling all possible binding configurations increases for lower ligand-densities because the relative number of ligands available for binding is lower, which would decrease the binding probability in Fig. 2.2b. Hence, we suspect that a high valency on the colloid leads to a faster bond formation and thus equilibration of the system, which can explain this observation. These results indicate that the binding kinetics play an important role in multivalent bond formation.

2.2.4. BINDING KINETICS

For superselectivity to be observed on a given timescale, the dynamics of the individual bonds needs to be fast enough for them to behave reversibly on that timescale. In other words, bonds should constantly form and break. In fact, if bonds were irreversible the binding probability would be 1 regardless of the density of ligands and receptors.

Since our setup allows for the direct visualization of the spatial receptor distribution on the flat surface, we can visualize the exchange of the receptors inside the contact area with unbound receptors in close proximity of the patch using Fluorescent Recovery After Photobleaching (FRAP), see Fig. 2.4a. We performed bleaching experiments of ligand-receptor patches in the contact area for three sticky ends ACTCTAC ($\Delta G^0 = -11 k_B T$), ATTCATTATAA ($\Delta G^0 = -13 k_B T$) and GTAGAAGTAGG ($\Delta G^0 = -17 k_B T$) and recorded the signal recovery up to 300s, see Fig. 2.4b. After bleaching the receptors in the patch, we observe a recovery of the signal for all sticky ends, albeit at different rates. Furthermore, the recovery rate depends on the sticky end: the stronger the hybridization free energy, the longer the recovery of the receptor signal takes. This shows that the hybridization energy of the individual receptors and ligands influences the timescale on which the formation and dissolving of bonds occur.

Mathematical modelling allows us to unravel some details of the kinetics in our sys-

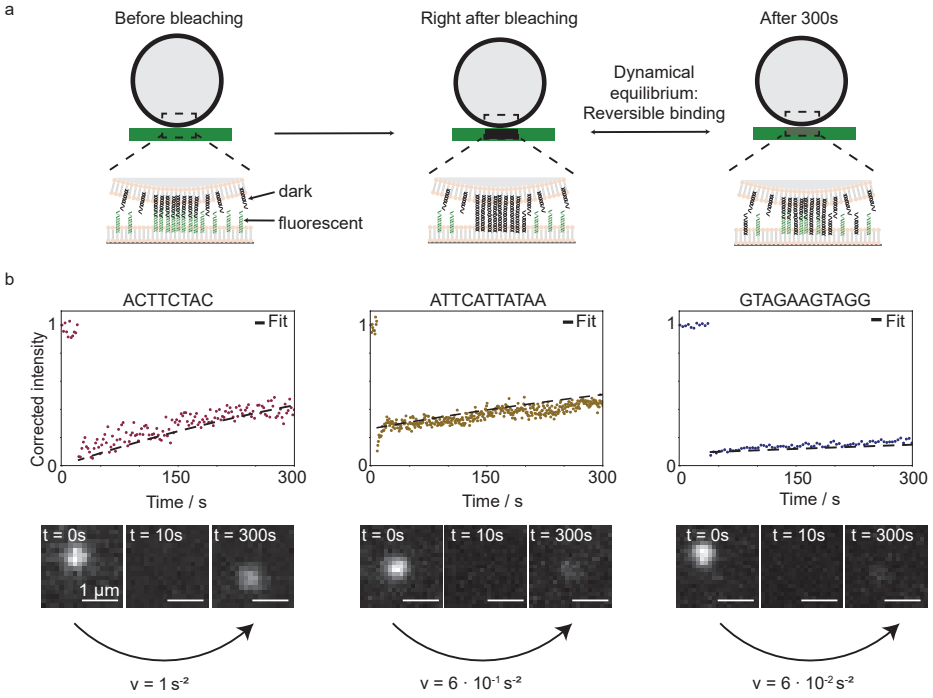

Figure 2.4: **Ligand-receptor binding kinetics in a multivalent bond.** (a) Receptors and ligands with weak interactions repeatedly break and form bonds over time. We visualize their dynamic binding and unbinding by observing the fluorescent recovery after photobleaching (FRAP) of the receptors in the contact area of a colloidal particle and the target surface. For sufficiently weak ligand-receptor interactions the bonded pairs frequently break and bleached receptors can diffuse out of the patch with a flux $\propto k_{out}$. At the same time, unbleached receptors can diffuse into the patch with flux $\propto k_{in}$ and bind to ligands on the colloid. This exchange results in an increase of the receptor signal of the patch in time. (b) FRAP experiments for three sticky ends. Top row shows intensity recovery in time, bottom row shows the recovery of the fluorescent intensity in the receptor channel in time. Colloidal probes coated with the sticky end ACTTCTAC have a ligand density of $100.000\mu m^{-2}$ and colloids coated with the 11bp sticky end comprise of $10.000\mu m^{-2}$ ligands. The target surface was functionalized with a receptor density of $450\mu m^{-2}$. Fitting the FRAP curves with Eq. 2.4, 2.5, 2.6 we can quantify the initial speed of recovery, which is defined as the product $v = \sigma_0 k_{\text{out}} k_{\text{in}}$.

tem and gauge the relative importance of different processes in the observed behaviour. At a coarse-grained level, the intensity recovery over time for our system should be well-described within the framework of Langmuir kinetics [36], whose assumptions we use here to derive a simple two-component model (corresponding to the description of bleached vs unbleached DNA) to gain a better, quantitative understanding of the dynamics of receptor-ligand bonds in the patch. Within this model the normalised intensity I as a function of time after bleaching is given by (see the Supplementary Information for details):

$$I = \frac{k_{\text{in}}\sigma_0}{k_{\text{out}} + k_{\text{in}}\sigma_0}(1 - e^{-k_{\text{out}}t}) + I_0 e^{-k_{\text{out}}t} \tag{2.4}$$

where k_{in} and k_{out} are two kinetic constants related to the inward and outward flux of receptors from the bulk to the patch and vice-versa, respectively, σ_0 is the bulk density of receptors on the surface and I_0 is the initial value of the intensity, which is not always exactly 0 due to partial bleaching of the patch. The initial speed of recovery under our experimental conditions is approximately proportional to the product $k_{in}k_{out}\sigma_0$ which we use to quantify the speed at which systems employing different ligand-receptor pairs reach dynamical equilibrium (again, see the Supplementary Information for details). The exact relation between microscopic details of the system and the value of k_{in} and k_{out} is difficult to quantify without the use of accurate molecular simulations. For example, the speed at which receptors can diffuse will be dependent on the viscosity of the lipid membrane and the interaction between cholesterol linkers and lipid chains. Here, instead, we therefore only provide an approximate expression showing how the kinetic constant is expected to depend on parameters such as the receptors diffusion coefficient in the lipid membrane D, and the sticky end hybridization free energy G_0, which reads:

$$k_{in} = \gamma_1 D \tag{2.5}$$

$$k_{out}^{-1} = k_{diff}^{-1} + k_{break}^{-1} = \gamma_2 R_c L/D + \gamma_3 \exp(-\beta G_0) \tag{2.6}$$

where $\gamma_i, i = 1,2,3$ are system-dependent constants within our model, which we will use to fit our experimental data and L is the length of the receptor. We obtained these approximate formulas by assuming that k_{in} depends on the rate at which ligands from the outside of the binding patch diffuse into it, whereas k_{out} arises from a two-step process, where the bound ligand-receptor pairs in the patch first unbinds, and later the receptor diffuses out of the binding patch, whose size will be of the order of $R_c L$ (see Supplementary Information for details). Given their origin from the solution of a diffusion problem, and based on dimensional analysis, γ_1 and γ_2 should be non-dimensional coefficients of order one and only dependent on geometrical factors, i.e., the specific boundary conditions under which the ligands evolve. Because the sticky ends are located at the top of a long dsDNA stem, they will be mostly far from the lipid membrane and we do not expect them to strongly influence the diffusion coefficient of different ligands and receptors.

For this reason, we fix $\gamma_1 = \gamma_2 = 1$ for all the systems investigated. In contrast, γ_3 has the dimensions of a frequency and can be thought of as the natural frequency at which a bond of $G_0 = 0$ will break. Because γ_3 is expected to be a function of the exact microscopic details of the bond-breaking mechanism, we leave it as a system-specific fitting parameter. Thus k_{in} will be constant by construction for all ligands and receptors, while we expect k_{out} to decrease as the bond between the sticky ends of the DNA becomes stronger, due to its dependence on G_0.

A fit of Eq. 2.4 to the intensity recoveries yields the unknown parameter k_{out}, see Fig. 2.4b. As expected, the product $k_{out}k_{in}$ which quantifies the initial speed of recovery shows a decrease with increasing bond strength. A more detailed analysis of the fitting results provides two crucial physical insights: the first is, that the quality of the fitting is essentially insensitive to the value of k_{in}, whereas it strongly depends on k_{out} (see Supplementary Information, Fig. S1). This suggests that a correct description of the process by which receptors diffuse out of the binding patch is more important then diffusion towards it. To make this more quantitative, we calculate the non-dimensional parameter $\delta = \frac{k_{in}\sigma_0}{k_{out}}$ as a measure of the relative magnitude of the ingoing vs outgoing flux towards

the patch (see Supplementary Information, Tab. S1). For all sequences used here, $\delta \gg 1$, showing that the outward diffusion is much slower than inward diffusion, implying that it is the bottleneck of the signal recovery process.

Secondly, we find that $k_{\text{diff}} \gg k_{\text{break}}$. Interpreted in light of the model expressed in Eqs. 2.5 and 2.6, this suggests that the kinetics in our system is dominated by bond breaking rather than diffusion. In other words, bond breaking is the rate-limiting factor for the system to sample different binding configurations. This is an important finding since superselectivity has been shown to arise from statistical mechanical effects, in particular, the steep increase in the combinatorial entropy of binding as the number of ligands and receptors increases. To observe an ergodic sampling of these configurations within the timescales accessible to experiments, and thus observing superselective behaviour (which is an equilibrium property), requires the system dynamics to happen on much shorter timescales. Here we have shown that, at least for our system, these are dominated by the unbinding kinetics of the ligand-receptor pair. Similar findings have been reported in a recent study focusing on the mode of diffusion of ligand-coated colloid exhibiting inter-particle linkages [37].

2.3. CONCLUSION

Multivalent binding in a fully mobile system is a highly dynamic process that can show superselective surface binding at the right ratio of enthalpic and entropic contributions. In this work, we have combined experiments with theory to investigate the binding probability of multivalent ligand and receptor interactions between two surfaces that provide full mobility to the ligands and receptors. Our experimental setup allowed us to directly visualize the spatial distribution of the individual binding sites. We have shown that multivalent binding between fluid surfaces is characterized by receptor and ligand clustering as suggested by Lanfranco et al. [20] and Dubacheva et al. [19]. Following the design rules proposed by Frenkel et al. [16] we demonstrated that we can achieve superselective binding by tuning the hybridisation energy of the individual ligand and receptors and measured the effective free energy of binding. Finally, we visualized and quantified the reversibility of weak bonds through the highly dynamic exchange of bound receptors with unbound ones from outside the binding patch.

Future studies with this model system can provide exciting insights into the binding kinetics of multivalent interactions at the ligand-receptor level, for example the formation of bonds and development of the spatial distribution in time. The observed timescale of bond formation and importance of the time scale for bond breakage might be crucial for competitive binding of various receptors on cell surfaces. Moreover, our experimental system can provide insights into membrane deformations caused by locally high receptor and ligand accumulations, which is important for the initiation of endocytosis. Surface targeting in biological systems is often governed by more then one type of receptors and ligands, and our model system can straightforwardly be extended to study the effect of competing interactions between more types of ligands and receptors on superselectivity[38–40]. Finally, our experimental system might provide key insights for applications in nanomedicine as it can be used to improve specific target binding while reducing off-target binding, useful for example for drug-delivery.

Table 2.1: **Comparison between the binding free energy obtained from the multivalent model and experimental data**. The binding free energy ΔG_{bond} is obtained for the four sticky ends by computing the theoretical value (ΔG^{theo}, see Methods) and by fitting Equation 2.1 to the binding curves for a variation in the ligands (see Fig. 2.2), ΔG^{fit}(lig), and receptors (2.3), ΔG^{fit}(rec). The absolute differences between the experimental and theoretical values ΔG^{fit} - ΔG^{theo} are shown in the last column: the first value in each row is obtained using the experimental value of the free energy obtained varying the concentration of ligands ΔG^{fit}(lig), while the second is computed using ΔG^{fit}(rec); these differences are small with respect to thermal energy $k_B T$, verifying that our model is appropriate for our experimental setup.

Free energy ($k_B T$)	ΔG^0	ΔG^{fit}(lig)	ΔG^{fit}(rec)	ΔG^{theo}	$\lvert\Delta G^{\text{fit}}$ - $\Delta G^{\text{theo}}\rvert$
ACTTCT	−7	32	N/A	31	1 − N/A
ACTTCTAC	−11	28	N/A	28	0 − N/A
ATTCATTATAA	−13	27	25	26	1 − 1
GTAGAAGTAGG	−17	27	24	21	6 − 3

2.4. MATERIALS AND METHODS

2.4.1. DNA STRANDS

All DNA strands ([Integrated DNA Technologies, Inc.], [Eurogentec], [IBA]) with a sticky end are functionalized with cholesterol at the 5′. The 3′ is modified with a fluorophore ($Cy3/Cy5$, $Cy3/Atto655$). The complementary backbone DNA strand had a length of 77 bp and cholesteryl-TEG at the 3′ end. Single stranded DNA with the sticky end and single stranded backbone were annealed to 95°C and slowly cooled in 0.2°C/minute steps in Tris Acetate-EDTA-NaCl (TAE, 100mM NaCl, pH = 8, [Formedium]) buffer in a Thermocycler. The resulting DNA strands are double-stranded with a double cholesterol anchor and a single stranded overhang. The hybridized DNA strands were stored in TAE-NaCl buffer at 4°C. The single stranded overhang varies in sequence and length with a hybridisation energy ranging between $\Delta G^0 = -7k_B T - (-17k_B T)$ [41]. The sticky ends used as the ligand and receptor system are ACTTCT, ACTTCTAC, ATTCATTATAA, GTAGAAGTAGG and their respective complementary sequences (see Supplementary Information, Tab. S2).

2.4.2. DNA COATED COLLOID SUPPORTED LIPID BILAYERS

We coated commercial silica spheres [Microparticle GmbH] of 2.12μm with a supported lipid bilayer (SLB). To do so, we mixed the silica particles (0.5wt%) with small unilamellar vesicles (SUVs) consisting of the desired lipid composition and incubated the mixture at room temperature for 30 min. To obtain the SUVs, we first added the desired volume of 18 : 1 DOPC lipids ([Avanti Polar Lipids], stored in chloroform) into a glass vial and let it dry overnight in a vacuum desiccator. Next, we resuspended the dried lipids in TAE-NaCl buffer and extruded the solution with an Avanti mini extruder through a membrane with pore size of 30 nm yielding a transparent solution. By mixing the SUVs with the colloids, the SUVs spread on the colloid surface to form a supported lipid bilayer (SLB). Excess SUVs were removed by centrifugation of the mixture at 2000 rcf for 30 s and subsequent replacement of the supernatant with fresh TAE-NaCl buffer. The desired concentration of hybridized DNA was added to the colloid supported lipid bilayers (CSLB) and incubated for 1h at room temperature [26, 42]. Using the stock concentration and surface

area of the colloids in solution, we estimated the final DNA surface density σ_{DNA} on the CSLB, which typically ranged between $60\mu m^{-2} - 100.000\mu m^{-2}$. After the incubation time we washed the mixture trice by centrifugation at 2000 rcf for 30 s and replacement of the supernatant with fresh buffer. The last replacement of the supernatant was done with imaging buffer (0.8% dextrose, 1 mg/mL glucose oxidase, 170mg/mL catalase, and 1 mM Trolox [(±) – 6 – hydroxy – 2,5,7,8 – tetramethylchromane – 2 – carboxylic acid, 238813] [Merck][43]) to reduce the bleaching of the fluorophores during imaging.

2.4.3. DNA FUNCTIONALIZED SUPPORTED LIPID BILAYER ON FLAT GLAS SURFACE

The microscopy slides and coverslips were sonicated for 30min each in 2% Hellmanex, acetone (> 99.9%) and potassium hydroxide solution (KOH. 1M, [Merck]). Between each change of chemical, the glassware was rinsed with milliQ water and blown dry with nitrogen before use. The experiments were performed in a flow channel consisting of parafilm slices between a glass microscope slide [VWR] and a glass coverslip [VWR]. Placing the construct on a heating stage at 125°C melted the parafilm and bound the objective slide and coverslip together yielding four 2mm × 24mm flow channels. Before we injected SUVs into the flow channels, we cleaned the channels with TAE-NaCl buffer. After 30 min we washed out the excess SUVs with TAE-NaCl buffer and added DNA with the complementary DNA sequence at the desired concentration with respect to the DNA CSLB. Here, the resulting DNA surface densities σ_{DNA} used varied between $5\mu m^{-2} - 1500\mu m^{-2}$. After 1 hour of incubation, we flushed the channels three times with TAE-NaCl buffer before injecting the DNA CSLBs to the flow channels.

2.4.4. TOTAL INTERNAL REFLECTION MICROSCOPY

The colloidal silica particles quickly sedimented to the flat SLB due to their density being higher than that of water. To image the colloid-membrane interactions we used Total Internal Reflection Fluorescence Microscopy (TIRF) on an inverted fluorescence microscope (Nikon Ti2-E) upgraded with an azimuthal TIRF/FRAP illumination module (Gataca systems iLAS 2) equipped with a $100x$ oil immersion objective (Nikon Apo TIRF, 1.49NA). To investigate the DNA-DNA interactions in the colloid-surface contact area, we used dual color imaging with alternating laser excitation with wavelength 561 nm and 640 nm (Cairn Research Optosplit II ByPass, EM-CCD Andor iXON Ultra 897). This technique allowed for alternating excitation of the donor and receptor, yielding a Foerster Resonance Energy Transfer (FRET) when the two complementary DNA linker strands hybridized. Subsequently, we acquired a Brightfield image to localize the colloids on the surface (CCD Retiga R1). This setup was also used to perform Fluorescence Recovery after Photobleaching (FRAP) experiments to investigate the mobility of DNA in a membrane and patch. Per sample we imaged 100 colloids in at least three independent experiments. The errorbar on the binding probability represents the standard error of the mean. The error bar on the selectivity α results from the least square fitting error.

2.4.5. IMAGE ANALYSIS

After the acquisition of the data we deinterleaved and cropped the resulting images with respect to the three fluorescent channels corresponding to the donor, acceptor and

FRET. For each measurement, we first acquired an image with fluorescent beads, which is used for the spatial calibration of the channels and the Brightfield image. An ImageJ plugin [44] was used to overlay the fluorescent channels with the Brightfield image to locate the DNA-DNA interactions with respect to the colloids. We defined a colloid bound to the flat surface via DNA-DNA interactions if we could visually differentiate the signal in the colloid-surface contact area of the donor, acceptor and FRET channel from the local background signal.
For the FRAP experiments we extracted the intensity profile of the bleached area via ImageJ and first subtracted the background noise of the microscope and then normalized the raw intensity with respect to the initial unbleached intensity. Per condition we imaged at least 3 patches and in 3 independent experiments.

2.5. SUPPLEMENT

2.5.1. STATISTICAL MECHANICS MODEL OF ADSORPTION MULTIVALENCY

We implement a model for the adsorption probability Θ of colloids to a receptor decorated surface through multivalent interactions by combining various results previously derived in the literature. In particular, we take Θ to have the form $\Theta = \frac{zq(N_L,N_R,G_{\text{bond}})}{1+zq(N_L,N_R,G_{\text{bond}})}$, as shown e.g. in [16, 23], where $z = \rho_B v_{\text{bind}}$, ρ_B being the bulk density of colloids and v_{bind} their binding volume. For what concerns the value of the partition function q, we make a mean-field approximation, that is, we assume that the binding of a ligand to a certain receptor does not strongly affect the possibility for another ligand to bind it, while at the same time maintaining the constraint that a ligand cannot bind more than one receptor at any one time (the so-called valence-limited condition [32]). As previously discussed [32, 45], this mean-field approximation works well for weak ligand-receptor bonds and when the number of receptors is much larger than the number of ligands. In our system, both conditions are satisfied as the effective bond energies are very large and positive while the number of receptors is around 5 orders of magnitude larger than the maximum number of ligands used.
Under these assumptions we can write the ratio between the bound and unbound partition function for a whole colloid as [16]:

$$q = (1 + N_{\text{R}} e^{-\beta G_{\text{bond}}})^{N_{\text{L}}} - 1 \tag{2.7}$$

where the minus one account for the fact that colloid is considered bound if at least 1 bond is present. Most of the background noise in the experiments are caused by the receptors that are present on the whole target surface. The average receptor density before binding is approximately 7 receptors per pixel. This means that we can distinguish a patch from the local background signal if the number of accumulated receptors in the colloid-surface contact area is above 7 receptors per pixel. Including a threshold for the number of bonds in the theoretical model does not change the fitting results significantly, hence we continue with the simpler version of the model (Eq. 2.7). In Eq. 2.7 G_{bond} is the effective bond energy, including a configurational entropic contribution [32]. Care must be taken in the interpretation of N_{R} and N_{L} in this formula. For colloids with surface-grafted ligands and SLBs with grafted receptors, these would be the number of ligands and receptors, respectively, that are at available for binding given a certain

orientation of the colloid [16]. However, because ligands and receptors are mobile in our system, N_R and N_L correspond to the total number of receptors on the adsorption surface and the total number of ligands per colloid. Thus, in our case, $N_L(N_R)$ can be approximated as the average ligand (receptor) grafting density $\sigma_L(R)$ multiplied by the colloid (binding surface) area.
In order to obtain a theoretical estimate of the free-energy of a single ligand-receptor bond G_{bond}, we use the formula [32]:

$$G_{\text{bond}} = G_0 + G_{\text{conf}} \tag{2.8}$$

where G_0 is the nucleotide-sequence-dependent free-energy of binding in solution for the free sticky end of the complementary DNA, which we calculated using Santalucia's nearest neighbour model [35]. As explained in detail in [32], G_{conf} is a configurational entropic penalty due to the restriction of the phase space for the ligand and receptor pair upon binding. This configurational contribution is evaluated for mobile, rod-like ligands, freely pivoting around their tethering point and with point-like sticky-ends, exactly the conditions of our system where ligands and receptors comprise a long and rigid double stranded DNA (dsDNA) part to which a short sticky end of single stranded DNA (ssDNA) is attached. In particular, $G_{\text{conf}} = G_1 + G_2 + G_3$ in our system, where the three different contributions are:

1. $G_1 = -k_B T \log\left(\frac{A_p}{A_{\text{tot}}}\right)$. This is the entropic cost of localising a receptor within a patch of area $A_p = 2\pi R_c L$ (see e.g., [6]) where binding with a ligand can occur. Here, R_c is the radius of the colloid and L the length of the receptor, because such receptor would otherwise be able to span the whole adsorption surface (A_{tot}) when in the unbound state.

2. $G_2 = -k_B T \log\left(\frac{A_p}{A_c}\right)$. Similarly to G_1, this contribution represent the entropic cost of localising a ligand from the whole colloid surface (A_c) to the patch area.

3. $G_3 = k_B T \log(\rho_0 L A_p)$. This latter term is the entropic cost of bonding a rod-like receptor and a rod-like ligand together, assuming a fixed particle-surface distance equal to the ligand/receptor length L (see Ref. [34] for details).

Combining the three contribution and with some elementary algebra we obtain:

$$G_{\text{conf}} = +k_B T \log(2R_c A_{\text{tot}} \rho_0) \tag{2.9}$$

Interestingly the final expression for the configurational free-energy does not depend on the length of the ligands/receptor or the contact area, implying that it will have the same value for all of the systems considered in our work. Finally, we note that the mean-field calculation of the partition function and that of the configurational bond energy G_{conf}, taken together, turn out to be exactly equivalent to a formula for the adsorption free-energy F_{ads} by Mognetti *et al* in Ref. [34]. To connect the seemingly different treatments, one only needs to recognise that:

$$\exp(-\beta F_{\text{ads}}) - 1 = q, \tag{2.10}$$

where the -1 (as discussed in [46]) stems from the fact that we consider as bound only colloids where at least a single bond is present, whereas F_{ads} is calculated using the zero-energy reference as a state with no bonds.
Substituting our experimental parameters in Eq. 2.9, we get a fixed value of $G_{\text{conf}} \approx 38.7 k_B T$ that once summed with the hybridisation free energies G_0 computed with DINAMelt allows us to predict the fitted values of G_{bond} in our system with an average accuracy of less then $\pm 1.5 k_B T$.

2.5.2. KINETICS OF THE PHOTOBLEACHING EXPERIMENTS

We provide here details of the derivation of a simple mathematical model to describe the photobleaching / recovery experiments. We start by assuming a Langmuir-type dynamics to describe the population of receptors N inside the patch, that is, we have:

$$\frac{dN}{dt} = +k_{\text{in}}(N_{\text{max}} - N)\sigma_{\text{out}} - k_{\text{out}}N, \tag{2.11}$$

where N_{max} is the total number of bonds that can be formed inside the patch. In practice, in Langmuir kinetics we assume the fluxes to be linear in the amount of free sites inside the patch and in the amount of DNA outside of the patch (for the incoming flux inside the patch) and linear with respect to the amount of DNA already in the patch (for the outgoing flux). Thus k_{in} and k_{out}, both positive, are the two proportionality constant for the flux and σ_{out} is the concentration of receptors outside the patch. In principle, σ_{out} is a dynamical quantities changing in time. However, because the total amount of DNA outside the patch is much larger than that inside, we can just assume them to be constant and set $\sigma_{\text{out}}(t=0) \approx const = \sigma_0$. When the system reaches equilibrium, we would thus have:

$$\frac{dN}{dt} = 0 \rightarrow f \equiv \frac{N}{N_{\text{max}}} = \frac{k_{\text{in}}\sigma_{\text{out}}}{k_{\text{in}}\sigma_{\text{out}} + k_{\text{out}}} \tag{2.12}$$

We now exploit the fact that right before bleaching the system is in dynamical equilibrium and bleaching is equivalent to assigning two different "tags" to otherwise equal receptors. We thus distinguish between N_2 and N_1, i.e., the receptors inside the patch that are bleached, or not, respectively, and thus $N = N_1 + N_2$. Note that because of dynamical equilibrium, N remains constant during the recovery process. We can thus write an equation for the amount of unbleached receptors inside the patch:

$$\frac{dN_1}{dt} = +(N_{\text{max}} - N)k_{\text{in}}\sigma_{\text{out}} - k_{\text{out}}N_1. \tag{2.13}$$

which gives the general solution

$$f_1 \equiv \frac{N_1}{N_{\text{max}}} = Ae^{-k_{\text{out}}t} + \frac{k_{\text{in}}\sigma_0}{k_{\text{out}} + k_{\text{in}}\sigma_0} \tag{2.14}$$

where A for the moment is an arbitrary constant. Note that if one normalises the intensity of the signal I_{abs} measured during photobleaching recovery with respect to the value I_{eq} it would have at equilibrium, this normalised signal is exactly equal to f_1. Now

to find a final expression for f_1, we need an initial condition to calculate A. In order to fit experiments, we need to account for the fact that, due to experimental variability, not 100% of the DNA in the patch is bleached at $t = 0$. If we call I_0 the normalised signal intensity at $t = 0$, we obtain that $A = I_0 - \frac{k_{\text{in}}\sigma_0}{k_{\text{out}}+k_{\text{in}}\sigma_0}$, and we arrive to the final equation for the normalised signal:

$$I \equiv \frac{I_{\text{abs}}}{I_{\text{eq}}} = f_1 = \frac{k_{\text{in}}\sigma_0}{k_{\text{out}} + k_{\text{in}}\sigma_0}(1 - e^{-k_{\text{out}}t}) + I_0 e^{-k_{\text{out}}t} \tag{2.15}$$

Note that in practice signal recovery by replacing bleached DNA with unbleached one depends on how fast bonds exchange for a system in dynamical equilibrium. Here, we quantify how fast the process occur by looking at the initial speed of recovery, that is, the initial flux of unbleached particles towards the patch, which is given by a Taylor expansion of df_1/dt for small times, which to leading order is:

$$v_{\text{rec}} = \frac{dN_1}{dt}|_{t=0} = k_{\text{out}}\left(\frac{k_{\text{in}}\sigma_0}{k_{\text{in}}\sigma_0 + k_{\text{out}}} - I_0\right) \tag{2.16}$$

It should be noted that, in our system, we always observe $k_{\text{in}}\sigma_0 \gg k_{\text{out}}$. At the same time, as we are about to explain, k_{in} is not expected to vary between different ligands. For these reasons, and given our form for v_{rec} above, a good quantity to compare the relative speed at which different ligand-receptor pairs reach dynamical equilibrium is the product $k_{\text{in}}k_{\text{out}}\sigma_0$, as reported in Table S1.

We now turn to provide a physical model to interpret the values of k_{in} and k_{out} based on microscopic details of the system. Because of their dependence on molecular details of the system, determining the exact value of k_{in} and k_{out} requires in principle expensive molecular simulations, outside the scope of this work. In the theory we present here we simply provide and fit approximate expressions for k_{in} and k_{out} to characterise the dynamics of the system; this allows us to provide an estimate of their scaling as a function of some fundamental microscopic parameters of the system. Let us first deal with k_{out}. In this Langmuir model, this quantity is proportional to the frequency with which a DNA inside the patch escapes from it. Let us call D the diffusion coefficient of DNA on the surface and assume that the escape time $t_{\text{out}} = 1/k_{\text{out}}$ can be written as the sum of two processes:

1. Unbinding of the DNA from a potential partner, which takes an average time τ_{unbind}. If we consider this as a bond-breaking reaction, we expect this time to be exponentially dependent on the hybridisation energy in solution of the DNA sticky end, G_0 in the main text, hence $\tau_{\text{unbind}} = \gamma_3 \exp(-\beta G_0)$, γ_3 having the dimension of a time. In practice, one can expect γ_3 to be dependent on the microscopic details of the intermediate steps along the unbinding pathway, and thus have a certain dependence on the sequence of nucleotides use [47].

2. Diffusion of the unbound DNA outside the patch area, which takes a time $\tau_{\text{diff}} \approx \gamma_2' A_p^*/D = \gamma_2 R_c L/D$, where this time γ_2 is a non-dimensional constant, approximately of order 1, where we collect the effects of all the finer details of the diffusion process. R_c is the colloid radius and L is the length of the receptor.

Table 2.2: Parameters of the kinetic model for multivalent recovery after photobleaching described in Eq. 4,5,6 (see main text) fitted to experimental data. As detailed in the main text, γ_3 was the only optimised fitting parameter; γ_1 and γ_2 values were fixed to 1, while the diffusion coefficients employed for the computation of the reported quantities were obtained experimentally. In addition to the optimal value of γ_3, various quantities describing the relative importance of different events in the overall kinetics of the system are shown: $k_{in}\sigma_0$ and k_{diff} specify the relevance of diffusion in determining the inward and outward flux; k_{break} describes the speed of the bond-breaking step involved in diffusion exiting the patch; k_{out} is the overall kinetic constant for the outgoing flux; the product $\nu = \sigma_0 k_{out} k_{in}$ quantifies the initial speed of recovery; finally $\delta = \frac{k_{in}\sigma_0}{k_{out}}$ is a non-dimensional parameter providing an estimate of the relative magnitude of the ingoing vs outgoing flux. From the values shown it can be immediately seen how the limiting step of our system dynamics is represented by the bond breaking event ($\delta \gg 1$ for all DNA sequences) which becomes progressively slower as the hybridization free energy increases. The irrelevance of the speed of diffusion has been further confirmed by the results of the parameter space analysis we conducted (see Fig. 2.5) which showed how the quality of the fitting is negligibly affected by the value of the parameters γ_1 and γ_2 (included in the expressions for k_{in} and k_{diff}).

DNA sequence	$\gamma_3\,[s]$	$k_{out}\,[s^{-1}]$	$k_{in}\sigma_0\,[s^{-1}]$	$k_{diff}\,[s^{-1}]$	$k_{break}\,[s^{-1}]$	$\nu\,[s^{-2}]$	δ
GTAG AAGT AGG	$1.5\cdot 10^{-4}$	$2.3\cdot10^{-4}$	$0.27\cdot10^{3}$	17	$2.3\cdot10^{-4}$	$6.2\cdot 10^{-2}$	$1.2\cdot 10^{6}$
ATTC ATTA TAA	$2.4\cdot 10^{-3}$	$1.3\cdot10^{-3}$	$0.45\cdot10^{3}$	29	$1.3\cdot10^{-3}$	$6.0\cdot 10^{-1}$	$3.4\cdot 10^{5}$
ACTT CTAC	$9.2\cdot 10^{-3}$	$1.9\cdot10^{-3}$	$0.72\cdot10^{3}$	46	$1.9\cdot10^{-3}$	$1.3\cdot10^{0}$	$3.8\cdot 10^{5}$

From these considerations, we obtain the final formula:

$$k_{out}^{-1} = \gamma_2 R_c L/D + \gamma_3 \exp\left[-\beta G_0\right] \tag{2.17}$$

Let us now turn to calculating k_{in}, which we will do based on dimensional arguments. The dimension of k_{in} must be that of an area times an inverse time. The only physical quantities in our system that can be combined to give such a dimension basically tell us that k_{in} should be scaled as:

$$k_{in} = \gamma_1 D, \tag{2.18}$$

D again being the DNA diffusion coefficient and γ_1 a non-dimensional constant of order 1 that should only depend on the dimensionality of the system and on its geometry. Note that in practice the diffusion coefficient inside and outside the patch area might not be exactly the same. In fact, we would expect the diffusion of receptors within the patch area to be somewhat slower than outside of it, mostly because additional friction would be expected due to the interactions between unbound ligand-receptor pairs.
Note that given the previous expressions one should expect k_{in} to be the same for all of the systems studied here, whereas k_{out} should decrease for decreasing hybridisation energies G_0, i.e. for stronger bonds.

Table 2.3: DNA sequences. Strand 1 is used as the backbone for all strands with a sticky end to form a double-stranded stem. The complementary strand is denoted with '. Inert strand 1 and inert strand 2 are hybridized to obtain passive double-stranded DNA.

Name	DNA sequence
Strand 1	TCGTAAGGCAGGGCTCTCTAGACAGGGCTCTCT GAATGTGACTGTGCGAAGGTGACTGTGCGAAGG GTAGCGATTTT
Strand 2	TTTATCGCTACCCTTCGCACAGTCACCTTCGCA CAGTCACATTCAGAGAGCCCTGTCTAGAGAGCC CTGCCTTACGATTATAATGAAT
Strand 2'	TTTATCGCTACCCTTCGCACAGTCACCTTCGCA CAGTCACATTCAGAGAGCCCTGTCTAGAGAGCC CTGCCTTACGAATTCATTATAA
Strand 3	TTTATCGCTACCCTTCGCACAGTCACCTTCGCA CAGTCACATTCAGAGAGCCCTGTCTAGAGAGCC CTGCCTTACGAGTAGAAGTAGG
Strand 3'	TTTATCGCTACCCTTCGCACAGTCACCTTCGCA CAGTCACATTCAGAGAGCCCTGTCTAGAGAGCC CTGCCTTACGACCTACTTCTAC
Strand 4	TTTATCGCTACCCTTCGCACAGTCACCTTCGCA CAGTCACATTCAGAGAGCCCTGTCTAGAGAGCC CTGCCTTACGAGTAGAAGT
Strand 4'	TTTATCGCTACCCTTCGCACAGTCACCTTCGCA CAGTCACATTCAGAGAGCCCTGTCTAGAGAGCC CTGCCTTACGAACTTCTAC
Strand 5	TTTATCGCTACCCTTCGCACAGTCACCTTCGCA CAGTCACATTCAGAGAGCCCTGTCTAGAGAGCC CTGCCTTACGAGTAGAA
Strand 5'	TTTATCGCTACCCTTCGCACAGTCACCTTCGCA CAGTCACATTCAGAGAGCCCTGTCTAGAGAGCC CTGCCTTACGATTCTAC
Inert strand 1	CGTAAGGCAGGGCTCTCTAGATTGACTGTGCGA AGGGTAGCGATTTT
Inert strand 2	TTTATCGCTACCCTTCGCACAGTCAATCTAGAGA GCCCTGCCTTACGA

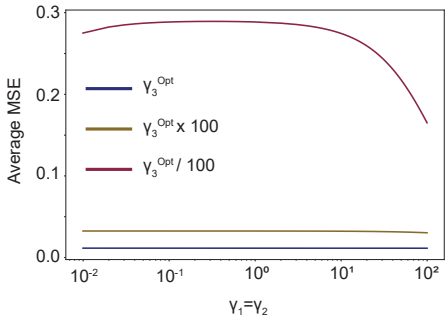

Figure 2.5: Mean square error of the fit as a function of $\gamma_1 (= \gamma_2)$, shown here for both the optimal value of γ_3 (blue line) as well as for two sub-optimal values (yellow and purple line). As it can be seen, the mse of the fit is almost insensitive to the value of γ_1 chosen compared to the effect of γ_3. Because $\gamma_1 = \gamma_2$ are related to the diffusion time of ligands whereas γ_3 to the bond breaking time, the observed insensitivity is what one can expect when kinetics is dominated by the latter process.

2.5.3. ACKNOWLEDGMENT

We thank Stefano Angioletti-Uberti and Daniele Visco who developed the theory. We thank Ramon van der Valk and Anne Schwabe for technical help and Jérémie Capoulade for help with microscopy.

REFERENCES

[1] M. Mammen, S. K. Choi, and G. M. Whitesides, *Polyvalent interactions in biological systems: Implications for design and use of multivalent ligands and inhibitors,* Angewandte Chemie - International Edition **37**, 2754 (1998).

[2] J. Huskens, *Multivalent interactions at interfaces,* Current opinion in chemical biology **10**, 537 (2006).

[3] T. Satav, J. Huskens, and P. Jonkheijm, *Effects of variations in ligand density on cell signaling,* (2015).

[4] N. J. Boudreau and P. L. Jones, *Extracellular matrix and integrin signalling: The shape of things to come,* (1999).

[5] C. Fasting, C. A. Schalley, M. Weber, O. Seitz, S. Hecht, B. Koksch, J. Dernedde, C. Graf, E. W. Knapp, and R. Haag, *Multivalency as a chemical organization and action principle,* (2012).

[6] X. Tian, S. Angioletti-Uberti, and G. Battaglia, *On the design of precision nanomedicines,* Science Advances **6**, eaat0919 (2020).

[7] M. Liu, A. Apriceno, M. Sipin, E. Scarpa, L. Rodriguez-Arco, A. Poma, G. Marchello, G. Battaglia, and S. Angioletti-Uberti, *Combinatorial entropy behaviour leads to range selective binding in ligand-receptor interactions,* Nature Communications **11**, 1 (2020).

[8] S. Hauert and S. N. Bhatia, *Mechanisms of cooperation in cancer nanomedicine: Towards systems nanotechnology,* Trends in Biotechnology **32**, 448 (2014).

[9] J. Wang, J. Min, S. A. Eghtesadi, R. S. Kane, and A. Chilkoti, *Quantitative study of the interaction of multivalent ligand-modified nanoparticles with breast cancer cells with tunable receptor density,* ACS Nano **14**, 372 (2020).

[10] J. Zhang, Z. Wang, Y. Gao, and Z. S. Wu, *Simple self-assembled targeting dna nano sea urchin as a multivalent drug carrier,* ACS Applied Bio Materials **3**, 4514 (2020).

[11] Y. Zhang, M. Cheng, J. Cao, Y. Zhang, Z. Yuan, Q. Wu, and W. Wang, *Multivalent nanoparticles for personalized theranostics based on tumor receptor distribution behavior,* Nanoscale **11**, 5005 (2019).

[12] S. Li, S. Huang, and S. B. Peng, *Overexpression of g protein-coupled receptors in cancer cells: Involvement in tumor progression,* International Journal of Oncology **27**, 1329 (2005).

[13] M. J. Akhtar, M. Ahamed, H. A. Alhadlaq, S. A. Alrokayan, and S. Kumar, *Targeted anticancer therapy: Overexpressed receptors and nanotechnology,* Clinica Chimica Acta **436**, 78 (2014).

[14] P. A. Koenig, H. Das, H. Liu, B. M. Kümmerer, F. N. Gohr, L. M. Jenster, L. D. Schiffelers, Y. M. Tesfamariam, M. Uchima, J. D. Wuerth, K. Gatterdam, N. Ruetalo, M. H. Christensen, C. I. Fandrey, S. Normann, J. M. Tödtmann, S. Pritzl, L. Hanke, J. Boos, M. Yuan, X. Zhu, J. L. Schmid-Burgk, H. Kato, M. Schindler, I. A. Wilson, M. Geyer, K. U. Ludwig, B. M. Hällberg, N. C. Wu, and F. I. Schmidt, *Structure-guided multivalent nanobodies block sars-cov-2 infection and suppress mutational escape,* Science **371** (2021).

[15] G. J. Doherty and H. T. McMahon, *Mechanisms of endocytosis,* Annual Review of Biochemistry **78**, 857 (2009).

[16] F. J. Martinez-Veracoechea and D. Frenkel, *Designing super selectivity in multivalent nano-particle binding,* Proceedings of the National Academy of Sciences of the United States of America **108**, 10963 (2011).

[17] G. A. Duncan and M. A. Bevan, *Computational design of nanoparticle drug delivery systems for selective targeting,* Nanoscale **7**, 15332 (2015).

[18] S. Wang and E. E. Dormidontova, *Selectivity of ligand-receptor interactions between nanoparticle and cell surfaces,* Physical Review Letters **109** (2012).

[19] G. V. Dubacheva, T. Curk, D. Frenkel, and R. P. Richter, *Multivalent recognition at fluid surfaces: The interplay of receptor clustering and superselectivity,* Journal of the American Chemical Society **141**, 2577 (2019).

[20] R. Lanfranco, P. K. Jana, L. Tunesi, P. Cicuta, B. M. Mognetti, L. D. Michele, and G. Bruylants, *Kinetics of nanoparticle-membrane adhesion mediated by multivalent interactions,* Langmuir **35**, 2002 (2019).

[21] D. D. Iorio and J. Huskens, *Surface modification with control over ligand density for the study of multivalent biological systems,* ChemistryOpen **9**, 53 (2020).

[22] G. V. Dubacheva, T. Curk, B. M. Mognetti, R. Auzély-Velty, D. Frenkel, and R. P. Richter, *Superselective targeting using multivalent polymers,* Journal of the American Chemical Society **136**, 1722 (2014).

[23] G. V. Dubacheva, T. Curk, R. Auzély-Velty, D. Frenkel, and R. P. Richter, *Designing multivalent probes for tunable superselective targeting,* Proceedings of the National Academy of Sciences of the United States of America **112**, 5579 (2015).

[24] M. R. Scheepers, L. J. IJzendoorn, and M. W. Prins, *Multivalent weak interactions enhance selectivity of interparticle binding,* Proceedings of the National Academy of Sciences of the United States of America **117**, 22690 (2020).

[25] N. J. Overeem, P. H. E. Hamming, O. C. Grant, D. Di Iorio, M. Tieke, M. C. Bertolino, Z. Li, G. Vos, R. P. de Vries, R. J. Woods, N. B. Tito, G.-J. P. H. Boons, E. van der Vries, and J. Huskens, *Hierarchical multivalent effects control influenza host specificity,* ACS Central Science **6**, 2311 (2020).

[26] M. Rinaldin, R. W. Verweij, I. Chakraborty, and D. J. Kraft, *Colloid supported lipid bilayers for self-assembly,* Soft Matter **15**, 1345 (2019).

[27] S. F. Shimobayashi, B. M. Mognetti, L. Parolini, D. Orsi, P. Cicuta, and L. D. Michele, *Direct measurement of dna-mediated adhesion between lipid bilayers,* Physical Chemistry Chemical Physics **17**, 15615 (2015).

[28] A. Cossins, *Membrane fluidity in biology, vol. 4, cellular aspects,* International Journal of Radiation Biology and Related Studies in Physics, Chemistry and Medicine **50**, 756 (1986).

[29] S. Chakraborty, M. Doktorova, T. R. Molugu, F. A. Heberle, H. L. Scott, B. Dzikovski, M. Nagao, L. R. Stingaciu, R. F. Standaert, F. N. Barrera, J. Katsaras, G. Khelashvili, M. F. Brown, and R. Ashkar, *How cholesterol stiffens unsaturated lipid membranes,* Proceedings of the National Academy of Sciences of the United States of America **117**, 21896 (2020).

[30] P. Delcanale, B. Miret-Ontiveros, M. Arista-Romero, S. Pujals, and L. Albertazzi, *Nanoscale mapping functional sites on nanoparticles by points accumulation for imaging in nanoscale topography (paint),* ACS Nano **12**, 7629 (2018).

[31] I. Chakraborty, V. Meester, C. V. D. Wel, and D. J. Kraft, *Colloidal joints with designed motion range and tunable joint flexibility,* Nanoscale **9**, 7814 (2017).

[32] P. Varilly, S. Angioletti-Uberti, B. M. Mognetti, and D. Frenkel, *A general theory of dna-mediated and other valence-limited colloidal interactions,* The Journal of Chemical Physics **137**, 094108 (2012).

[33] S. Angioletti-Uberti, P. Varilly, B. M. Mognetti, and D. Frenkel, *Mobile linkers on dna-coated colloids: Valency without patches,* Physical Review Letters **113**, 128303 (2014).

[34] B. M. Mognetti, P. Cicuta, and L. D. Michele, *Programmable interactions with biomimetic dna linkers at fluid membranes and interfaces,* Reports on progress in physics. Physical Society (Great Britain) **82** (2019).

[35] J. SantaLucia, *A unified view of polymer, dumbbell, and oligonucleotide dna nearest-neighbor thermodynamics,* Proceedings of the National Academy of Sciences **95**, 1460 (1998).

[36] S. Azizian, *Kinetic models of sorption: a theoretical analysis,* Journal of Colloid and Interface Science **276**, 47 (2004).

[37] P. K. Jana and B. M. Mognetti, *Translational and rotational dynamics of colloidal particles interacting through reacting linkers,* Physical Review E **100**, 060601 (2019).

[38] T. Curk, J. Dobnikar, and D. Frenkel, *Optimal multivalent targeting of membranes with many distinct receptors.* Proceedings of the National Academy of Sciences of the United States of America **114**, 7210 (2017).

[39] D. Bray, M. D. Levin, and C. J. Morton-Firth, *Receptor clustering as a cellular mechanism to control sensitivity,* Nature **393**, 85 (1998).

[40] J. F. Stefanick, D. T. Omstead, T. Kiziltepe, and B. Bilgicer, *Dual-receptor targeted strategy in nanoparticle design achieves tumor cell selectivity through cooperativity,* Nanoscale **11**, 4414 (2019).

[41] N. R. Markham and M. Zuker, *Dinamelt web server for nucleic acid melting prediction,* Nucleic Acids Research **33** (2005).

[42] S. A. V. D. Meulen and M. E. Leunissen, *Solid colloids with surface-mobile dna linkers,* Journal of the American Chemical Society **135**, 15129 (2013).

[43] J. V. Ginkel, M. Filius, M. Szczepaniak, P. Tulinski, A. S. Meyer, and C. Joo, *Single-molecule peptide fingerprinting,* Proceedings of the National Academy of Sciences of the United States of America **115**, 3338 (2018).

[44] S. Preibisch, S. Saalfeld, J. Schindelin, and P. Tomancak, *Software for bead-based registration of selective plane illumination microscopy data,* Nature Methods **7**, 418 (2010).

[45] S. Angioletti-Uberti, P. Varilly, B. M. Mognetti, A. V. Tkachenko, and D. Frenkel, *Communication: A simple analytical formula for the free energy of ligand–receptor-mediated interactions,* The Journal of Chemical Physics **138**, 021102 (2013).

[46] S. Angioletti-Uberti, *Exploiting receptor competition to enhance nanoparticle binding selectivity,* Physical review letters **118** (2017).

[47] P. J. Sanstead and A. Tokmakoff, *Direct observation of activated kinetics and downhill dynamics in dna dehybridization,* Journal of Physical Chemistry B **122**, 3088 (2018).

3

BOND FORMATION AND DIFFUSION OF MULTIVALENT COLLOIDAL PARTICLES

Clustering of ligands and receptors between biological interfaces upon binding is important for cell-cell adhesion, signalling, T cell activation and transport. The accumulation of ligands and receptors is characteristic for multivalent surfaces with fluidic properties. Theoretical and experimental works have provided insights into ligand and receptor recruitment but a direct visualisation of the ligand and receptor clustering in time between two multivalent surfaces is still missing. Here, we use membrane coated colloids, functionalized with DNA linkers that can multivalently bind to a target surface with complementary DNA linkers. Upon binding, we visualize the ligand and receptor interactions in the contact area with fluorescence microscopy and Foerster Resonance Energy Transfer (FRET). We observe the recruitment of ligands and receptors towards the contact area, while the colloid diffuses on the target surface. We discover a slow down of the colloidal motion during the accumulation of linkers. Depending on the interaction strength of the linkers, we find different final patch sizes. These results provide unprecedented quantitative insights into the timescale of multivalent binding and its effect on the motion of the ligand-bearing receptors on the surface.

3.1. INTRODUCTION

The interaction between two biological interfaces is mediated by specific binding between ligands and receptors that are both anchored in a membrane [1, 2]. Often, these interactions consist of multiple weak bonds between ligands and receptors that - because of their surface mobility in the membrane - can accumulate at the contact area. This process, also called receptor clustering, is crucial for signalling during chemotaxis of *Escherichia coli* [3], T cell activation triggered by T cell receptor nanoclusters [4], and integrin and cadherin clusters mediated cell adhesion [5–7].

The involved multivalently bound entities furthermore can undergo lateral diffusion on the membrane themselves due to its fluid character [8]. This property is well known for virus particles that first bind multivalently to cell membrane receptors and subsequently they show lateral movement via the cell receptors on the cell surface prior to uptake via endocytosis [9–14].

A combination of strong binding and high diffusive motion is also necessary for transporting a cargo along the cell membrane to a desired location, not only for virus particles trying to reach a suitable spot on the cell membrane for internalization but also for drug delivery applications. Achieving this requires an understanding of receptor mediated transport along the cell membrane and its dependence on the receptor cluster size.

The ideal experimental system to study both the adsorption and diffusive motion of multivalent particles needs to mimic the diffusive motion of receptors and ligands [15]. The adsorption of DNA coated gold nanoparticles [16] and biotin labeled giant unilamellar vesicles (GUV) [17] onto supported lipid bilayers (SLBs) gave insights into the receptor recruitment upon multivalent binding. By tracking DNA functionalised nanoparticles [18] and DNA functionalised small unilamellar vesicles (SUV) [19] adsorbed to a SLB, it has been shown that increasing the number of bonds decreases the diffusive motion of the attached particles. Previous work on colloid-colloid interactions found that the mobility of bound colloids depends on the ligand-receptor surface density, which was hypothesized to stem from the bonding patch [20]. Fluorescent microscopy of DNA-functionalized microdroplets [21] and GUVs [17, 22, 23] confirmed that the final bond is a result of receptor clustering. However, visual confirmation of the direct correlation between the bond formation and a slow down or arrest of the motion is missing. In fact, the formation of the multivalent bond in time itself has never been observed quantitatively. Even more so, its dependency on the multivalent character of the bond, and hence on the interaction strengths and surface densities of the ligands and receptors, is experimentally unexplored.

We here investigate the correlation between bond formation and arrest of motion using a dedicated model system of micrometer-sized colloids and surface, where we can measure linker accumulation in the binding patch *in-situ* through a fluorescent signal [24]. Since both, the particle and target surface are coated with a lipid membrane, ligands and receptors are both mobile on the surface. This allows us to directly observe the cluster formation of ligands and receptors and simultaneously track the motion of the particle. After the initial binding of a particle to the surface, we observe an intensity increase in the bond area in time, which implies that the DNA linkers are recruited towards the contact area, and a simultaneous decrease in the particle's diffusivity. The recruitment continues until a binding patch has been formed such that there is a dynamic

equilibrium between the bound and unbound ligand-receptor pairs that is determined by the balance between various energetic and enthalpic contributions. We link the binding strength of individual ligand-receptor pairs and their surface density to the size and density of ligand-receptor pairs in the patch and the loss of mobility. These observations provide unprecedented quantitative measurements on the multivalent bond formation and corresponding slow-down of diffusion of the multivalently-binding entity.

3.2. RESULTS

3.2.1. MULTIVALENT BOND FORMATION AND VISUALIZATION

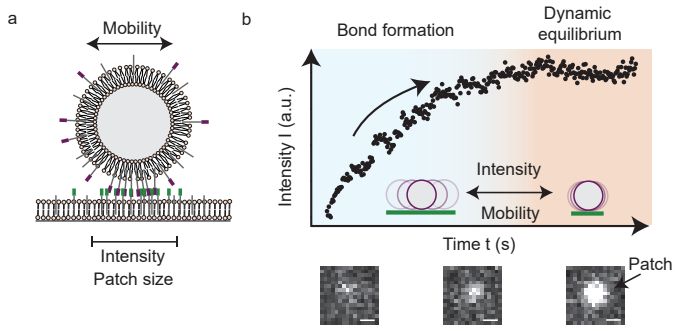

Figure 3.1: **Multivalent binding mediated by mobile DNA linkers.** a) The experimental model system consists of colloidal particles functionalized with DNA linkers that form the ligand and receptor system. The colored end of the DNA strand represents the single stranded overhang (sticky end). We use two different fluorophores to distinguish the DNA linker on the colloid and surface. Additionally, passive DNA strands without a sticky end are inserted into the lipid bilayer. Furthermore, we can track the location of the fluorescent signal to measure the diffusion of the colloidal particle. b) With this experimental setup, we can measure the intensity I and size of the patch in time, and connect it to the mobility. Fluorescent images illustrate the formation of the patch over time. The intensity I increases over time and shows that ligands and receptors are recruited towards the particle-surface contact area until the patch reaches a dynamic equilibrium. In the dynamic equilibrium, the maximum number of bonds $N_{B,max}$ is reached and the patch is fully established. The scale bar is 500 nm.

We investigate the correlation between the ligand and receptor bond formations and mobility of the colloid using colloidal probe particles (silica, $2.21 \pm 0.06 \mu$m) and a glass surface that are both coated with a supported lipid bilayer (SLB), see Fig. 3.1a. As binding sites we anchor double stranded DNA via a cholesterol molecule into the SLB to obtain full mobility of the ligands and receptors. Each DNA molecule consists of a single stranded overhang (sticky end) such that the DNA molecules on the colloid (ligands) can interact with the DNA on the target surface (receptors). We visualize the bond formation using Foerster Resonance Energy Transfer (FRET) between fluorophores placed on the $3'$ end of the ligand and receptor. We observe a fluorescent signal only when a receptor and ligand interact. Hence, when the colloids are still freely diffusing in solution, no FRET signal is being detected. See Materials and Methods for details.

The moment the colloid reaches the target surface we observe an increase in the FRET signal in the contact area between colloid and surface, see Fig. 3.1a and b. The intensity of the bonding patch rapidly increases and saturates at a constant value after

patch formation has completed. This constant intensity implies that a dynamic equilibrium state has been reached in which individual ligand-receptor pairs may unbind or bind, but the overall patch size and strength, i.e. the total number of bound ligand-receptor pairs, and hence intensity remains constant [24]. With this experimental setup we can simultaneously track the location of the FRET signal over time and from this extract the diffusive motion of the colloid, which allows us to directly link the results to the number of bonds in the patch. In the following, we will experimentally quantify the multivalent bond formation in time, and investigate how and under what circumstances its appearance affects the colloidal mobility.

3.2.2. PATCH FORMATION AND SLOW DOWN OF DIFFUSIVE MOTION

It has been hypothesized that bonds form by the accumulation of linkers and that this accumulation is causing an arrest of the bead motion [18–20]. We investigate the correlation between bond formation and motion by tracking the FRET signal of individual colloids coated with 1500 μm^{-2} ligands that are binding to a surface functionalized with 450 μm^{-2} receptors and enthalpy of $\Delta G^0 = -17$ k_BT(11 bp-seqA). An exemplary curve of the intensity of the FRET signal in time is shown in Fig. 3.2a. The intensity of the FRET signal shows an initial increase until it reaches a plateau around 20 s and continues until saturation at approximately 200 s. The change in slope suggests that the recruitment of receptors and ligands to the binding patch slows down after a specific time, which we will be focusing on in the following.

Initially, the receptors and ligands can diffuse unobstructed into the contact area and their diffusion inside and outside the patch area are the same. However, in time, the bonding area gradually becomes filled up with bound ligand-receptor pairs. This sterically hinders the diffusion of other ligands and receptors towards the patch, as well as slows down their diffusion inside the patch. In addition, the local accumulation of ligand-receptor pairs increases the concentration of cholesterol in the membrane area of the binding patch, which affects the fluidity of the membrane and further slows down the diffusion of both bound and unbound ligands and receptors [25, 26]. As a consequence, further diffusion, binding, and accumulation between individual linkers in the patch decreases and the intensity of the FRET signal saturates to a steady value.

To investigate how this transition affects the motion of the ligand-bearing entity, the colloid, we track the spatial coordinates of the patch center during bond formation, see Fig. 3.2b. Initially, the colloid moves significantly between two frames, indicated by the circles, but then gradually slows down, until the particle becomes stationary at around 150 s. Clearly, the bond formation, strongly affects the mobility of the colloidal particle, which is confirmed by the decrease of the displacement d of the colloid in time, see Fig. 3.2c. In the first 20 s we observe a significant decay of the displacement between two frames, which subsequently transitions into a slower decay. Various effects may cause this slow-down of the colloidal diffusion, similar to what has been hypothesized previously for the mobility of colloidal joints after bond formation [20]: a higher number of bonded ligand-receptor pairs and a larger patch size increases friction for the patch diffusion inside the supported lipid bilayers. Secondly, the gradual accumulation of cholesterol moieties in the patch area of the membrane affects the membrane viscosity and hence not only the diffusion of individual ligands and receptors but also the

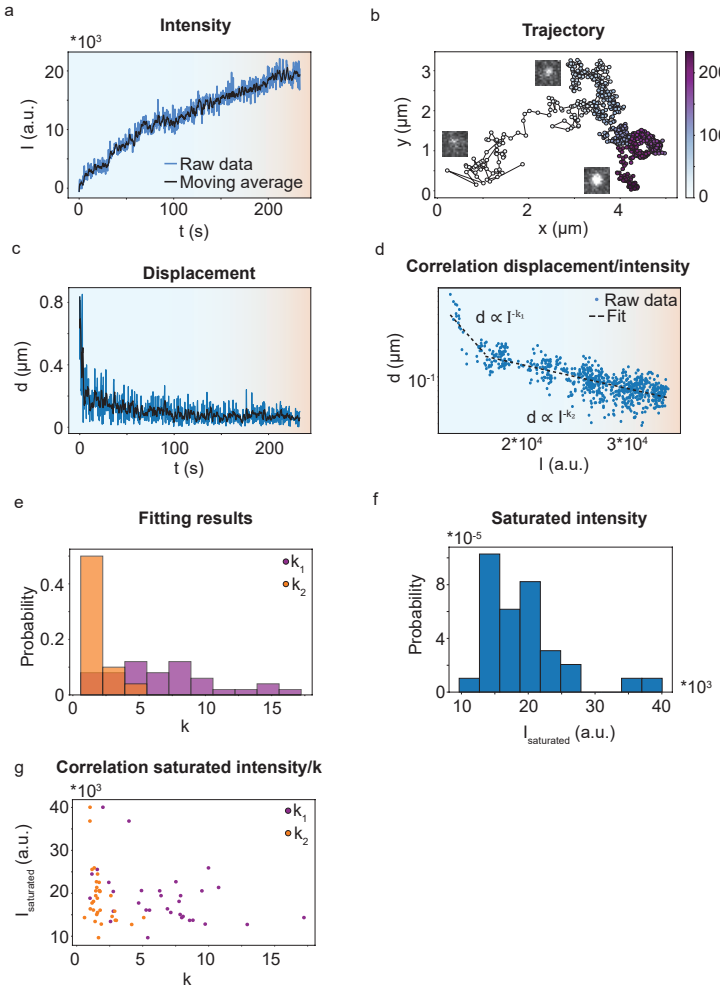

Figure 3.2: **Patch formation.** a) Intensity as a function of time shows the recruitment of ligands and receptors with an enthalpy of $\Delta G^0 = -17 k_B T$(11 bp-seqA) towards the contact area. b) Trajectory of colloid during bond formation. c) Displacement d between two consecutive frames extracted from a). After approximately 20 s, the exponential decay transitions into a linear decrease until the displacement reaches a steady value. d) Displacement d as a function of intensity I on a log-log scale. We observe two regimes with distinctly different power laws and a transition at approximately 50 s. We fit both regimes with a powerlaw yielding two exponents k_1 and k_2. e) Linear regression on a log-log scale of $d(I)$ yields two exponents k_1 and k_2 that vary between $0-17$. Furthermore, the exponent k_1 shows larger values compared to k_2. f) Distribution of $I_{\text{saturated}}$. g) $I_{\text{saturated}}$ as a function of k_1 and k_2 demonstrates that large exponents are common for low $I_{\text{saturated}}$. To track the colloids and measure the intensity, we used trackpy.

diffusion of the patch and thus colloid as a whole.

Comparing the intensity of the FRET signal and the displacement of the colloidal particle in time, we find a clear correlation between the two parameters, see Fig. 3.2d. Interestingly, on a log-log scale we can identify two time-intervals with different slopes. This implies two distinct power-law relationships $d \propto I^k$ between the displacement d and the FRET intensity I. We extract the exponents k_1 and k_2 for the two regimes by performing a linear regression, and plotting their probability density function in Fig. 3.2e. In the first regime, we find a narrow distribution of k_1 values varying between $1-6$, whereas the second slope k_2 varies over a greater range, namely between $1-17$. Plotting the saturated intensities I_{sat}, which represents the intensity of the fully formed patch in the dynamic equilibrium, we observe a similarly broad distribution. The latter stems from the broad distribution of the ligand density on the colloids, which is known to vary by up to an order of magnitude in a sample [27]. We speculate that the ligand density on the colloids may also affect the dynamics of the patch formation and connected slow down of the colloid displacement, which would be reflected in the large spread of k_2 [20, 27]. The more narrow distribution of k_1 that describes the dynamics of the initial regime suggests that this regime corresponds to unhindered diffusion, binding and accumulation of the ligands and receptors in the bond area. Therefore, it is reasonable to expect that a spread in the ligand density on the colloidal particle has a less pronounced effect on the initial dynamics, and hence a smaller spread in k_1.

3.2.3. PATCH AREA AND INTENSITY IN DYNAMIC EQUILIBRIUM

In the previous subsection we have shown that with increasing patch intensity, we observe a striking reduction in the surface mobility of the colloidal particle. We attributed this decrease to the increase in the number of ligand-receptor bonds and the growth of a binding patch. In the following, we consider what dictates the maximum value for these parameters.

Assuming a rigid geometry of the particle and a sufficiently high receptor density on the surface, the determining factors have to be the ligand density and binding strength between ligand-receptor pairs as they are the two remaining factors that contribute to the multivalent character of the bond. Therefore, we measure the patch size and intensity over a range of ligand densities and different sticky ends. An overlay of the brightfield image of the colloid with the FRET channel verifies that the fluorescent signal stems from ligand and receptor interactions in the contact area of the colloid, see Fig. 3.3a. Using a canny-edge detection algorithm, see Materials and Methods for details, we extract the patch size and intensity based on the FRET images, see Fig. 3.3a and Fig. 3.3b.

First, we measure the size of the patch area for colloids functionalised with DNA linkers with three different sticky ends with an enthalpy ranging between -11 k_BT to -17 k_BT. All patch areas increase with increasing ligand density σ_L until they reach a maximum value and decrease again. To compare the result with the geometrically expected maximum patch size, we assume that the patch is circular and limited by the maximum bond length L, defined by the length of a ligand and receptor after hybridization. Together with the colloid radius R_C we expect the maximum patch size of $A_{\text{patch,max}} = 2\pi R_C L = 0.36\ \mu\text{m}^2$, see 3.3a. Surprisingly, the binding patch of colloids functionalised with DNA linkers with 8 bp sticky ends increase slower compared to colloids functionalised with

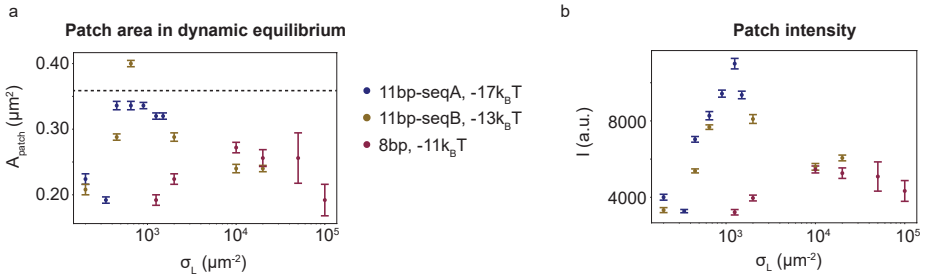

Figure 3.3: **Patch area and intensity in dynamic equilibrium.** a) Patch sizes A_{patch} of colloids coated with different ligand densities for three different sticky ends. All patch sizes increase with increasing ligand density until they reach a maximum and decrease again. The maximum A_{patch} differs between sticky ends. Colloids functionalised with 8 bp sticky ends reach the maximum value at higher values of σ_{L} compared to colloids functionalised with 11 bp sticky ends. Dashed line indicates the geometrical expected maximum patch area. b) I as a function of σ_{L} for 8 bp and 11 bp sticky ends. The data in (a) and (b) was measured with a canny edge detection algorithm.

11 bp sticky ends, even though they are coated with an up to 100 × higher ligand density. In addition, the maximum value for the 11bp sticky ends are around $A_{\text{patch,max}}$, whereas the 8 bp sticky end yields a maximum patch size of approximately 0.28 μm^2. We hypothesize that this behavior stems from the multivalent nature of the bond. Upon binding, the ligands on the colloid have to diffuse towards the contact area, which can lead to a concentration difference of ligands on the colloid. The energy released upon binding compensates for this inhomogeneity of ligand density and hence, the longer the sticky end, the more easily ligands can overcome the energy barrier. Due to the cost of binding, the 8 bp sticky ends are shifted to larger σ_{L} and, additionally, show a slower increase in A_{patch} because the enthalpy is $(2-6)$ k$_{\text{B}}$T lower compared to the 11 bp sticky ends. Another possible explanation is that the close packing of DNA inside the patch induces repulsion between the dsDNA backbone due to the negative charge. If the enthalpy of the bonds is strong, this effect is negligible compared to low enthalpies, where the ligand-receptor bond cannot compensate for the repulsion.

A second intriguing observation in Figure 3.3a is that one measured patch size of the 11 bp-seqB lies above the geometrically possible maximum patch size. This observations may point to a deformation of the supported lipid bilayer both on the colloid and/or the target surface. Such deformations would effectively increase the area for ligands and receptors to bind, as has been hypothesized by [20] and [18]. In addition, we find that the patch areas for the 11 bp strands tend to be higher when saturated than for the 8 bp strand. This observation suggests that an increase in σ_L does not only increase the attraction between ligands and receptors but hinders the system to bind, however it remains unclear to which degree σ_L induces a repulsion.

Finally, we observe a drop in the patch size for colloids functionalised with 8 bp and 11 bp sticky ends at high ligand concentrations σ_{L}. While the origin of this effect is as of yet unclear, we suspect that above a certain ligand density, the colloidal particles experience an increased repulsion that stems from steric interactions caused by the increased number of ligands [28]. Moreover, close packing of the linkers restrict their freedom of

motion in space and results in a configuration, where the linkers all point straight up, which also increases the steric repulsion.

Similar to the patch size, the intensity I, which is the product of the mean intensity of the patch and the number of pixels that span the patch area, integrated over the patch area also increases as a function of ligand density, see Fig. 3.3b. Again, the colloids functionalised with 11 bp linkers reach saturation at lower σ_L compared to colloids functionalised with 8 bp DNA linkers. Note, that the absolute intensity values of the fluorescent signal of the 11 bp DNA linkers are not directly comparable to the 8 bp DNA linkers due to different flurophores on the DNA strands. Comparing the integrated intensity with the patch size with increasing ligand density, we observe similar trends for both values: At a specific σ_{L} the curves reach a maximum and with a further increase of σ_{L}, the intensity and area decreases.

Between different strands, and hence different interaction strengths, we observe three effects: (1) the curves are shifted along σ_{L}, (2) their slope changes and (3) the intensity and patch do not saturate but decrease. Longer sticky ends with higher interaction strengths show the same intensity values already at lower ligand densities. This can be understood from the multivalent character of the bond. Upon binding of ligands or receptors their motion is significantly confined, from either the whole colloid or the target surface to the bonding patch [29]. In addition, the recruitment of ligands towards the contact area can lead to a concentration difference in ligand density inside and outside the patch area on the colloid surface. This loss of translational entropy and ligand density inhomogeneity needs to be compensated by a gain in combinatorial entropy and binding enthalpy. The higher the enthalpy gain from binding, the easier the system can make up for the entropy loss, and hence form the same number of bonds already at lower ligand density. As a result, the integrated intensity of colloids coated with 11 bp linkers saturates earlier than for those coated with 8 bp linkers.

We believe that the physical mechanism for this shift is similar to the one observed for the binding probability of colloids as a function of ligand densities for different linker lengths [24]. However, there is also a notable difference namely that ligands with longer sticky ends show a less steep binding probability with increasing receptor density, whereas the average patch intensity and hence number of bound ligand-receptor pairs is steeper for longer sticky ends. This can be explained by the dynamic unbinding and binding of receptor and ligand interactions. The stronger the interactions, the longer it takes for the bond to break and diffuse out of the patch. Therefore, we expect a faster accumulation of linkers in the patch for the 11 bp linkers. This observation confirms our findings that the dynamic binding kinetics are crucial for the binding probability of colloids.

A recent study with DNA functionalized droplets binding to complementary DNA on a surface investigated the patch size and intensity as a function of DNA density on the droplet (σ_L) [21]. They find that the DNA density on the vesicle governs the final patch size, confirming our findings. However, they do not observe a decrease in A_{patch} at large DNA densities but an asymptotic increase of A_{patch} as a function of σ_R until saturation. Moreover, they propose that the receptors and ligands inside the patch tend to migrate towards the outer edge of the patch at high density to avoid intermolecular interaction penalties, leading to a ring formation. Due to experimental limitation, we

cannot observe the ring formation. To obtain a better estimate of the patch size and shape, we would need to increase the colloid radius.

3.2.4. DIFFUSIONCOEFFICIENT IN DYNAMIC EQUILIBRIUM

An interesting feature of fully mobile ligands and receptors is that even when they are bound, they can still diffuse within the bond area and simultaneously move collectively as a complex. The same should hold for our experimental model system, where a bound colloid should still be able to diffuse on the target surface, albeit with lower diffusion constant due to the increased friction of the patch of linkers within the membrane. However, diffusion might even arrest fully, as we showed in Figure 3.2b and c, where the displacement strongly reduced in time.

To elucidate how this process depends on the interaction strength between individual ligands and receptors and the ligand density, we determine the diffusion coefficient of colloids with fully developed bonding patches. By measuring the displacement of the colloid from the tracked FRET signal over time with a python tracking algorithm trackpy [30] we can calculate the diffusion coefficient D. Fig. 3.4a shows D for the 8 bp at $\sigma_L = 2000\mu\text{m}^{-2}$. We set a threshold for D for unbound colloids, which we determined from unbound colloids as a reference. We consider four different ligand-receptor interaction strengths, by employing two DNA linkers with 11 bp sticky ends, one with an 8 bp sticky end and one with a 6 bp sticky end. We observe a decrease in D with increasing ligand density σ_L. Independent of the enthalpy of the sticky end, the lowest values we find for the diffusion coefficient lies between $0-0.1\ \mu\text{m}^2/\text{s}$.

However, the transition from a freely diffusive motion of the colloid to nearly complete stillness depends on the strength of the DNA linker. The diffusion of colloids equipped with 11 bp-seqA linkers is almost constant and close to the smallest observed values for D, whereas the diffusion constant of colloids functionalized with the 11 bp-seqB shows a smooth decay until complete arrest of motion. Interestingly, the diffusion of colloids functionalized with 8 bp first decreases slowly until it suddenly drops to $D = 0\ \mu\text{m}^2/\text{s}$. The colloids equipped with 6 bp linkers show a sharp decrease with σ_L, except for the highest σ_L where an increase of D can be seen. This might stem from a decrease in patch size due to steric repulsion, an effect similar to the one that was observed for the decreased area size with σ_L in Fig. 3.3a.

Plotting D as a function of I does not show a clear relation between the two parameters, see Fig. 3.4c. Note, that we did not include the 6 bp sticky ends in the analysis, because the signal to noise ratio of the patch makes it challenging to analyse and prone to false results. We suspect that the decreasing A_patch and I at large σ_R yield a nonlinear dependence between the parameters and D. To test our hypothesis, we exclude the datapoints that belong to the range of σ_L, where we observed the decrease in A_patch, see Fig. 3.4d. Now, the 11 bp-seqB and 8 bp fall on a line, but the 11 bp seq-A shows a constant D independent of I. Previous experimental and theoretical work have proposed the 'free draining model' to describe the diffusion D as a function of the number of interactions[18, 19].

$$D = \frac{1}{N_B}, \tag{3.1}$$

where N_B are the number of bonds. Our findings do not support a powerlaw between D and I. Moreover, the free draining model describes systems with few binding sites on the nanoscale. This observation suggests that the lengthscale of the system changes the underlying theory to describe the system. On the microscale, within a short timescale hundreds of bonds are formed, which has a much larger effect on A_{patch} and D, as it holds for nanoparticles.

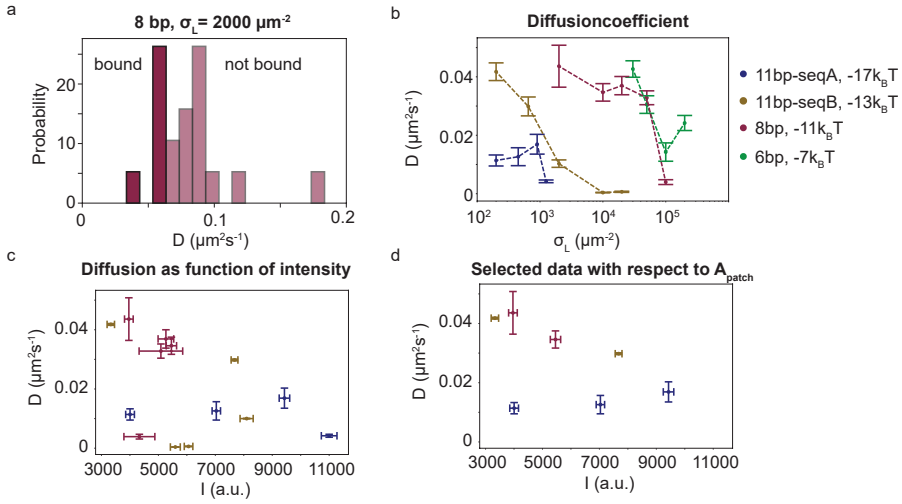

Figure 3.4: **Diffusioncoefficient in dynamic equilibrium.** a) Distribution of D for 8 bp sticky ends at σ_R = 10000μm^{-2}. The lighter region indicates D for unbound colloids and is excluded from the average computation. b) Diffusioncoefficient D for four different sticky ends. Colloids functionalised with 11 bp sticky ends have an approximately constant diffusioncoefficient of 0.15μm^2/s. Weaker interactions show a larger decrease with increasing ligand density until they reach a stationary value. Colloids functionalised with 8 bp sticky ends plateau at $D = 0.035\mu$m^2/s and then drop to $D \approx 0\mu$m^2/s. The shortest sticky end drops similarly to the 8 bp sticky ends but D does not saturate and increases again at high σ_L. c) D as a function of I for 8 bp, 11 bp seq-A and 11 bp seq-B. d) Same plot as in (c) but only datapoints before the decrease in A_{patch} are included.

3.3. CONCLUSION

The diffusion of a multivalent particle is determined by the number of bonds in the patch area. In this chapter, we have employed an experimental model system to study bond formation and diffusion of a fully mobile system on the ligand-receptor level. We directly visualised the spatial organisation of the ligand and receptors inside the patch area and linked our results to the diffusion of the colloid. We have shown that the bond formation is governed by the ligand and receptor recruitment. The final patch size in the dynamic equilibrium can be tuned with the ligand density and interaction strength, which has a direct impact on the diffusive motion of the bound colloid: an increasing number of σ_L gradually decreases the diffusive motion of the colloid until its motion arrests almost completely.

Subsequent studies with this model system can contribute to the understanding of receptor recruitment on the surface, leading to receptor depletion on the surface, by

investigating the bond formation for different concentrations of colloidal particles in solution. Different diffusion coefficients of ligands and receptors, which are typical for biological membranes, could have an impact on the timescale of binding. This could be investigated by tuning the membrane composition on the colloid and target surface in our experimental system. The insights gained in this study might be important for the self-assembly of colloid supported lipid bilayers into flexible microstructures, because they show under what conditions bond flexibility arrests. Lastly, our observations might help in designing a drug-delivery carrier that shows a high binding probability and diffusion on the target surface.

3.4. METHODS

3.4.1. SUPPORTED LIPID BILAYER FORMATION

To ensure full mobility of the binding sites, we coated the surfaces of the probe particle and target surface with a supported lipid bilayer (SLB). 18 : 1 DOPC lipids [Avanti Polar Lipids] were stored in chloroform, so we first transfered the lipids with gastight syringes into a glass vial. We gently blew with nitrogen to evaporate the chloroform and we additionally placed the glass vial into a vacuum dessiccator overnight to make certain that all chloroform has been evaporated. Next, we resuspended the dried lipids in Tris Acetate-EDTA-NaCl (TAE, 100 mM NaCl, pH=8,[Formedium]) and vortexed the solution for 30 min. During this process, the lipids formed giant unilamellar vesicles (GUV) in solution. Small unilamellar vesicles (SUVs) were prepared by pushing the GUVs through an Avanti mini extruder with a membrane pore size of 30 nm [Avanti Polar Lipids]. This process was repeated until the final solution is transparent.

The SLB is formed by spreading SUVs on a coverslip. This process is very sensitive to the surface properties of the glass, which is why we thoroughly cleaned the glass coverslip [VWR] and glass microscope slide [VWR] before use. In doing so, we sonicated the coverslips and glass microscope slides each in 2%(volume per volume) Hellmanex solution, acetone (> 99.9%) and potassium hydroxide solution (KOH,1M, [Merck]). Between each change of solution, we rinsed the glassware with MilliQ.

All experiments were performed in a flow channel, which consisted of a layer of Parafilm placed between a coverslip and microscope slide. We cut out a 24×2 mm channel in a strip of parafilm and placed it between the cleaned coverslip and microsope slide. Placing the whole construct on a hot plate at 125° melted the parafilm and fused all components together. First, we flushed buffer through the channels and after that we added SUVs and incubated the membranes for 30 min at room temperature. Then, we washed the channels with buffer at 4× the volume of the channel to remove SUVs from solution.

Commercial silica spheres [Microparticle GmbH] of 2.12 ± 0.06 μm diameter were mixed with SUVs and incubated for 60 min at room temperature on an end-over-end tumbler at 8 rcf to avoid sedimentation. Next, we washed the solution three times by centrifuging for 1 min at 2000 rcf and replacing the supernatant with fresh buffer. The last exchange of the supernatant was done with buffer used for imaging and which consisted of 0.8% dextrose, 1 mg/mL glucose oxidase, 170 mg/mL catalase and 1 mM Trolox [$(\pm) - 6-$hydroxy$-2,5,7,8-$tetramethylchromane$-2-$ carboxylic acid, 238813] [Merck].

3.4.2. DNA FUNCTIONALISED SURFACES

Each ssDNA strand ([Integrated DNA Technologies, Inc.],[Eurogentec], [IBA]) with a sticky end were hybridised with a 77 bp ssDNA to form a double stranded backbone, see Tab. 3.1. The two ssDNA strands are annealed up to 95°C and gradually cooled down by 0.2°C/min in Tris Acetate-EDTA-NaCl (TAE, 100 mM NaCl, pH=8,[Formedium]) buffer in a thermocycler. The final products were stored in TAE-NaCl buffer at 4°C. We used sticky ends ranging between 6 bp - 11 bp ($\Delta G^0 = -7\ k_BT - (-17)\ k_BT$).

The hybridised product has a double cholesteryl-TEG anchor that can integrate into the SLB. By adding different concentrations to the membrane coated colloids and target surface, we could tune the final density of DNA on the surface. After an incubation of 60 min, we washed the samples as described in Sec. 3.4.1. We note that the resulting concentration of DNA linkers might be different from the nominal concentration we report in the manuscript. For all experiments, we kept the maximum number of DNA strands per μm^2 constant to ensure constant membrane properties.

3.4.3. DATA ACQUISITION

Fluorescent microscopy data was acquired with Total Internal Reflection (TIRF) microscopy on an inverted microscope (Nikon Ti2-E) upgraded with an azimuthal TIRF / FRAP illumination module (Gata systems iLAS 2) equipped with a 100x oil immersion objective (Nikon Apo TIRF, 1.49NA). By using dual color imaging, we alternated between the donor (561 nm) and acceptor (640 nm) wavelength (Cairn Research Optosplit II By-Pass, EM-CCD Andor iXON Ultra 897), resulting in a Foerster Resonance Energy Transfer (FRET) signal, if the two complementary sticky ends hybridised. Additionally, we acquired a Brightfield image to detect the colloids on the surface (CCD Retiga R1).

3.4.4. IMAGE ANALYSIS

First, we averaged the acquired FRET images over 4 consecutive frames to reduce high frequency noise. With *Trackpy* we located the fluorescent patches in the FRET images and extracted the integrated intensity and spatial coordinates over time during bond formation. Additionally, we used *Trackpy* to extract the spatial coordinates of the patch. *Trackpy* is based on the Crocker-Grier algorithm [31]. We set a fixed mask size and threshold to detect the maximum fluorescent pixels that belong to a patch. The threshold is based on visual inspection after tracking and chosen such that the algorithm does not account for noise. As a result, we obtained for each colloid in the field of view spatial coordinates, which we used to compute the mean square displacement (MSD) leading to the diffusion coefficient D of bound colloids to the SLB. The D for 6 bp sticky ends at $\sigma_R = 10000\ \mu m^{-2}$ estimates D for unbound colloids.

The patch size has been determined via a Canny edge detection algorithm implemented in Python [32]. Prior to analysis, we normalised the images with the maximum fluorescent signal and performed a gaussian blur to reduce noise. The width of the Gaussian was $\sigma = 1$ and was chosen as small as possible to reduce the smoothing of the edges, which effectively increases the size of the patch. The algorithm detects gradient changes in the intensity along the pixels, which defines the edges. Further analysis with hysteresis thresholding on the detected gradient results in the final edge. Therefore, we set a high and low threshold to 0.2 and 0.9, respectively. The absolute values of the patch size

Table 3.1: **List of all DNA sequences.**

Name	Sequence (5′ to 3′)	5′	3′
Receptor/Ligand	TTTATCGCTACCCTTCGCACA GTCACCTTCGCACAGTCACAT TCAGAGAGCCCTGTCTAGAGA GCCCTGCCTTACGA-*sticky end*	Cholesterol-TEG	*fluorophore*
Receptor/Ligand backbone	TCGTAAGGCAGGGCTCTCTAG ACAGGGCTCTCTGAATGTGAC TGTGCGAAGGTGACTGTGCGA AGGGTAGCGATTTT	-	Cholesterol-TEG
Inert strand A	CGTAAGGCAGGGCTCTCTAGA TTGACTGTGCGAAGGGTAGCG ATTTT	-	Cholesterol-TEG
Inert strand B	TTTATCGCTACCCTTCGCACA GTCAATCTAGAGAGCCCTGCC TTACGA	Cholesterol-TEG	-
receptor backbone	TCGTAAGGCAGGGCTCTCTAG ACAGGGCTCTCTGAATGTGAC TGTGCGAAGGTGACTGTGCG AAGGGTAGCGATTTT	Cholesterol-TEG	-
receptor	TTTATCGCTACCCTTCGCACA GTCACCTTCGCACAGTCACAT TCAGAGAGCCCTGTCTAGAGA GCCCTGCCTTACGA-*sticky end*	Cholesterol-TEG	Cy3
ligand *sticky end*	GTAGAAGT-Atto647N (8 bp), TTATAATGAAT-Cy5 (11 bp seq-B), GTAGAAGTAGG-Cy5 (11 bp seq-A)	-	*fluorophore*
receptor *sticky end*	ACTTCTAC-Cy3 (8 bp), ATTCATTATAA-Cy3 (11 bp seq-B), CCTACTTCTAC-Cy3 (11 bp seq-A)	-	*fluorophore*

are sensitive to the parameters chosen for the canny edge detection. However, we tried different methods and we observe the same trends with increasing ligand density only shifted along the y-axis, providing confidence that a comparison between different linkers can be trusted. However, we note that each detected signal represents a point spread function and hence the detected signal is larger than expected, especially for high values of the intensity, adding a difficult to estimate uncertainty to our measurements. To exclude non-physical results from tracking errors, we set a threshold for A_{patch} as three times the maximum possible patch size.

3.5. ACKNOWLEDGEMENT

We thank Thijs van Schoor and Laurie Salvadora van de Weerd for their contribution to the data analysis and Jos Zwanikken for useful discussions.

REFERENCES

[1] J. Huskens, *Multivalent interactions at interfaces,* Current opinion in chemical biology **10**, 537 (2006).

[2] L. B. Freund and Y. Lin, *The role of binder mobility in spontaneous adhesive contact and implications for cell adhesion,* Journal of the Mechanics and Physics of Solids **52**, 2455 (2004).

[3] V. Sourjik, *Receptor clustering and signal processing in e. coli chemotaxis,* Trends in Microbiology **12**, 569 (2004).

[4] S. V. Pageon, T. Tabarin, Y. Yamamoto, Y. Ma, P. R. Nicovich, J. S. Bridgeman, A. Cohnen, C. Benzing, Y. Gao, M. D. Crowther, K. Tungatt, G. Dolton, A. K. Sewell, D. A. Price, O. Acuto, R. G. Parton, J. J. Gooding, J. Rossy, J. Rossjohn, and K. Gaus, *Functional role of t-cell receptor nanoclusters in signal initiation and antigen discrimination,* Proceedings of the National Academy of Sciences **113**, E5454 (2016).

[5] R. Changede and M. Sheetz, *Integrin and cadherin clusters: A robust way to organize adhesions for cell mechanics,* BioEssays **39**, 1 (2017).

[6] E. Sackmann and A.-S. Smith, *Physics of cell adhesion: some lessons from cell-mimetic systems,* Soft matter **10**, 1644 (2014).

[7] L. Li, X. Wang, H. Wu, Y. Shao, H. Wu, and F. Song, *Interplay between receptor-ligand binding and lipid domain formation depends on the mobility of ligands in cell-substrate adhesion,* Frontiers in Molecular Biosciences **0**, 138 (2021).

[8] K. Jacobson, P. Liu, and B. C. Lagerholm, *The lateral organization and mobility of plasma membrane components,* Cell **177**, 806 (2019).

[9] C. J. Burckhardt and U. F. Greber, *Virus movements on the plasma membrane support infection and transmission between cells,* PLoS Pathogens **5** (2009).

[10] H. Gao, W. Shi, and L. B. Freund, *Mechanics of receptor-mediated endocytosis,* Proceedings of the National Academy of Sciences **102**, 9469 (2005).

[11] M. Müller, D. Lauster, H. H. Wildenauer, A. Herrmann, and S. Block, *Mobility-based quantification of multivalent virus-receptor interactions: New insights into influenza a virus binding mode,* Nano Letters **19**, 1875 (2019).

[12] N. Peerboom, S. Block, N. Altgärde, O. Wahlsten, S. Möller, M. Schnabelrauch, E. Trybala, T. Bergström, and M. Bally, *Binding kinetics and lateral mobility of hsv-1 on end-grafted sulfated glycosaminoglycans,* Biophysical Journal **113**, 1223 (2017).

[13] M. Delguste, C. Zeippen, B. Machiels, J. Mast, L. Gillet, and D. Alsteens, *Multivalent binding of herpesvirus to living cells is tightly regulated during infection,* Science Advances **4** (2018).

[14] C. Sieben, E. Sezgin, C. Eggeling, and S. Manley, *Influenza a viruses use multivalent sialic acid clusters for cell binding and receptor activation,* PLOS Pathogens **16**, e1008656 (2020).

[15] M. BM, C. P, and D. M. L, *Programmable interactions with biomimetic dna linkers at fluid membranes and interfaces,* Reports on progress in physics. Physical Society (Great Britain) **82** (2019).

[16] R. Lanfranco, P. K. Jana, L. Tunesi, P. Cicuta, B. M. Mognetti, L. D. Michele, and G. Bruylants, *Kinetics of nanoparticle–membrane adhesion mediated by multivalent interactions,* Langmuir **35**, 2002 (2019).

[17] D. D. Iorio, Y. Lu, J. Meulman, and J. Huskens, *Recruitment of receptors at supported lipid bilayers promoted by the multivalent binding of ligand-modified unilamellar vesicles,* Chemical Science **11**, 3307 (2020).

[18] S. Merminod, J. R. Edison, H. Fang, M. F. Hagan, and W. B. Rogers, *Avidity and surface mobility in multivalent ligand-receptor binding,* **13**, 12602 (2021).

[19] S. Block, V. P. Zhdanov, and F. Höök, *Quantification of multivalent interactions by tracking single biological nanoparticle mobility on a lipid membrane,* (2016).

[20] I. Chakraborty, V. Meester, C. van der Wel, and D. J. Kraft, *Colloidal joints with designed motion range and tunable joint flexibility,* Nanoscale **9**, 7814 (2017).

[21] A. McMullen, S. Hilgenfeldt, and J. Brujic, *Dna self-organization controls valence in programmable colloid design,* Proceedings of the National Academy of Sciences **118** (2021).

[22] S. F. Fenz, A.-S. Smith, R. Merkel, and K. Sengupta, *Inter-membrane adhesion mediated by mobile linkers: Effect of receptor shortage,* Soft Matter **7**, 952 (2011).

[23] S. Shimobayashi, B. Mognetti, L. Parolini, D. Orsi, P. Cicuta, and L. D. Michele, *Direct measurement of dna-mediated adhesion between lipid bilayers,* Physical chemistry chemical physics : PCCP **17**, 15615 (2015).

[24] C. Linne, D. Visco, S. Angioletti-Uberti, L. Laan, and D. J. Kraft, *Direct visualization of superselective colloid-surface binding mediated by multivalent interactions,* Proceedings of the National Academy of Sciences **118** (2021).

[25] Y. Zhang, Q. Li, M. Dong, and X. Han, *Effect of cholesterol on the fluidity of supported lipid bilayers,* Colloids and Surfaces B: Biointerfaces **196**, 111353 (2020).

[26] S. Chakraborty, M. Doktorova, T. R. Molugu, F. A. Heberle, H. L. Scott, B. Dzikovski, M. Nagao, L. R. Stingaciu, R. F. Standaert, F. N. Barrera, J. Katsaras, G. Khelashvili, M. F. Brown, and R. Ashkar, *How cholesterol stiffens unsaturated lipid membranes,*

Proceedings of the National Academy of Sciences of the United States of America **117**, 21896 (2020).

[27] P. Delcanale, B. Miret-Ontiveros, M. Arista-Romero, S. Pujals, and L. Albertazzi, *Nanoscale mapping functional sites on nanoparticles by points accumulation for imaging in nanoscale topography (paint),* ACS Nano **12**, 7629 (2018).

[28] M. Liu, A. Apriceno, M. Sipin, G. Battaglia, and S. Angioletti-Uberti, *A game of entropy : range selective binding in multivalent constructs,* Nature Communications **11**, 1 (2020).

[29] F. J. Martinez-Veracoechea and M. E. Leunissen, *The entropic impact of tethering, multivalency and dynamic recruitment in systems with specific binding groups,* Soft Matter **9**, 3213 (2013).

[30] M. Rinaldin, R. W. Verweij, I. Chakraborty, and D. J. Kraft, *Colloid supported lipid bilayers for self-assembly,* Soft Matter **15**, 1345 (2019).

[31] J. C. Crocker and D. G. Grier, *Methods of digital video microscopy for colloidal studies,* Journal of Colloid and Interface Science **179**, 298 (1996).

[32] S. V. D. Walt, J. L. Schönberger, J. Nunez-Iglesias, F. Boulogne, J. D. Warner, N. Yager, E. Gouillart, and T. Yu, *Scikit-image: Image processing in python,* PeerJ **2014**, e453 (2014).

4

SUPERSELECTIVE DNA NANOSTAR ADSORPTION

Weak multivalent interactions govern biological processes like cell-cell adhesion and virus-host interactions. These systems distinguish sharply between surfaces based on receptor density, known as superselectivity. Earlier experimental and theoretical work provided insights into the control of selectivity: Weak interactions and a high number of ligands facilitate superselectivity. But present experimental systems typically involve tenth or hundreds of interactions, resulting in a high entropic contribution leading to high selectivities. An experimental system with a high level of control over a few ligands mimicking multidomain proteins and virus binding to a membrane is still missing. Here, we introduce a multivalent experimental model system based on star shaped branched DNA nanostructures with each branch featuring a single stranded overhang that binds to complementary receptors on a target surface. Each DNA nanostar possesses a fluorophore, which allows for the direct visualization of nanostar surface adsorption by total internal reflection microscopy (TIRF). We observe that the weaker the interaction, the more superselective and, surprisingly, stronger the nanostar is bound to the surface. These findings cast a new light on the definition of the strength of multivalent bonds. Our results add to the understanding of multivalent interactions on the nanoscale, which improve future work on selective targeting in directed drug delivery.

4.1. INTRODUCTION

Two entities in biological systems mostly interact weakly and reversibly [1, 2]. Multiple ligands and receptors generate these interactions and form an overall strong bond. These multivalent interactions can promote binding close to existing bonds (cooperativity), increasing the specificity of the system [3]. Multivalent systems are highly relevant in biology, where many processes require a high specificity of binding: intrinsically disordered protein-protein interactions [4], multivalent protein phase separation [5], ubiquitylation [6] and antibody-antigen binding [7]. These examples highlight that multivalent interactions establish a strong bond, although the individual interactions are weak and highly reversible. This combination of high binding probability and strong binding also occurs in virus-host interactions: Multivalent weak interactions significantly increase selectivity, and nevertheless upon binding the virus still diffuses on the cell surface to search for suitable entries for endocytosis [8]. This lateral diffusion of the virus indicates that the overall bond is strong and not immediately reversible [8–10], see Fig. 4.1a.

To understand how biological systems achieve a high selectivity upon binding, Martinez-Veracoechea and Frenkel for the first time introduced the concept of superselectivity as a non-linear increase in the binding probability [11]. In their models a multivalent particle distinguishes surfaces based on receptor density. A change in the interaction strength, valency and/or particle concentration manipulates the sharpness of this transition, where high valency, weak interactions and low particle concentrations yield the highest selectivity. In addition, recent studies illustrated that parameters like crowding [12] or the addition of an external force on the particle [13] also regulate selectivity.

To experimentally assess superselectivity precise control of valency, ligand and receptor interaction strength and the particle's concentration is needed. Present experimental model systems that successfully demonstrated multivalent surface binding include polymers [14, 15], viruses [16] and nano- [17] and microparticles [18, 19]. These studies emphasized that the right interplay of enthalpy and entropy leads to superselectivity. But, experimental model systems consisting of polymers and nanoparticles mimic biological systems that include tenth or hundreds of interactions. Virus particles interact with less than 10 receptors [20], but the experimental control over interaction strength and valency is limited. As far as we know, research on superselectivity with a focus on valencies below ten has not been done. Investigating superselectivity with few binding sites provides insights in the transition from monovalent to multivalent binding.

To adress superselectivity with low valencies, we report a new experimental model system consisting of DNA nanostars. A DNA nanostar consists of branched junctions of DNA strands (also called arms) with single stranded sticky overhangs that act as binding sites (ligands) [21–23]. The sticky ends on each nanostar bind to surface mobile complementary DNA strands (receptors), see Fig. 4.1 b. DNA nanostars have a number of attractive features: the length of the sticky end regulates the interaction strength, the number of arms precisely dictates the valency and a fluorophore attached to one arm allows for the visualization of nanostar-surface adsorption with Total internal reflection fluorescence microscopy (TIRFM).

In this research we want to dissect the role of valency, with few interactions ranging between $2-10$, on superselectivity. More specifically, we want to investigate how the in-

teraction strength in combination with valency regulates selectivity. We aim at connecting individual ligand-receptor binding to nanostar binding by asking how many bonds form in a multivalent interaction and what defines the strength of the overall multivalent bond. We next address how the presence of additional, non-interacting biomolecules, as are typically diffusing in a cell membrane, influence adsorption and superselectivity. Using a combination of theory and experiments we determine the binding kinetics and average number of bonds in the context of nanostar-receptor interactions. We find for a 6 arm nanostar that the weaker the ligand-receptor interaction is, the more superselective it is and surprisingly, the stronger the nanostar is bound to the surface. Our findings offer important insights into the question of how a weakly binding superselective particle can still form a strong bond. Our results advance the understanding of virus-host interactions, where few weak interactions govern superselective cell targeting without immediate detachment of virus particles after binding.

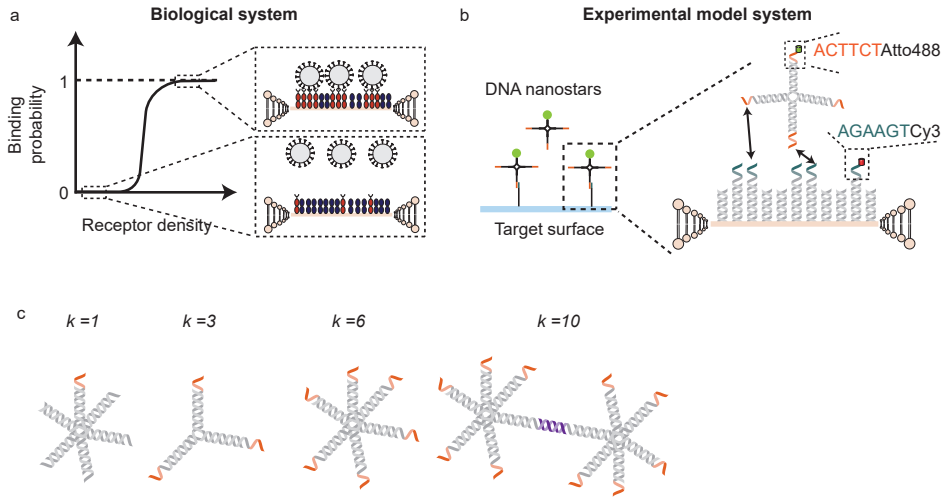

Figure 4.1: **Motivation and model system.** A characteristic feature of superselective systems is a sharp, nonlinear transition in the binding probability with increasing receptor density. This feature occurs in many biological systems, when weak multivalent interactions are involved. a) One example is selectivity in virus-cell adhesion, where only few interaction sites participate in binding. b) We experimentally investigate superselectivity with valencies below 10 with DNA nanostars that feature tunable, well-controlled DNA-DNA interactions and valency. Each arm of the DNA nanostar features a single stranded overhang (sticky end) that binds to the complementary sticky end on the receptors in the supported lipid bilayer (SLB). The length of the sticky end defines the strength of the interaction. Each DNA nanostar and receptor possess a fluorophore, such as Atto488 or Cy3, which allows for the direct visualisation of adsorbed nanostars onto the target surface and receptors. c) DNA nanostar constructs for valencies $k = 1, 3, 6, 10$. Each DNA nanostar holds an Atto488 dye, which is not visible in the sketch.

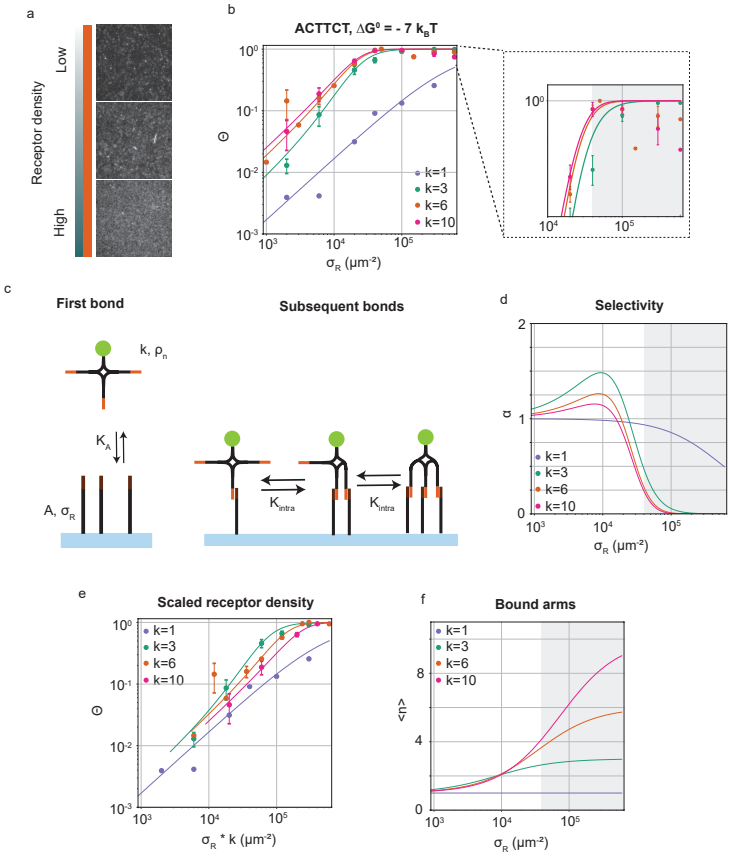

Figure 4.2: **DNA nanostar surface adsorption.** a) To quantify the change in the number of adsorbed nanostars on the target surface, we measure the intensity on the surface. By varying the number of receptors on the surface, we obtain a higher signal with increasing receptor density. After background subtraction and normalisation with the saturated value, we translate the signal into a bound fraction Θ, see Materials and Methods for details. b) The bound fraction Θ measured as a function of receptor density σ_R for sticky end ACTTCT and four valencies $k = 1, 3, 6, 10$. Solid lines are least-squared fits of the model Eq. 4.2 adapted from Frenkel and coworkers [11] with fitting parameters K_A and K_{intra}. For $k = 3$ we excluded the last four datapoints for the fit to get the most accurate mathematical description of the non-linear transition of Θ. A zoom of Θ at high σ_R visualises the deviation of the model from the datapoints. Interestingly, for $k = 6, 10$ we observe a significant decrease of Θ after reaching the maximum adsorption. We indicate the receptor density range, where the model does not capture the data well with a grey area, also for subsequent analysis throughout this chapter. c) The adsorption of a nanostar is a two step process: First, the first bond forms and then, subsequent bonds follow. This sketch points out relevant parameters of the system used for the model Eq. 4.2. d) Together with the mathematical description of Θ in a), we compute the selectivity parameter $\alpha = \frac{d\ln\Theta}{d\ln\sigma_R}$. e) Rescaled x-axis of a) with the valency k. f) Eq. 4.9 and Θ obtained from the least squared fit in a) yield the average number of bound arms $\langle n \rangle$.

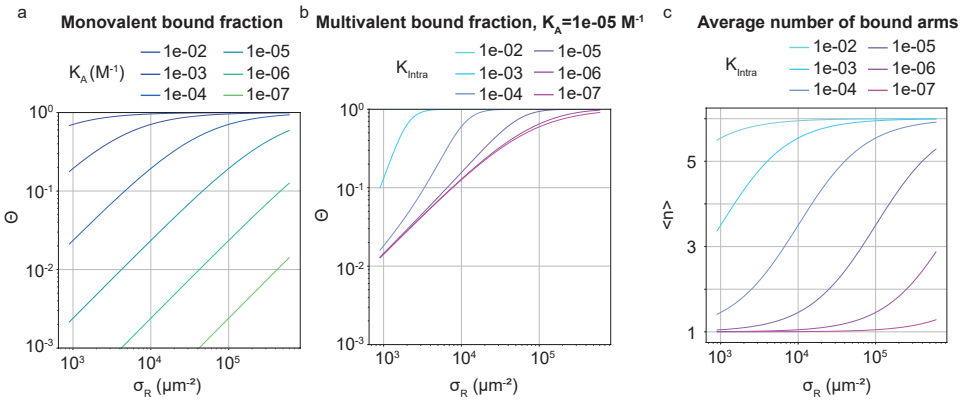

Figure 4.3: **Model for $k = 6$ and different K_A and K_{intra}.** a) Theoretical prediction of Θ for a monovalent particle for different K_A, see Eq. 4.1.b) Eq. 4.2 predicts Θ for fixed $K_A = 1e-05\ M^{-1}$ and varying K_{intra}. c) Average number of bound arms $\langle n \rangle$ for varying K_{intra}, see Eq. 4.9.

4.2. RESULTS

4.2.1. SUPERSELECTIVE DNA NANOSTAR ADSORPTION

In this section, we show our experimental results of DNA nanostar surface adsorption. We systematically study superselective surface targeting using DNA nanostars with a ss-DNA sequence at the end of each arm (sticky end) that binds to receptors on a target surface with the complementary sticky end, see Fig. 4.1b. The receptors consist of a 77 bp double stranded stem with a cholesterol molecule on the 5′ end. Cholesterol integrates the receptor into a supported lipid bilayer (SLB) on the target surface and ensures full mobility of the receptors [24–26]. On the 3′ end the receptors have a sticky end with the complementary sequence to the nanostar sticky ends. The length of the sticky end determines the hybridization free energy of each arm, see Materials and Methods for details. Each DNA nanostar possesses an Atto488 dye on the 3′ end of one arm, which does not inhibit binding. The excitation of the fluorophore and acquisition of the emission with total internal reflection microscopy (TIRFM) allows for the direct visualization of nanostar-surface adsorption. The advantage of TIRFM is the direct excitation of the nanostars on the surface and limiting the excitation of nanostars in solution.

First we ask how the number of adsorbed nanostars changes with a change in the receptor density σ_R for a fixed interaction strength. We therefore imaged the nanostar signal for different receptor densities ranging from low to high, see Fig. 4.2a. An increase in σ_R clearly enhances the fluorescent signal emitted from the SLB, implying increased adsorption of the nanostars. This result demonstrates that the number of adsorbed nanostars to the surface changes with σ_R. For these experiments, nanostars with valencies 1, 3, 6 and 10 were used.

To quantitatively elucidate the transition of nanostar adsorption, we employed nanostars with different number of arms k, and imaged their adsorption to SLBs functionalized with different receptor concentrations σ_R. We measured the mean intensity of a certain area, and normalised it with respect to the maximum intensity of the same area. Finally,

we plot the normalised signal, here referred to as binding probability Θ as a function of σ_R, see Fig. 4.2b.

We started by investigating the nanostar-surface adsorption for different number of arms $k = 1, 3, 4, 10$ but with fixed hybridization energy $\Delta G^0 = -7\ k_BT$ at a constant nanostar concentration in solution $\rho_n = 10^{-8}$ M. We choose this interaction strength based on our findings in a previous study with colloidal particles [18], where superselective binding occurred for ligand-receptor interaction enthalpies around $\Delta G^0 = -7\ k_BT$. We measured Θ over receptor densities ranging between $\sigma_R = (1.000 - 600.000)\ \mu m^{-2}$, see Fig. 4.2b, and found that Θ smoothly increases with increasing σ_R. With smaller valency k the curve shifts to higher σ_R. This can be understood from the decrease in the enthalpy and therefore causing a shift along σ_R, which we will explain in more detail later in this section. Interestingly, for $k = 6, 10$, Θ decreases again at high σ_R after reaching $\Theta = 1$, see Fig. 4.2b zoom. There are two possible explanations for this observation. First, the receptors induce a steric repulsion that increases the energy barrier for nanostars to adsorb at high σ_R [27]. Second, the receptors are not available for binding because divalent ions cause DNA bridging, which becomes more dominant with increasing σ_R [28–30]. Further studies targeting the role of steric repulsion and divalent ions need to be undertaken to pinpoint the origin of the decrease in Θ at large σ_R. Overall, our results confirm that the valency and σ_R are important for the adsorption of multivalent particles.

To get an analytical description of the experimental data, we adapt the model developed by Frenkel and coworkers [11, 31]. The Langmuir isotherm describes the adsorption of a monovalent nanostar Θ_{mono}:

$$\Theta = \frac{\rho_n A \sigma_R K_A}{1 + \rho_n A \sigma_R K_A}, \tag{4.1}$$

where ρ_n is the nanostar concentration in solution, σ_R is the receptor density on the target surface, A is the total surface area and K_A is the equilibrium association constant to form a single bond. The interaction strength of the ligand and receptor shifts Θ relative to σ_R, see Fig. 4.3a. The number of arms $k > 1$ introduces a combinatorial term to the system that accounts for the number of possible bond formations, see Fig. 4.2c. Hence, the adsorption now depends on K_A^{av}, the equilibrium avidity association constant:

$$\Theta = \frac{\rho_n K_A^{av}(K_A, K_{intra}, k)}{1 + \rho_n K_A^{av}(K_A, K_{intra}, k)}, \tag{4.2}$$

where K_{intra} is the equilibrium constant for subsequent bonds, after the first bond is established. In sum, K_A^{av} accounts for the formation of the first bond and, additionally, includes a combinatorial term that describes the formation of subsequent bonds:

$$K_A^{av} \approx \frac{K_A}{K_{intra}} \left[(1 + \sigma_R A K_{intra})^k - 1 \right]. \tag{4.3}$$

Depending on the value of K_{intra}, Θ of a multivalent particle with $k = 6$ yields a linear or non-linear transition of Θ, see Fig. 4.3b. For small K_{intra} the multivalent particle binds monovalently, whereas an increase in K_{intra} leads to sharper non-linear transitions. Hence, the superselectivity of a system depends on the likelihood of forming subsequent bonds. Overall, this observation highlights the need for an analytical expression of the average number of bound arms.

In the following section we apply the theory to our experimental data to extract information about the chemical equilibrium constants K_A and K_{intra}. A least-square fit with Eq. 4.2 to the experimental data in Fig. 4.2b yields the fitting parameters K_A/K_{intra}, $1/K_{intra}$ and a division of the two values yields K_A. The fit with Eq. 4.2 captures the experimental data over a wide range of σ_R, see Fig. 4.2b. At large σ_R, however, the model deviates significantly from the data. This finding further supports the idea of additional aspecific or repulsive interactions at high σ_R, because the model does not account for these parameters. Because of this potential limitation at large σ_R, we highlight this receptor density range with a grey area. Furthermore, the model does not accurately capture the non-linear transition in Θ for $k = 3$ because of the slow saturation at high σ_R. Regarding the limitation of the model, we only fit the first four datapoints for $k = 3$. The fitting results are reported in Tab. 4.1a.

Table 4.1: **Fitparameter.** A fit with Eq. 4.2 to Θ in Fig. 4.2a yields the fitting parameters K_A/K_{intra} and K_{intra}. The numbers in brackets indicate the fitting error. A division of the two fitting parameters yields K_A.

k	$K_A/K_{intra}(M^{-1} * 10^6)$	$K_{intra}(*10^{-12})$	$K_A(M^{-1} * 10^{-5})$
1	-	-	0.5(0.1)
3	2.3(0.5)	5(0.1)	1.2
6	10.1(0.2)	1.2(0.6)	1.2
10	17.9(0.2)	0.6(0.3)	1.0

Interestingly, a comparison of K_A for $k = 1,3,6,10$ in Tab. 4.1 reveals no significant difference, consistent with theory. The first bond formation therefore only depends on ρ_n and the number of free receptors and not on the valency of the nanostars. If the bonds are formed independently of each other, the binding probability of the multivalent particle would scale with the valency k:

$$\Theta_{multi} = k * \Theta_{mono}. \tag{4.4}$$

To test whether this relation holds for our experimental system, we multiply σ_R with k, see Fig. 4.2e. From this plot we find that the multivalent binding curves shift towards the monovalent curve and fall on top of each other in the low σ_R range. In this range, nanostars most likely bind one arm only and thus effectively bind monovalently. However, at increasing σ_R the curves starts to deviate from each other underlining that a mathematical description of the non-linear transition must include combinatorial effects.

Subsequent bond formations are captured by the second fitting parameter $1/K_{intra}$. Interestingly, we observe an increase in K_{intra} with decreasing k. This means that nanostars with more arms are less likely to bind with multiple arms to the SLB. This rather contradictory result may be due to the different geometries of DNA nanostars, see Fig. 4.1c. We hypothesize that the decrease in K_{intra} stems from a change in flexibility of the arms with increasing k. A nanostar with less arms has larger opening angles and more space to explore compared to higher valencies. Furthermore, the larger k, the more bonds can form, and hence, the further the arms need to bend towards the receptors on the substrate. The geometry of the nanostar is thus an important aspect for future research.

Together our results provide insights into the equilibrium constants of binding. The next paragraph evaluates how selectivity and chemical rate constants are related.
The selectivity α of a multivalent system describes the transition of Θ from unbound to bound [11]:

$$\alpha = \frac{\mathrm{d}\ln\Theta}{\mathrm{d}\ln\sigma_\mathrm{R}}. \tag{4.5}$$

Visually, α describes the slope of Θ as a function of σ_R on a log-log scale and $\alpha > 1$ defines a superselective system. Fig. 4.2d presents α for Θ in Fig. 4.2b. The selectivity of a monovalent nanostar never exceeds 1. This agrees with theory because a monovalent particle follows the Langmuir adsorption, which has a maximum slope of 1, see Fig. 4.3a. An increase in k is expected to lead to an increase in α, see Fig. 4.2d. Surprisingly, we observe the highest selectivity for $k = 3$ which is not according to theory which predicts that an increase in k always leads to an increase in selectivity.

To investigate the relation between selectivity and binding constants, we compare the maximum α (Fig. 4.2d) with the values found for K_intra (Tab. 4.1). From the data we see a clear connection between the two parameters: the larger K_intra, the larger α. This observation implies that a multivalent particle becomes more superselective, if it binds more quickly with subsequent arms and thus is more likely to bind with the maximum number of bonds after establishing the first bond. These results highlight the importance of subsequent bond formation in a superselective system. In the following, we therefore investigate how the average number of bound arms scales with σ_R.

To investigate the average number of bound arms $\langle n\rangle$ and how it correlates with the selectivity, we derive an analytical expression for the average number of bound arms. Given that the nanostar has established the first bond, we derive an equation for the average number of bound arms [32]:

$$\langle n\rangle = 1 + \frac{\partial}{\partial\mu}\beta \ln Z_1, \tag{4.6}$$

where $\beta = \mathrm{k_B T}$ and Z_1 describes the state partition function of a single bound nanostar with one arm. The binding free energy f for subsequent bonds and the chemical potential μ generate Z_1:

$$Z_1 = \sum_{n=0}^{k-1} \binom{k-1}{n} \exp^{-\beta n f} \exp^{\beta n \mu} = (\exp^{-\beta(f-\mu)} + 1)^{k-1}. \tag{4.7}$$

Together with Eq. 4.6, the expression for $\langle n\rangle$ yields:

$$\langle n\rangle = 1 + \frac{k-1}{1 + (\frac{\sigma_\mathrm{R}}{\sigma_0}\exp^{\beta f})^{-1}}. \tag{4.8}$$

In chapter 2, we derived a similar expression and a comparison yields $\frac{\sigma_\mathrm{R}}{\sigma_0} = \sigma_\mathrm{R} A$. Furthermore [31] defines $\exp^{\beta f} = K_\mathrm{intra}$. Together, this provides an expression for the average number of bound arms:

$$\langle n\rangle = 1 + \frac{k-1}{1 + (\sigma_\mathrm{R} A K_\mathrm{intra})^{-1}}. \tag{4.9}$$

This equation describes the number of bonds, given that at least one arm is bound and therefore it only depends on K_{intra}. Comparing $\langle n \rangle$ for different values of K_{intra} we notice that the larger K_{intra}, the sooner the increase of $\langle n \rangle$ with increasing σ_R, see Fig. 4.3c. In the previous section, we measured K_{intra} and together with Eq. 4.9 we evaluate $\langle n \rangle$ for different k and σ_{R}, see Fig. 4.2f. Note, in the grey area we expect the largest uncertainty for K_{intra}, which is why we do not take those results into account. The monovalent nanostar never exceeds $\langle n \rangle = 1$, which is expected because it can only form one bond due to the design. For $k > 1$, $\langle n \rangle$ increases and within the receptor range that we can trust the model, $k = 3$ approximately reaches the maximum number of bonds possible. The σ_{R} at which $k = 3$ reaches the maximum number of bonds agrees with the σ_{R} at which we observe the non-linear transition in Θ. Although $k = 6$ and $k = 10$ reach saturation around $\sigma_{\text{R}} \approx 4 * 10^4$ μm^{-2}, they do not bind with all of their arms. A possible explanation is that an additional parameter dependent on the nanostar's geometry hinders the nanostars from reaching the maximum bonds. Thus, we conclude that the rate of subsequent bonds, described by K_{intra}, regulates the superselectivity of a system. A common approach to increase the selectivity is a decrease in interaction strength. This approach leads to a decrease in K_{A} but the effect on K_{intra} is unknown, which we will investigate in the following section.

4.2.2. TUNING SELECTIVITY WITH ENTHALPY

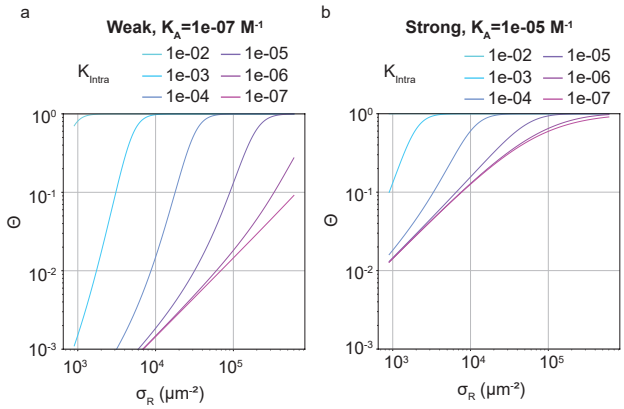

Figure 4.4: **Predicting Θ for strong and weak binding.** Comparing the adsorption curves for DNA nanostars with the same geometry ($k = 6$) for weak (a) and strong (b) binding for increasing K_{intra}.

This section describes and discusses the impact of interaction strength on superselectivity and the underlying binding constants. Theory predicts that the weaker a monovalent particle is the further the binding curve Θ shifts to larger σ_{R}, see Fig. 4.3a. The weaker the individual bonds of a multivalent particle are, the larger the shift of Θ to larger σ_{R} and the larger the σ_{R} range, where $\Theta = 0$ facilitates a non-linear transition by large K_{intra}, see Fig. 4.4a and Fig. 4.4b. Effectively, the formation of subsequent bonds is expected to lead to an increase in α that is stronger the weaker the interactions are.

We test these theoretically predicted scalings in Fig. 4.4a and Fig. 4.4b by measuring

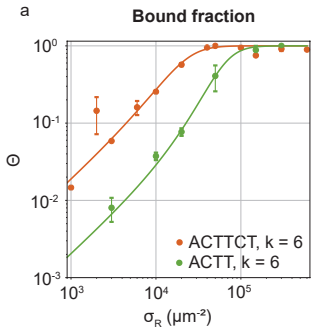

b

Binding constants

sticky end (bp)	k	K_A / K_{Intra} ($M^{-1}*10^6$)	K_{Intra} ($*10^{-12}$)	K_A ($M^{-1}*10^{-5}$)
ACTTCT	6	10.1(0.2)	1.2(0.6)	1.2
ACTT	6	2.1(0.5)	0.7(0.1)	0.1

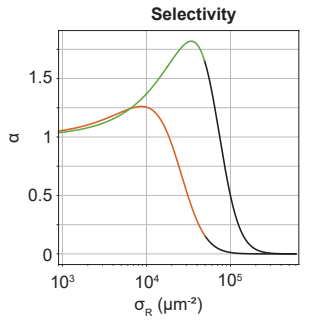

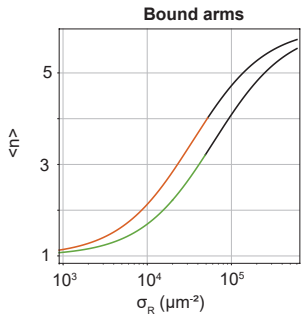

Figure 4.5: **Adsorption of 4 bp and 6 bp sixvalent nanostars.** a) Experimental results for Θ as a function of the receptor density σ_R for a 6 bp ($\Delta G^0 = -7\ k_BT$) and 4 bp ($\Delta G^0 = -4\ k_BT$) sticky end. The dashed lines represent a least-square fit with Eq. 4.2, results of which are reported in the table in (b). Note, that the fit for ACTT, k = 6 has been restricted to the two datapoints that determine the non-linear transition (encircled in red). b) Fitting results for K_A and K_{intra} obtained from fitting Eq. 4.2 to the data presented in (a). The numbers in brackets represent the fitting error. c) The fit from (a) and Eq. 4.5 generates the selectivity α. d) Plot of the average number of bound arms $\langle n \rangle$ as a function of σ_R obtained from Eq. 4.9. The datapoints displaying an errorbar are the standard error of the mean of at least two experimental replicates. The black color in the curves displays the data that is not captured accurately by the Fit in (a), and hence, excluded from the discussion.

Θ for nanostars with valency $k = 6$ and adhesion strength of the individual arms of $\Delta G^0 = -5\ k_BT$ and compare the results to a DNA nanostar with equal valency $k = 6$ but stronger adhesion $\Delta G^0 = -7\ k_BT$. The data Θ as a function of σ_R for these nanostars with two different sticky ends is presented in Fig. 4.5. Comparing the two results, we immediately notice that Θ_{ACTT} shifts to higher σ_R compared to Θ_{ACTTCT}, in line with the theoretical predictions shown in Fig. 4.3a.

To investigate if and how the selectivity and binding constants vary between these two nanostars, we fit Eq. 4.2 with K_A and K_{intra} as fitting parameters as described in the previous Sec. 4.2.1, see Fig. 4.5a. We note that only the first four data points of the 4 bp sticky end were used in the fit to capture the non-linear transition as accurately as possible, because it determines the maximum selectivity of the system. The fitting results are reported in Fig. 4.5b. Comparing the equilibrium constants of $k = 6$ for the 4 bp and 6 bp sticky end, we notice that whereas the equilibrium constant for binding the first arm, K_A, shows a difference of one order of magnitude, the values for the equilibrium constant associated to binding subsequent arms, K_{intra}, are very similar for the two different sticky end lengths. These results agree with the predictions that a change in enthalpy reduces K_A only, explaining the shifts of Θ along σ_R. Interestingly, changing the enthalpy has nearly no impact on K_{intra}. Previously, we hypothesized that a decrease of K_{intra} might stem from a change in the geometry of the nanostar. Here, the two nanostars have the same structure, and indeed we found similar values for K_{intra}, supporting our hypothesis that the geometry of the multivalent particle has the strongest influence on K_{intra} in our system.

Previously, we assumed that a large K_{intra} facilitates subsequent bond formations and leads to higher selectivity. To test our hypothesis, we calculate α with Eq. 4.5 and plot it in Fig. 4.5c. The selectivity of the nanostars with the 4 bp sticky end is larger compared to those featuring a 6 bp sticky end, although the values of K_{intra} are very similar. This implies that K_{intra} is not playing a dominating role in determining the selectivity, α.

Further comparison of the fitting parameters K_A and K_{intra} for the 4 bp sticky end nanostars shows a large difference in their values. This difference is less pronounced for the 6bp sticky end nanostars. Considering the selectivity differences shown in Fig. 4.5c, this finding suggests that a small K_A and large K_{intra} favors selectivity.

To assess the effect of the binding constants on $\langle n \rangle$, we compute $\langle n \rangle$ for both sticky ends and over the range of σ_R using the obtained values for K_A and K_{intra} and Eq. 4.9. Fig. 4.5d illustrates a similar increase in $\langle n \rangle$ with increasing σ_R for both sticky ends. The only difference is the small shift relative to σ_R as we also observed in Fig. 4.5a. However, the slope is similar for both sticky ends. This finding is expected because $\langle n \rangle$ only depends on K_{intra}, which does not differ between the two sticky ends.

This section has analysed the impact of weaker interactions on the selectivity and binding constants, while keeping the same k and thus same geometry of the nanostar. The findings raise the question how we can experimentally achieve a large difference between K_A and K_{intra}. One way to achieve an even further decrease in K_A is by shortening the sticky end further. Alternatively, other methods that reduce the binding of the first arm to the surface might work as well. In the following, we will test the latter by introducing inert DNA strands on the target surface as a steric hindrance for nanostar adsorption and measure the equilibrium constants.

4.2.3. TUNING THE EQUILIBRIUM CONSTANTS WITH INERT STRANDS

In cell membranes many more molecules besides the targeted receptors are present that may on the one hand weakly interact with any approaching particle or on the other hand induce a steric repulsion that prevents the particle from binding. Here, we mimic this effect by introducing inert strands to the experimental system to test if and how steric repulsions affect superselective binding. The term inert is commonly used for molecules that do not have any function in the system. In colloidal systems, steric stabilization against aggregation by for example adsorbed or grafted polymers is well-established. More recently, inert, non-interacting DNA strands have been found to provide a similar stabilization against unspecific attractions [25, 33], see Fig. 4.6a.

We here use inert strands that consist of 47 bp dsDNA anchored via a cholesterol molecule into the SLB. Note, that the inert strands are around 30 bp shorter compared to the receptors, leaving the sticky end of the DNA receptors accessible to the nanostars. For all the measurements, we keep the total amount of DNA strands (inert DNA + receptors) at 300.000 μm^{-2} constant and only adjusted the ratios between inert strands and receptors. In this way, membrane properties remain unaffected through a constant cholesterol concentration.

To investigate whether the presence of inert strands changes the binding constants of nanostar adsorption, we start by measuring the binding behavior for nanostars equipped with 6 bp sticky ends and valencies $k = 1, 6$ and 4 bp sticky ends and valency $k = 6$ to target surfaces functionalized with both inert strands and receptors, see Fig. 4.6b. For all nanostars, the data shows a smooth transition from unbound to bound. Surprisingly, we find an initial plateau at low σ_R for all sticky ends, see Fig. 4.6b. These findings can be attributed to the inert strands, because no such plateau was found for in their absence, see Sec.4.2.1. We speculate that the origin for the plateau can be found in multivalent electrostatic effects as follows: the addition of DNA molecules to the target surface might increase the overall negative charge, which attracts divalent magnesium ions present in the buffer. Their divalent charge in turn could attract the negatively charged nanostars, an effect known as magnesium ion bridging [30]. Hence, the inert DNA strands possibly introduce an electrostatic, non-specific attraction for the nanostars, leading to their adsorption to the SLB already at low receptor concentrations.

After the initial plateau, the monovalent nanostar shows a linear increase, whereas the adsorption of 6-valent nanostars grows non-linearly. We again fit Eq. 4.2 to the experimental data. However, the theoretical model does not capture the initial plateau at low σ_R because it does not account for an additional binding mode. Here, we suspect that the weak binding between nanostars and inert strands generate a second binding mode and hence the initial datapoints that form a plateau are not included in the fit. We therefore only use the two datapoints that define the non-linear transition (encircled in red), see Fig. 4.6b, while still excluding data at high receptor density as we did before.

The resulting selectivity α shows that the monovalent nanostars never exceed $\alpha = 1$ as expected, whereas $\alpha \approx 2.5$ for both the nanostars with ACTT and ACTTCT, see Fig. 4.6c. Comparing the two systems with and without inert strands (see Fig. 4.5 and Fig. 4.6), we note two differences for $k = 6$: 1) α significantly increases after adding inert strands, and 2) Θ shifts to larger σ_R. The monovalent nanostars behave similarly in both systems, except for the appearance of the initial plateau. A shift of Θ to higher σ_R generally indi-

cates a change in K_A. If we now turn to the binding constants reported in Fig. 4.6d we indeed find that K_A decreased by one order of magnitude. Why did K_A not change for the monovalent nanostar? We suspect that the reason is that the monovalent already binds at relatively high σ_R (see Fig. 4.2a). At larger σ_R, fewer inert strands are present when the overall DNA strand concentration is kept constant and hence the magnesium adsorption and thus any contributions from non-specific nanostar adsorption are similar in both systems. However, these data must be interpreted with caution because the underlying theoretical model does not include the secondary binding mode through electrostatic adsorption. An extension of the model with a second binding mode is required before a confident interpretation can be done.

We find that the difference between K_A and K_{intra} for both sticky ends is even larger compared to previous measurements. The difference in selectivity can only be attributable to the large difference between the binding constants. From the previous discussions, we pointed out that K_{intra} regulates $\langle n \rangle$. Because K_{intra} barely changed, we expect the same $\langle n \rangle$ for the range of σ_R. And indeed, the slope of $\langle n \rangle$ (see Fig. 4.6e) is similar as for the system without inert strand, see Fig. 4.5e. However, caution must be applied because we can only trust $\langle n \rangle$ for a very small range of σ_R. If we assume that the plateau results from magnesium bridging, then $\langle n \rangle = 0$ for σ_R before the non-linear transition. Above a specific σ_R the nanostars bind specifically through their DNA-DNA interactions and they rapidly transition to binding with three arms.

This section has discussed the impact of inert strands on the selectivity of nanostar adsorption. We found that the presence of inert strands significantly reduces K_A, whereas it induces little effect on K_{intra}. We hypothesize that the addition of inert strands lead to magnesium ion bridging between the target surface and nanostars. To break the bridges, the system needs to invest energy and effectively weakens the ligand and receptor interactions. However, it remains unclear why the magnesium bridges do not change K_{intra} as it did affect K_A. To explain this observation, we need a full theoretical description of K_{intra} to understand the contribution of enthalpy to K_{intra}. In addition, it is important to experimentally test how $\langle n \rangle$ changes with σ_R and interaction strength. So far, the model yields an approximation of $\langle n \rangle$ for a certain σ_R. The following section will discuss the binding kinetics of bound nanostars to assess the strength of the bonds with respect to sticky end, valency and inert strands.

4.2.4. BINDING KINETICS

Because of their weak multivalent interactions nanostars highly dynamically bind and unbind, leading to a constant exchange between unbound nanostars in solution with adsorbed nanostars on the surface. The higher the number of interactions between nanostar and receptors, the longer it resides on the surface. From the above experiments, we therefore expect that the length and sequence of the sticky end (i.e. its enthalpy) and the valency k dictates the timescale of unbinding and binding. Here, we investigate the binding kinetics quantitatively with fluorescent recovery after photobleaching (FRAP). Data for the 4 bp and 6 bp sticky ends with varying k and for both, with and without inert strands will be compared.

To assess the binding kinetics, we bleach a circular area of nanostars adsorbed on the surface at different σ_R and measure the normalised recovery signal I(5s) 5 s after

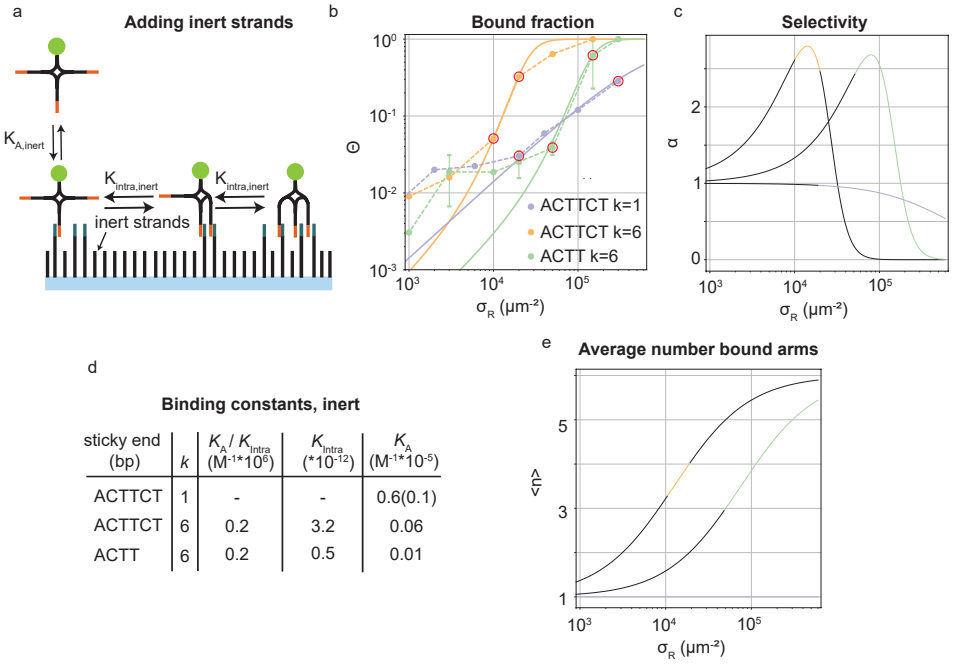

d

Binding constants, inert

sticky end (bp)	k	K_A / K_{Intra} ($M^{-1}*10^6$)	K_{Intra} ($*10^{-12}$)	K_A ($M^{-1}*10^{-5}$)
ACTTCT	1	-	-	0.6(0.1)
ACTTCT	6	0.2	3.2	0.06
ACTT	6	0.2	0.5	0.01

Figure 4.6: **Tuning selectivity with inert strands.** a) Sketch of the experimental system and relevant parameters for binding after introducing inert strands to the target surface. Inert strands are 47 bp dsDNA and they anchor via two cholesterol molecules into the SLB on the surface. Note, that the inert strands are approximately 30 bp shorter compared to receptors with a sticky end. b) Experimental results for Θ as a function of σ_R for 6 bp sticky ends with valencies $k = 1, 6$ and 4 bp sticky end with valency $k = 6$. The full shape of the curves cannot be accurately described with Eq. 4.2, which is why we fit only the two datapoints that define the non-linear transition (encircled in red). The dashed line is a guide to the eye and the solid line results from a fit with Eq. 4.2. c) Selectivity α derived from the fits of Θ with Eq. 4.2. d) Fitting parameters K_A and K_{intra}. e) The average number of bound arms $\langle n \rangle$ as a function of σ_R. Errorbars are the standard error of the mean of at least two replicates.

bleaching, see Fig. 4.7a. This time interval was chosen to exclude a significant contribution from the diffusion of membrane-bound nanostars into the field of view to the signal recovery. In this way, signal recovery should stem solely from desorption of bleached nanostars, and adsorption of unbleached nanostars.

First, we measure $I(5s)$ for the nanostars with 4 bp ($k = 6$) and for the 6 bp ($k = 1,3,6$) sticky ends for the different σ_R, see Fig. 4.7b. All intensities follow a decreasing trend with increasing σ_R, implying that the nanostars stay longer on the surface if there are more receptors present. These findings show that multivalent nanostars bind with more than one arm, because we expect $\langle n \rangle$ to increase with increasing σ_R, see Fig. 4.2d. However, the recovery does not solely depend on the number of arms bound, because also the monovalent recovery signal decreases with increasing σ_R despite only being able to form one bond. This implies the presence of a second adsorption mechanism beyond the specific binding through the complementary DNA sequences which increases in strength with σ_R. This observation provides further proof for our hypothesis of aspecific adsorption through magnesium bridging, which indeed becomes stronger with σ_R.

Surprisingly, the 4 bp sticky end recovers slower compared to the 6 bp sticky end, indicating that the 4 bp nanostars bind more strongly to the surface despite their lower enthalpy of binding. If we assume magnesium bridging as the second binding mode and thus independent of the sticky end, the difference between the 6 bp and 4 bp is most likely a result from a difference in $\langle n \rangle$. As a consequence, to our surprise, at the same receptor density and nanostar concentration the 4 bp seems to bind on average with more arms compared to the 6 bp nanostars.

A system with inert strands caused a decrease in K_A, effectively weakening the bonds and thus facilitating bond breaking. To assess the influence of inert DNA on the binding kinetics, we performed the same measurement for an SLB functionalized with inert strands and receptors and nanostars that possess either a 4 bp ($k = 6$) or 6 bp ($k = 1,6$) sticky end. Fig. 4.7c compares the experimental data of $I(5s)$ for different σ_R. The recovery signals of all nanostars show a decrease with increasing σ_R. The binding behavior of the monovalent nanostars is very similar with and without inert DNA strands.

The 6bp first decreases until it seems to plateau around $\sigma_R = 10^5\ \mu m^{-2}$. A plateau would indicate that a change in σ_R does not change the binding kinetics of the 6 bp nanostar and the maximum number of bonds is reached. However, to verify this plateau, additional measurements at higher σ_R are needed.

Interestingly, the 4 bp ($k = 6$) behaves like the monovalent nanostar at the beginning before a sharp drop at $\sigma_R = 300000 \mu m^{-2}$. This concentration of σ_R coincides with the concentration at which the 4 bp ($k = 6$)nanostar undergoes non-linear superselective binding, see Fig. 4.6b. Surprisingly, the 4 bp nanostars, again, bind even stronger than the 6 bp nanostars in spite of the higher enthalpy for the 6 bp sticky ends. This raises questions about $\langle n \rangle$ in association with $I(5s)$, which we will discuss next.

The interaction strength and valence k of a nanostar regulate the residence time on the target surface. With increasing σ_R we expect an increase in $\langle n \rangle$ (see Eq. 4.9) and therefore a slower recovery. To test whether $\langle n \rangle$ correlates with the recovery $I(5s)$, we plot it as a function of $\langle n \rangle$, see Fig. 4.7d-e. The datapoints in grey fall into the regime at low and high σ_R, where we expect that a second binding mode dominates the interactions

or steric repulsion, which are not included in the model. That is why we exclude them in our discussion. Strikingly, all data seems to fall onto a single curve for small values of $\langle n \rangle$, indicating that indeed binding is directly related to average number of bound arms. However, also the monovalent case shows a decrease in $I(5s)$ at a constant $\langle n \rangle$, suggesting that the 6 bp are mostly in the state of one arm bound. The 4bp nanostars show a slightly lower $I(5s)$ for the same $\langle n \rangle$, suggesting again a stronger binding than the 6 bp. If we turn to the system with inert strands, we again find a similar trend for small $\langle n \rangle$ albeit for very few data points, but then the difference of $I(5s)$ for different σ_{R} between the 4 bp and 6 bp becomes more significant. First, the 4 bp behaves like the monovalent nanostar and at certain σ_{R} the 4 bp decreases steeper compared to the 6 bp, presumably because more arms bind. The 4 bp consistently shows stronger binding to the surface than the 6 bp nanostar. However, due to the limitations in the theoretical model at specific σ_R, we cannot clearly state how many bonds are formed and if the 6 bp and 4 bp form the same number of bonds for $k = 6$ and if so, why the weaker sticky ends bind more strongly. Therefore, it is important to add another method to quantify $\langle n \rangle$.

4.3. CONCLUSION

In this chapter, we have studied superselectivity on the nanoscale, where a few ligand and receptor interactions are enough for superselective adhesion. The experimental setup allowed for the needed high level of control of the number of ligands, their interaction strength and a direct visualisation of multivalent targeting. Combining theory and experiments, we gained insights into the binding constants and the average number of bound arms. Lastly, we have presented the dynamic unbinding and binding of nanostars.

Superselectivity on the molecular level requires a weak first bond and a rapid transition to the maximum number of bonds. For the design of superselective particles, it is therefore highly important to decrease the binding probability of the first bond as much as possible. As a result, the multivalent particle has to bind with as many interactions as possible on a short timescale to achieve an overall strong and stable bond. The stronger the bond the longer the particle resides on the surface. The combination of high superselectivity and long residence time has been observed for biological systems like virus-cell interactions and protein-membrane adhesion. These systems need a high selectivity and after binding lateral diffusion on the target surface.

The most surprising result in this chapter is that multivalent weak interactions bind more strongly at large σ_{R} compared to stronger multivalent interactions. We hypothesize that the differences in K_{A} and K_{intra} regulate the strength of binding, see Fig. 4.8. The larger the gap between K_{A} and K_{intra} (see Fig. 4.8a), the more likely the multivalent particle is in a state of many arms bound, whereas a system with similar K_{A} and K_{intra} dynamically switches between the different binding states (see Fig. 4.8b). If $K_{\mathrm{A}} \gg K_{\mathrm{intra}}$, the multivalent particle forms a strong bond with one interaction and is less likely in a state with many arms bound (see Fig. 4.8c). However, more research on this topic needs to be undertaken before the relation between the binding strength and equilibrium constants are fully understood.

For future work, we propose to extend the theoretical model with a second binding mode to accurately capture the experimental data and to investigate the source of the as-

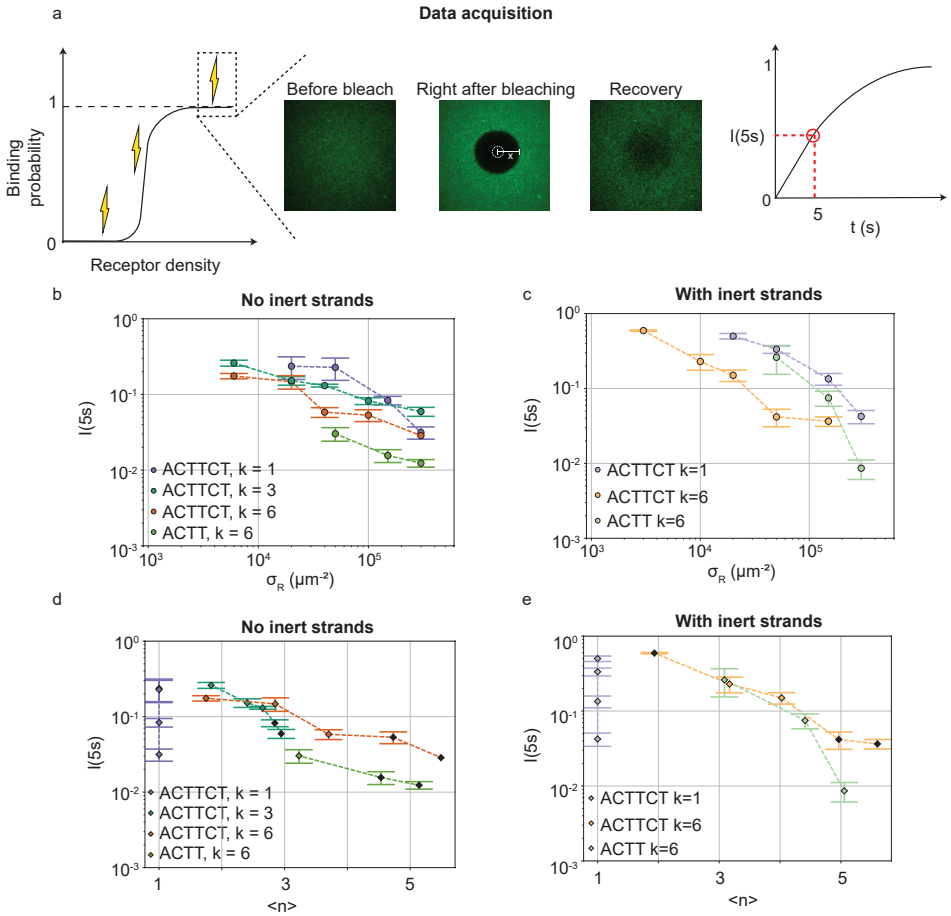

Figure 4.7: **Binding kinetics.** a) Description of the data acquisition of fluorescent recovery after photobleach (FRAP). To exclude the membrane diffusion in the signal recovery, we extracted the signal in the centre of the bleached area and measured the recovered intensity $I(5s)$, after 5 s. b) $I(5s)$ as a function of σ_R for nanostars with 4 bp and 6 bp sticky ends and different valencies k, and an SLB without inert strands, see Fig. 4.2. c) $I(5s)$ for a system with inert strands, see Fig. 4.6. Results include nanostars with 6 bp and 4 bp sticky end and $k = 1, 6$. d,e) $I(5s)$ plotted as a function of $\langle n \rangle$ for an SLB (d) without and (e) with inert DNA strands. The dashed lines are a guide to the eye and the datapoints highlighted in black fall into the specific σ_R range, where we suspect additional binding modes or repulsion, which the theoretical model does not account for.

pecific binding further. To assess the specific rate constants between the different binding states of a nanostar, a complete reaction-diffusion model is needed. Future experimental studies with surface anchored receptors can facilitate the extraction of binding kinetics. Our results provide new insights on the ligand and receptor level in a superselective system and helps the design of drug-delivery systems with a high selectivity and strong overall bond.

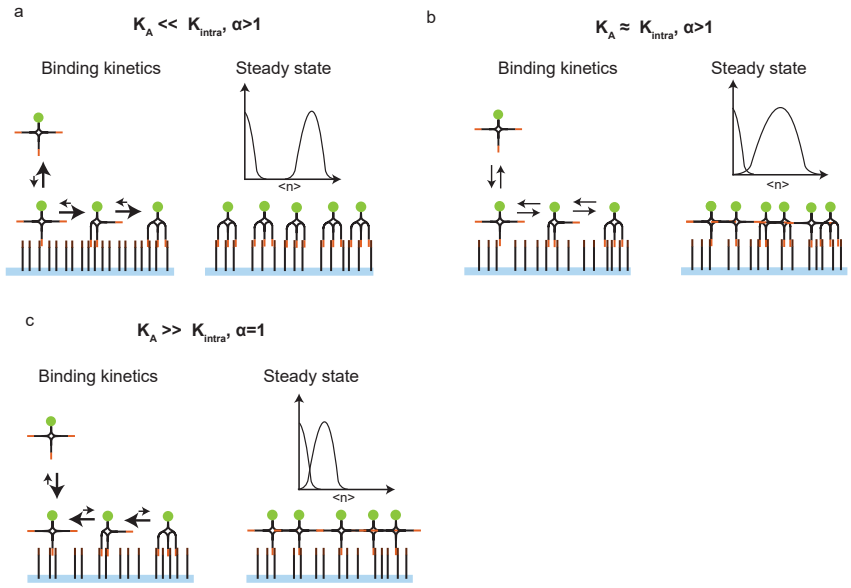

Figure 4.8: **Hypothesis multivalent binding strength.** a) $K_A \ll K_{\text{intra}}$: The individual interactions are very weak and highly reversible. To bind, the receptor density needs to be sufficient such that the particle can immediately bind with multiple arms. Although, the individual interactions are weak and reversible, the particle will be either unbound or on average bound with many arms. These particles will be superselective. b) $K_A \approx K_{\text{intra}}$: The multivalent particle dynamically switches between unbound and every bond state yielding a broad distribution of $\langle n \rangle$. Because the interactions are still reversible and weak, we expect the system to be superselective. c) $K_A \gg K_{\text{intra}}$: If the individual bonds are very strong the formation of one bond is enough to bind the multivalent particle to the surface. In addition, a low probability for subsequent bonds will keep the multivalent particle in a state with few $\langle n \rangle$ or unbound in solutions, similar to a monovalent particle.

4.4. MATERIALS AND METHODS

DNA nanostar hybridisation All DNA strands were purchased from Integrated DNA Technologies Inc (IDT), resuspended in Tris buffer (pH8) and stored at $-20°C$. To achieve for example tetravalent nanostars with four sticky ends and one fluorophore, we mixed the four DNA strands $X1$, $X2$, $X4$ and $X5$ in equal molar ratios and annealed the mixture to $95°C$ for 10 min and then cool it down at a rate of $0.2°C$/min to $4°C$, see Tab. 4.2, Tab. 4.3 and see Fig. 4.9a. The annealing took place in a Thermocycler and a final concentration of 0.5 μM. The final product was stored at $4°C$. For the experiments, we diluted the desired concentration of DNA nanostars and receptors in Tris Acetate-EDTA-NaCl

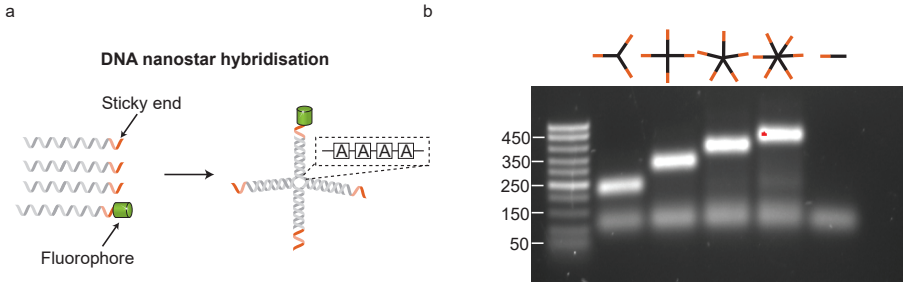

Figure 4.9: **DNA nanostar design.** a) Four ssDNA with a sticky end form the star shaped structure during hybridization. Four free *A* bp at the centre of the nanostar enable full flexibility of the arms. One sticky end possesses an ATTO488 dye for fluorescent imaging. b) DNA electrophoresis allows for the visualization of the final DNA star products after hybridization. The fluorescent bands shift upwards and confirm the formation of larger DNA nanostructures. Each lane contains faint lower bands that represent incompletely hybridized side products.

(TAE,100 mM NaCl, pH=8) and 10 mM magnesium chloride ($MgCl_2$).
To verify the hybridization of the DNA nanostars, we performed DNA electrophoresis. The sample consisted of 10 μL of 0.5 μM nanostars and we loaded the sample on a 1% agarose gel. After 30 min at 100 V we took an image of the gel, see Fig. 4.9b. The fluorescent bands correspond to DNA nanostars: the higher the band, the larger the DNA nanostar nanostructure. Lower bands result from incomplete hybridizations. The intensity of the upper bands is significantly higher, confirming the successful formations of the nanostars.

DNA functionalised supported lipid bilayer We studied the DNA nanostar adsorption in solution in a flow channel. The supported lipid bilayer (SLB) consisted of 18:1 1,2-dioleoyl-sn-glycero-3-phosphocholine (DOPC, [Avanti Polar lipids], stored in chloroform). To obtain the SLB, we first made small unilamellar vesicles (SUVs) from DOPC lipids. To do so, we added the desired volume of lipid to a glass vial and let it dry overnight in a vacuum desiccator. Subsequently, we resuspended the lipids in TAE-NaCl buffer and extruded the solution with an Avanti mini extruder through a membrane with pore size of 30 nm [Avanti Polar lipids]. The microscopy slides and coverslips were sonicated at 30 min each in 2% Hellmanex solution, acetone (> 99.9%) and potassium hydroxide solution (KOH,1 M,[Merck]). Between each change of chemical we rinsed the glass ware [VWR] with milliQ water. Before use, the slides and coverglasses were blown dry with nitrogen. Parafilm stripes confined the flow channel and glued the microscopy slide and a coverslip together. Subsequent annealing at 125°*C* let the Parafilm melt and bound the microscopy slide and coverslip together yielding (1×22)mm rectangular flow channels. To obtain SLBs in the flow channel, we injected SUVs and after 30 min at room temperature, we washed out the excess SUVs with buffer and added DNA of the desired concentration.

Table 4.2: **DNA sequences nanostars.** The DNA strands labelled with *X* form the DNA nanostars. The number of strands and sticky ends define the geometry and valency of the nanostar. To click two DNA nanostars together, the strands X bridge A and X bridge B in combination with the regular nanostar strands X generate a nanostar with valencies larger than 6.

Name	Sequence (5′ to 3′)	5′	3′
X 1	CTACTATGGCGGGTGATAAAAAAA CGGGAAGAGCATGCCCATCCA-*sticky end*	-	ATTO488
X 2	GGATGGGCATGCTCTTCCCGAAAA CTCAACTGCCTGGTGATACGA-*sticky end*	-	-
X 3	CGTATCACCAGGCAGTTGAGAAAA TTTATCACCCGCCATAGTAGA-*sticky end*	-	-
X 4	CGTATCACCAGGCAGTTGAGAAAA CATGCGAGGGTCCAATACCGA-*sticky end*	-	-
X 5	CGGTATTGGACCCTCGCATGAAAA TTTATCACCCGCCATAGTAGA-*sticky end*	-	-
X 6	CGGTATTGGACCCTCGCATGAAAA CCATGCTGGACTCAACTGACA-*sticky end*	-	-
X 7	GTCAGTTGAGTCCAGCATGGAAAA TTTATCACCCGCCATAGTAGA-*sticky end*	-	-
X 8	GTCAGTTGAGTCCAGCATGGAAAA CGCATCAGTTGCGGCGCCGCA-*sticky end*	-	-
X 9	GCGGCGCCGCAACTGATGCGAAAA TTTATCACCCGCCATAGTAGA-*sticky end*	-	-
X *sticky end*	GTAG, GTGATT	-	-
X bridge A	GGATGGGCATGCTCTTCCCGAAAACTCAAC TGCCTGGTGATACGTCCACCAATCCACTAA TCCT	-	-
X bridge B	GGATGGGCATGCTCTTCCCGAAAACTCAAC TGCCTGGTGATACGAGGATTAGTGGATTGGT GGA	-	-

Data acquisition and analysis To image the nanostar adsorption on the target surface we used Total Internal Reflection Microscopy (TIRF) on an inverted fluorescence microscope (Nikon Ti2-E) upgraded with an azimuthal TIRF/FRAP illumination module (Gata systems,iLAS 2) equipped with a 100× oil immersion objective (Nikon Apo TIRF, 1.49NA). Each DNA nanostar possesses an Atto488 dye and each receptor features a Cy3 dye. Therefore, we used laser excitations with wavelength 488 nm and 561nm and detect the emitted fluorescent signal (EM-CCD Andor iXON Ultra 897). For each binding probability we measure for 7 different σ_R the intensity of the nanostars I to obtain the full range of adsorption from unbound to bound. A negative control with $\sigma_R = 0\ \mu m^{-2}$ defines the background signal I_{back}. The maximum intensity I_{max} provides a reference for normalization. The monovalent nanostars were not measured until saturation due to practical constraints. Therefore, we normalized the monovalent signal with the maxi-

Table 4.3: **DNA sequences surface.** Inert strand A and inert strand B are the two components for the dsDNA used as inert strands. The hybridization of receptor backbone and receptor yields the receptor with a sticky end.

Name	Sequence (5′ to 3′)	5′	3′
receptor *sticky end*	CTAC, AATCAC	-	-
Inert strand A	CGTAAGGCAGGGCTCTCT AGATTGACTGTGCGAAGG GTAGCGATTTT	-	Cholesterol-TEG
Inert strand B	TTTATCGCTACCCTTCGC ACAGTCAATCTAGAGAGC CCTGCCTTACGA	Cholesterol-TEG	-
receptor back-bone	TCGTAAGGCAGGGCTCTC TAGACAGGGCTCTCTGAA TGTGACTGTGCGAAGGTG ACTGTGCGAAGGGTAGCG ATTTT	Cholesterol-TEG	-
receptor	TTTATCGCTACCCTTCGC ACAGTCACCTTCGCACAG TCACATTCAGAGAGCCCT GTCTAGAGAGCCCTGCCT TACGA-*sticky end*	Cholesterol-TEG	Cy3

mum signal of $k = 6$ of the same sticky end. After the acquisition of the nanostar adsorption in equilibrium, the acquired signal is corrected and normalized yielding the binding probability:

$$\Theta = \frac{I - I_{\text{back}}}{I_{\text{max}} - I_{\text{back}}}. \tag{4.10}$$

For the image processing we used a combination of ImageJ and python. FRAP measurements revealed the binding kinetics of the nanostar adsorption. The acquired data was normalised with respect to the initial intensity before bleaching. Furthermore, we corrected for the bleaching of the fluorophores over time.

4.5. ACKNOWLEDGEMENT

We thank Jos Zwanikken for help with the theoretical model and Constant Tellinga for his contribution in the data analysis.

REFERENCES

[1] P. Chien and L. M. Gierasch, *Challenges and dreams: physics of weak interactions essential to life,* Molecular Biology of the Cell **25**, 3474 (2017).

[2] V. LG and C. M, *The role of weak interactions in biological systems: the dual dynamics model,* Journal of theoretical biology **193**, 287 (1998).

[3] A. Gao, K. Shrinivas, P. Lepeudry, H. I. Suzuki, P. A. Sharp, and A. K. Chakraborty, *Evolution of weak cooperative interactions for biological specificity,* Proceedings of the National Academy of Sciences **115**, E11053 (2018).

[4] K. Teilum, J. G. Olsen, and B. B. Kragelund, *On the specificity of protein–protein interactions in the context of disorder,* Biochemical Journal **478**, 2035 (2021).

[5] S. Banjade and M. K. Rosen, *Phase transitions of multivalent proteins can promote clustering of membrane receptors,* eLife **3** (2014).

[6] F. Liu and K. J. Walters, *Multitasking with ubiquitin through multivalent interactions,* Trends in Biochemical Sciences **35**, 352 (2010).

[7] R. J. Goldberg, *A theory of antibody—antigen reactions. i. theory for reactions of multivalent antigen with bivalent and univalent antibody2,* Journal of the American Chemical Society **74**, 5715 (2002).

[8] C. J. Burckhardt and U. F. Greber, *Virus movements on the plasma membrane support infection and transmission between cells,* PLOS Pathogens **5** (2009).

[9] M. Müller, D. Lauster, H. H. Wildenauer, A. Herrmann, and S. Block, *Mobility-based quantification of multivalent virus-receptor interactions: New insights into influenza a virus binding mode,* Nano Letters **19**, 1875 (2019).

[10] M. Delguste, C. Zeippen, B. Machiels, J. Mast, L. Gillet, and D. Alsteens, *Multivalent binding of herpesvirus to living cells is tightly regulated during infection,* Science Advances **4**, eaat1273 (2018).

[11] F. J. Martinez-Veracoechea and D. Frenkel, *Designing super selectivity in multivalent nano-particle binding,* Proceedings of the National Academy of Sciences **108**, 10963 (2011).

[12] A. T. Christy, H. Kusumaatmaja, and M. A. Miller, *Control of superselectivity by crowding in three-dimensional hosts,* Physical Review Letters **126**, 028002 (2021).

[13] T. Curk and N. B. Tito, *First-order 'hyper-selective' binding transition of multivalent particles under force,* Journal of Physics Condensed Matter **32** (2020).

[14] G. V. Dubacheva, T. Curk, R. Auzély-Velty, D. Frenkel, and R. P. Richter, *Designing multivalent probes for tunable superselective targeting,* Proceedings of the National Academy of Sciences **112** (2015).

[15] G. V. Dubacheva, T. Curk, B. M. Mognetti, R. Auzély-Velty, D. Frenkel, and R. P. Richter, *Superselective targeting using multivalent polymers,* Journal of the American Chemical Society **136**, 1722 (2014).

[16] N. J. Overeem, P. H. E. Hamming, M. Tieke, E. van der Vries, and J. Huskens, *Multivalent affinity profiling: Direct visualization of the superselective binding of influenza viruses,* ACS Nano **15**, 8525 (2021).

[17] R. Lanfranco, P. K. Jana, L. Tunesi, P. Cicuta, B. M. Mognetti, L. D. Michele, and G. Bruylants, *Kinetics of nanoparticle-membrane adhesion mediated by multivalent interactions,* Langmuir **35**, 2002 (2019).

[18] C. Linne, D. Visco, S. Angioletti-Uberti, L. Laan, and D. J. Kraft, *Direct visualization of superselective colloid-surface binding mediated by multivalent interactions,* Proceedings of the National Academy of Sciences **118**, e2106036118 (2021).

[19] M. R. W. Scheepers, L. J. van IJzendoorn, and M. W. J. Prins, *Multivalent weak interactions enhance selectivity of interparticle binding,* Proceedings of the National Academy of Sciences **10**, 202003968 (2020).

[20] O. M. Szklarczyk, N. González-Segredo, P. Kukura, A. Oppenheim, D. Choquet, V. Sandoghdar, A. Helenius, I. F. Sbalzarini, and H. Ewers, *Receptor concentration and diffusivity control multivalent binding of sv40 to membrane bilayers,* PLOS Computational Biology **9**, e1003310 (2013).

[21] N. Conrad, T. Kennedy, D. K. Fygenson, and O. A. Saleh, *Increasing valence pushes dna nanostar networks to the isostatic point,* Proceedings of the National Academy of Sciences of the United States of America **116**, 7238 (2019).

[22] R. A. Brady, W. T. Kaufhold, N. J. Brooks, V. Foderà, and L. D. Michele, *Flexibility defines structure in crystals of amphiphilic dna nanostars,* Journal of Physics: Condensed Matter **31**, 074003 (2019).

[23] S. Biffi, R. Cerbino, F. Bomboi, E. M. Paraboschi, R. Asselta, F. Sciortino, and T. Bellini, *Phase behavior and critical activated dynamics of limited-valence dna nanostars,* Proceedings of the National Academy of Sciences **110**, 15633 (2013).

[24] S. A. V. D. Meulen, G. V. Dubacheva, M. Dogterom, R. P. Richter, and M. E. Leunissen, *Quartz crystal microbalance with dissipation monitoring and spectroscopic ellipsometry measurements of the phospholipid bilayer anchoring stability and kinetics of hydrophobically modified dna oligonucleotides,* Langmuir **30**, 6525 (2014).

[25] M. Rinaldin, R. W. Verweij, I. Chakraborty, and D. J. Kraft, *Colloid supported lipid bilayers for self-assembly,* Soft Matter **15**, 1345 (2019).

[26] I. Chakraborty, V. Meester, C. van der Wel, and D. J. Kraft, *Colloidal joints with designed motion range and tunable joint flexibility,* Nanoscale **9**, 7814 (2017).

[27] M. Liu, A. Apriceno, M. Sipin, G. Battaglia, and S. Angioletti-uberti, *A game of entropy : range selective binding in multivalent constructs,* Nature Communications **11**, 1 (2020).

[28] X. Qiu, K. Andresen, L. W. Kwok, J. S. Lamb, H. Y. Park, and L. Pollack, *Inter-dna attraction mediated by divalent counterions,* Physical Review Letters **99**, 038104 (2007).

[29] Z. Zhang, Y. Wu, K. Xi, J. Sang, and Z. Tan, *Divalent ion-mediated dna-dna interactions: A comparative study of triplex and duplex,* Biophysical Journal **113**, 517 (2017).

[30] P. Aich, S. L. Labiuk, L. W. Tari, L. J. Delbaere, W. J. Roesler, K. J. Falk, R. P. Steer, and J. S. Lee, *M-dna: a complex between divalent metal ions and dna which behaves as a molecular wire,* Journal of Molecular Biology **294**, 477 (1999).

[31] T. Curk, J. Dobnikar, and D. Frenkel, *Design Principles for Super Selectivity using Multivalent Interactions* (John Wiley & Sons, Ltd, 2018) pp. 75–101.

[32] R. Phillips, J. Kondev, J. Theriot, H. G. Garcia, and N. Orme, *Physical biology of the cell,* Physical Biology of the Cell (2012).

[33] L. Parolini, J. Kotar, L. D. Michele, and B. M. Mognetti, *Controlling self-assembly kinetics of dna-functionalized liposomes using toehold exchange mechanism,* ACS Nano **10**, 2392 (2016).

5

PRELIMINARY WORK AND CONCLUSION

In this thesis we have presented two experimental model systems to study superselective surface targeting and multivalency on the micro- and molecular scale. We visualized the dynamic picture of superselective binding, resulting from weak ligand and receptor interactions. We used DNA molecules as a ligand and receptor system, which provided high experimental control over interaction strength and number of binding sites. However, we noticed that DNA does not only function as a specific receptor, but may also change membrane properties due to its cholesterol anchor. Here, we show preliminary results on how the presence of additional biomolecules integrated in the membrane via a cholesterol anchor can influence membrane fluidity. In addition, we investigate how the diffusion of receptors changes after the adsorption of nanostars and if we can link the number of bound arms to the consequent diffusion coefficient. Lastly, we will end this thesis with conclusive remarks and suggestions for future experiments.

5.1. PRELIMINARY RESULTS

5.1.1. INTRODUCTION

A complex cell membrane structure regulates a cell's function [1, 2]. Typically, self-assembly of phospholipids gives the membrane its unique structure and fluidic properties [3–5]. Membrane fluidity provides full lateral mobility of molecules that are anchored in the cell membrane, which is essential for cell-cell adhesion [6, 7], signalling pathways [8–10] and transport along the cell surface [11–13]. The initiation of cellular processes often results from receptor clustering in the membrane [14] and the accumulation of receptors emerges from ligand binding [15], and can induce liquid-liquid phase separation [16]. Since receptor diffusion governs many biological processes, it is important to understand the impact factors on receptor mobility in the membrane.

To assess the diffusion coefficient of membrane embedded objects theoretically, the Saffman-Delbrueck model gives insights in the physical parameters that are relevant for diffusion inside the membrane [17]. The model approximates the integrated object as a cylinder and demonstrates that the membrane viscosity and the object's radius determine the diffusion of the object. In agreement with the model, experiments have shown that the lateral diffusion of proteins changes with increasing protein concentration [18]. Furthermore, the addition of cholesterol molecules stiffens the membrane with increasing cholesterol concentration until the membrane looses its fluidity completely [19–21]. The addition of cholesterol to a membrane causes the lipids to pack more closely and therefore restrict their motion [22]. Moreover, the diffusion of the receptor changes drastically after binding to a multivalent object [23]. After binding, receptor mediated diffusion of a multivalently bound particle depends on the diffusion of the receptor cluster, which is larger in size compared to an individual receptor and therefore slows down the receptor diffusion. The Saffman-Delbrueck model predicts $D \approx 1/\ln(\text{biomolecule radius})$. But experiments with proteins have shown that the diffusion of biomolecules in crowded environments drastically slow down [24] and the diffusion scales $D \approx 1/(\text{biomolecule radius})$ [11, 25] in a crowded environment. Throughout this thesis, we found indications that a locally high density of membrane anchored DNA changes the diffusion of the DNA. In chapter 2, the reversibility of the DNA-DNA interactions in the densely packed colloid patch area was drastically slowed down for strong interactions. The stronger the interactions, the more DNA linkers are recruited towards the patch (see chapter 3). A possible explanation for this observation is the increased concentration of cholesterol in the patch area that stiffens the membrane and therefore slows down the DNA linkers. However, a reduced diffusion of DNA linkers in the patch has been also observed for anchored DNA via a stearyl anchor [21]. Another possible explanation is the increased effective size of the receptor as a result of the cluster formation and hence leading to a reduced diffusion.

To study the change in receptor diffusion in association with membrane viscosity, receptor cluster and additional biomolecules in the membrane, we employ membrane embedded receptors using supported lipid bilayers (SLB) functionalized with double stranded deoxyribonucleid acid (dsDNA) molecules [26]. Important for these experiments is a strong anchoring of a DNA strand into a supported lipid bilayer (SLB) that simultaneously grants mobility [27].

To measure the diffusion of unbound and bound dsDNA in a supported lipid bilayer

(SLB), we study fluorescently labelled dsDNA with a single stranded overhang (sticky end), modified with a double cholesterol anchor. Additional molecules in the membrane that do not contribute to binding are mimicked by a 47 bp inert dsDNA without a sticky end but also a double-cholesterol anchor for the integration in the SLB. The dsDNA in the SLB (receptor) can freely diffuse and bind to a multivalent ligand. Here, we use DNA nanostars as the multivalent ligand to study the change in receptor diffusion after binding. This study seeks to address the following questions: Do additional inert strands, also anchored with a double cholesterol anchor, reduce the diffusion of linkers? How does ligand binding affect the mobility of linkers in the membrane?

Another open question is whether we can derive for a multivalently bound particle the number of receptor and ligand interactions from a change in diffusion coefficient.

5.1.2. RESULTS

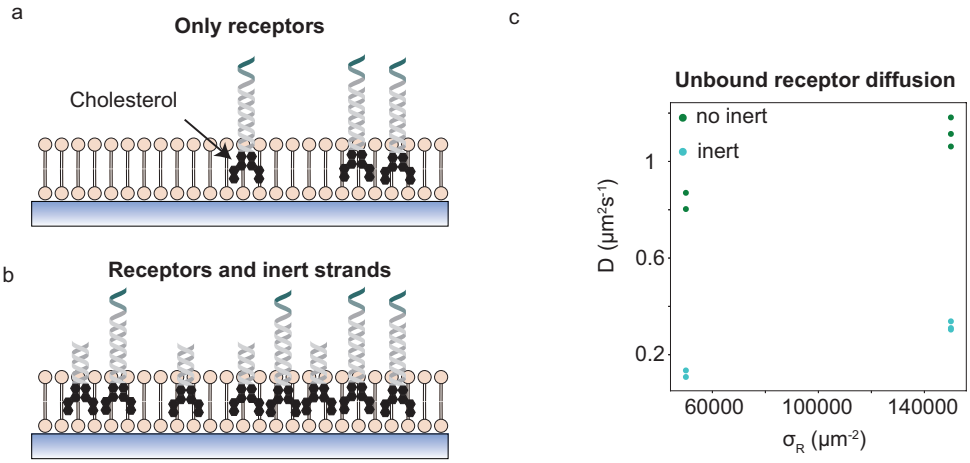

Figure 5.1: **Unbound receptor diffusion.** A double cholesterol anchor integrates receptors (a) and inert strands (b) into a supported lipid bilayer (SLB). Fluorescent recovery after photobleaching (FRAP) measurements provide insights in the timescale τ of signal recovery after bleaching the fluorophores on the receptors. Together with Eq. 5.2 we measured the diffusioncoefficient D for unbound receptors for surfaces with and without inert strands.

Unbound receptor diffusion in a supported lipid bilayer To assess how receptor diffusion changes with the density of receptors and inert strands embedded in a supported lipid bilayer (SLB) we use double stranded DNA (dsDNA) with a double-cholesterol anchor integrated in a DOPC lipid bilayer, see Fig. 5.1a-b. Here, the receptors are 77 bp dsDNA with a 6bp sticky end and inert strands consist of 47bp dsDNA. Each receptor carries a fluorophore that allows for the direct visualisation with fluorescent microscopy. We measure the diffusion coefficient D of receptors at different receptor densities σ_R and, additionally, with different inert strand densities. In the following, we compare D of a system with and without inert strands to quantify the impact of cholesterol and the presence of the inert strand on D.

First, we determine D of receptors at $\sigma_R = 50000\ \mu\text{m}^{-2}$ and $\sigma_R = 150000\ \mu\text{m}^{-2}$. To do

so, we prepared the DNA functionalized SLB in a flow channel as described in chapter 4. In order to measure D, repeated measurements of fluorescent recovery after photobleaching (FRAP) experiments were performed. The characteristic time τ governs the fluorescent signal recovery after photobleaching [28]:

$$I_{\text{norm}} = A(1 - \exp^{t/\tau}), \tag{5.1}$$

where A is a constant that accounts for incomplete recovery and t is the time after bleaching. I_{norm} is the detected signal normalised with respect to the intensity before bleaching. A fit with Eq. 5.1 yields τ and together with the radius r of the bleached area, we obtain [28]:

$$D = \frac{r^2}{4 * \tau}. \tag{5.2}$$

Fig. 5.1c reports D as a function of σ_R. The different datapoints represent different field of views in the same sample. The receptor diffusion without inert strands ranges between 0.8 μm^2/s and 1.2 μm^2/s. The results agree with studies that measure protein diffusion in DOPC lipids, where they showed that the addition of proteins can decrease the DOPC diffusion by tenfold compared to free lipid diffusion [18]. The small increase in D with increasing σ_R contradicts previous findings that an increase in cholesterol decreases D. However, we expect a standard deviation of approximately 0.5 μm^{-2}/s based on further experiments in this chapter (see Fig. 5.2). Therefore, the increase lies within the experimental error and is most likely not significant. But, taking the estimated experimental error into account, these findings indicate that a three fold increase of cholesterol does not change the receptor diffusion significantly. Cholesterol concentrations up to 20mol% double membrane viscosity [22]. We used 10mol% and 20mol% of cholesterol in the DOPC membrane corresponding to low and high σ_R respectively. In this range of cholesterol mol%, we would still expect a change in the membrane viscosity and therefore a decrease in D, which we do not observe in Fig. 5.1c. However, please note that it is not possible to draw a strong conclusion from the data because the sample size is too small. Further experiment with the addition of cholesterol molecules at constant receptor density can give insights in the contribution of cholesterol to the receptor diffusion. In addition to cholesterol, any additional biomolecules embedded in the membrane can decrease the diffusion of receptors due to crowding. Next, we investigate how the receptor diffusion changes with additional inert strands in the SLB.

Many biomolecules with different functions are part of the cell membrane. Here, we use inert strands to mimic biomolecules without a function to investigate the receptor diffusion in the presence of additional molecules embedded in the SLB. We kept the overall DNA density constant at 300000 μm^{-2}, which means that at σ_R = 50000 μm^{-2}, the SLB contains 50000 μm^{-2} receptors and 250000 μm^{-2} inert strands, which corresponds to 60mol% of cholesterol in the SLB. FRAP measurements together with Eq. 5.1 and Eq. 5.2 evaluate D for different field of views. The resulting D varies between 0.1 μm^2/s and 0.3 μm^2/s, see Fig. 5.1c. Interestingly, D increases with increasing σ_R similarly to the surfaces without inert strands, see Fig. 5.1c. But again, we expect the increase with increasing σ_R to lie within the experimental error. Furthermore, a change in σ_R should not change D because the overall cholesterol density is constant.

A comparison between the two systems shows that surfaces with inert strands show lower D than surfaces with only receptors. A study with 1,2-Dipalmitoyl-d_{63}-*sn*-glycero-3-phosphocholine (DPPC-d_{62}) revealed that at room temperature, the diffusion of DPPC ranges between $(1-2)\ \mu m^2/s$ for 20mol% - 50mol% cholesterol [29]. Because after the addition of inert strands, we change the membrane composition from 20mol% cholesterol to 60mol% cholesterol, the change in D results from the additional cholesterol molecules. Another explanation for the change in D is that the inert strands lead to a denser membrane composition of biomolecules and therefore decrease receptor diffusion due to steric hindrances [30]. Experimental and theoretical studies with proteins embedded in a membrane showed up to a tenfold decrease of protein diffusion in crowded membranes [18].

Taken together, these results provide insights into receptor diffusion in the presence of cholesterol embedded in the membrane and inert strands. To disentangle the impact of cholesterol and crowding effects on receptor diffusion further experiments are needed. A systematic measurement of receptor diffusion in the presence of different cholesterol concentrations can provide insights how cholesterol influences receptor diffusion. To avoid the effect of cholesterol on the membrane, inert strands and receptors anchored with a double-stearyl anchor [21] are a useful tool to study diffusion coefficients in crowded environments without altering the membrane viscosity. Altogether, we showed that the addition of biomolecules and cholesterol change the receptor diffusion. Next, we investigate how the binding of multivalent nanostars change receptor diffusion, while keeping the membrane composition constant.

Receptor diffusion after nanostar binding As was mentioned in chapter 4, nanostars bind with a varying number of arms to receptors, depending on σ_R and the interaction strength. However, our measurements did not conclusively show how many arms were bound due to practical constraints. Here, we propose another method to quantify the average number of bound arms $\langle n \rangle$ by measuring the change in receptor diffusion D before and after binding to an in-this-case trivalent nanostar. These findings help us link measured diffusion coefficients of multivalent particles to the number of bound arms, or, in other words interaction sites with the membrane.

We hypothesize that the adsorption of a multivalent nanostar changes the diffusion of receptors in the SLB substantially. These nanostars were first introduced in Chapter 4 and consist of a fluorescently labelled star shaped nanostructure with three arms, each featuring a sticky end that interacts with the receptors on the SLB (see more detailed information Materials and Methods in Chapter 4). This section examines the change in D after freely diffusing unbound receptors bind via their sticky end to a multivalent nanostar. In doing so, we prepared three samples with fluorescently labelled surface mobile receptors with 6 bp, 8 bp and 11 bp sticky ends with $\sigma_R = 100000\ \mu\text{m}^{-2}$ (see more detailed information Materials and Methods in Chapter 4). To assess the change in D, we first measured D for the unbound receptors and again after adding trivalent DNA nanostars to the solution.

To assess D, we performed repeated FRAP measurements on the receptors for different lengths of sticky ends, as described previously. With Eq.5.1 and Eq. 5.2 we extracted D. Fig. 5.2a presents D as a function of the sticky end, averaged over three field of views

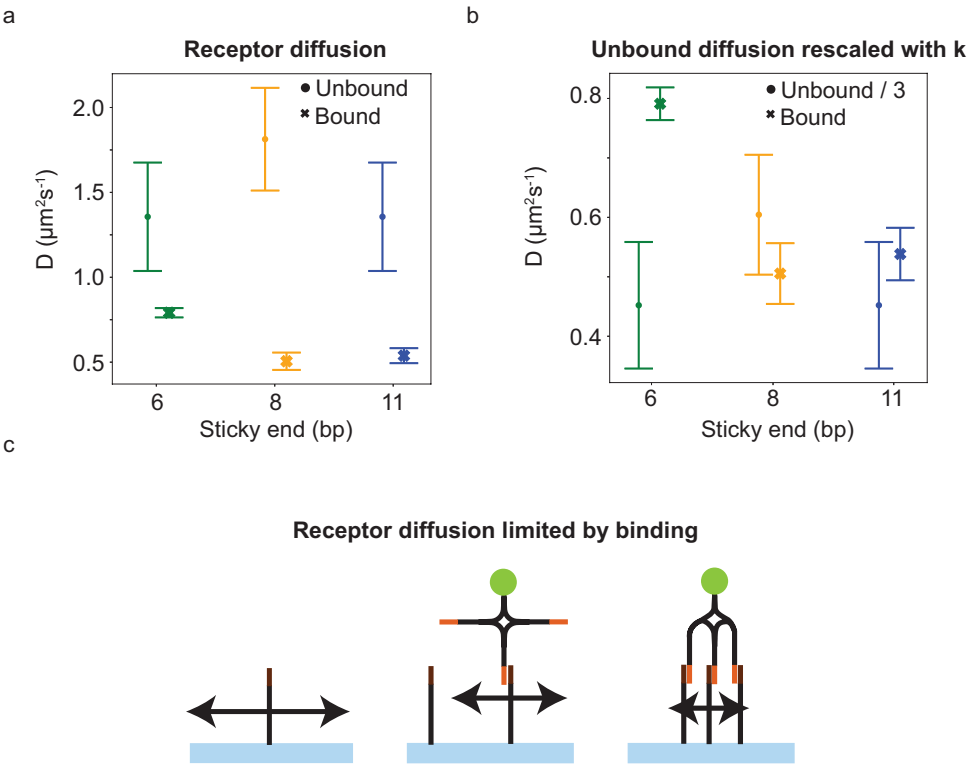

Figure 5.2: **Receptor diffusion after nanostar adsorption.** a) Receptor diffusion D of unbound and bound receptors. The bound receptors interact with trivalent nanostars for 6 bp, 8 bp and 11 bp sticky ends at σ_R = 100000 μm^{-2} and nanostar concentration $\rho = 10^{-7}$ M. b) Unbound receptor diffusion divided by $k = 3$ to evaluate if D after binding to a trivalent nanostar scales with the valency k. c) Ligand binding to receptors slows down the receptor diffusion. Furthermore, the number of receptor and nanostar interactions governs D.

within one sample. From the Figure we can see that unbound receptors show approximately the same D, independent of the sticky end. This finding indicates that the sticky end does not influence D, at least not for such short variations in lengths as were employed here. Next, we investigate D after adding trivalent nanostars to the system.

As was shown in chapter 4, at $\sigma_R = 100000$ μm^{-2} nanostars bind with a high binding probability to the surface. Each nanostar can bind with at least 1 arm and maximum the total number of arms, depending on the interaction strength. The total binding strength of the nanostar is therefore the interplay between interaction strength of one arm and how many arms are bound. To assess the binding strength, it is therefore important to measure the number of arms because the interaction strength is the enthalpy of the sticky end, which can be estimated via Santalucia's nearest neighbour rule [31]. Here, we hypothesize that D gives insight into the average number of bound arms $\langle n \rangle$. To study D_{bound} of bound receptors, we add trivalent nanostars to the system and let it equilibrate. Next, we performed FRAP measurements and extracted D for three different sticky ends as presented in Fig. 5.2a. What is interesting in this data is that after

adding nanostars to the receptors, D decreases significantly for all different sticky ends. This observation indicates that the nanostar-receptor interaction reduce receptor diffusion after binding. Moreover, there are also differences in the ratios between D_{bound} and D_{unbound} for the different sticky ends, namely the D for the 6 bp is decreased two-fold, whereas D for the 8 bp and 11 bp are reduced by a factor of three. The results indicate that the nanostars bind to the receptors and hence restrict their motion in the SLB as predicted by the Saffman-Delbrueck model. The addition of nanostars to the 6 bp receptors has the least effect on D, indicating that less receptors are bound to nanostars. This observation raises the question about $\langle n \rangle$, which we will discuss next.

The result of the 6 bp sticky end might suggest that the number of bonds between linker receptors and nanostars varies between the sticky ends, although all nanostars have the same number of arms. The interaction between multiple arms results in local clusters of receptors and therefore an increase in size scaling with the number of receptors that form the cluster. Assuming $D \approx 1/(\text{biomoleculeradius})$, we expect $D \approx 1/(\langle \text{n} \rangle * \text{receptorradius})$. To test this prediction, we first rescale the y-axis in Fig. 5.2a with the maximum number of bonds by dividing D_{unbound} by the valency $k = 3$ for all sticky ends, see Fig. 5.2b. The rescaling revealed an overlap of the data for the 8 bp and 11 bp sticky ends, whereas $D_{\text{unbound}}/3$ of the 6 bp receptor does not agree with D_{bound}. A possible explanation for these results is that the 8 bp and 11bp bind to three receptors simultaneously and that the weaker nanostar binds with less arms. To achieve an overlap of D for the 6 bp, the unbound D has to be rescaled with 2. We just suggest that $< n > \approx 2$ for 6 bp at $\sigma_R = 100000\ \mu\text{m}^{-2}$. Furthermore, the 6 bp receptor binds more weakly and therefore more likely unbinds compared to the 8 bp and 11 bp. It is tempting to compare this finding with chapter 4 Fig. 2f, where we derived $\langle n \rangle$ from the binding probability Θ. Unfortunately, at $\sigma_R = 100000\ \mu\text{m}^{-2}$, we cannot assess $\langle n \rangle$ due to deviations of the model from the experimental data. It is thus important to include another method to evaluate $\langle n \rangle$.

In this section, we confirmed the hypothesis that the adsorption of multivalent nanostars to a surface with mobile linker receptors reduces their diffusive motion to a certain extent. Overal the results indicate that receptor diffusion after binding to a multivalent particle scales with the number of interactions between receptors and particle, see Fig. 5.2c. Knowing the relation between number of interactions and D after ligand adsorption gives insights in biological processes that lead to receptor accumulation after ligand binding [15] and subsequent lateral diffusion of the surface bound particle as it has been reported for virus-host adhesion [32, 33]. This section has presented an additional method to evaluate the number of interactions in multivalent adhesion from the diffusive motion of receptors. Apart from looking at receptor diffusion, we wonder if studying the adsorbed nanostars directly gives insights into the number of interactions between nanostar and linker receptor, which we will address in the next section.

Bound nanostar surface diffusion Lateral diffusion along the cell membrane is an important feature for cellular processes and virus-host invasion. To diffuse on the cell membrane, the particle needs to bind strongly to the receptors. But typically, the interactions in biological systems are weak and reversible. It is thus interesting to understand how the valency and interaction strength of a multivalent particle allows for lateral dif-

fusion. The aim of this section is to investigate how receptor diffusion in a membrane changes with external factors like crowding, change in membrane viscosity and receptor clustering after multivalent binding.

To assess D of the surface bound nanostars, we use the same method as previously introduced in chapter 4. FRAP reveals the diffusion D of membrane bound nanostars and importantly it additionally shows the reversible binding. We measured trivalent nanostars with 6 bp, 8 bp and 11 bp sticky ends at $\sigma_R = 150000\ \mu\text{m}^{-2}$. FRAP results, as illustrated in Fig. 5.3a-c present a fluorescent image after 112 s after bleaching the area encircled in white. There is a significant difference in the amount of recovery for the three different length of sticky ends: The 6 bp and 8 bp are fully recovered, whereas the 11 bp sticky end shows very little recovery, even after 300 s, see Fig. 5.3d. These images indicate that the binding kinetics differ significantly between the length of the sticky end: The 6 bp and 8 bp dynamically exchange bound and unbound naostars, whereas nanostars with 11 bp do not leave the surface anymore after binding. To quantify the reversibility further, we focus on the signal recovery without membrane diffusion in the following.

Please note, a limitation of this experimental setup is the differentiation between binding kinetics and membrane diffusion that cause the signal recovery after photobleaching. To exclude the signal recovery resulting from membrane bound nanostars, we extract the intensity signal $I(10s)$ after 10 s, as it was introduced in chapter 4, in a small region inside the bleached area (red dashed circle in Fig. 5.3a). The results obtained from the initial FRAP signals are reported in Fig. 5.3e. The higher $I(10s)$, the faster the nanostars unbind receptors and unbleached nanostars bind to the surface. We observe a clear trend of decreasing $I(10s)$ with increasing receptor density for all different sticky ends. The differences in $I(10s)$ with a change in σ_R can be explained by different number of interactions between nanostars and receptors. The larger σ_R, the larger the average number of bound arms $\langle n \rangle$, as we have pointed out in chapter 4. An increase in $\langle n \rangle$ results in a longer residence time of the nanostar on the surface before it unbinds, hence the slow signal recovery. Interestingly, the 6 bp unbinds and binds faster compared to the 8 bp and 11 bp and confirms our observations in chapter 2, where we evaluated the binding kinetics in the patch. Furthermore, the 8 bp and 11 bp sticky ends show no recovery in the first 10s for $\sigma_r > 10^4\ \mu\text{m}^{-2}$. This observation suggests that the adsorbed nanostars do not detach from the surface anymore. Additionally, from this data we see that the 6 bp sticky end always shows a recovery, indicating that it still unbinds and rebinds even at high σ_r. These findings further support the idea that the average number of bound arms $\langle n \rangle$ is smaller for a 6 bp trivalent nanostar compared to the 8 bp and 11 bp. Because the 6 bp binds with weaker bonds, we expect $\langle n \rangle$ to be the lowest. This raises the question whether we can assess $\langle n \rangle$ in an irreversible system by evaluating D of surface bound nanostars, which will be discussed in the next section.

To further quantify the diffusive behavior of irreversible adsorbed nanostars, we extracted D for different σ_R of the fully bleached area for the 11 bp sticky end (white dashed circle in Fig.5.3c). From this data, we see that D decreases with increasing σ_R. Interestingly, it appears that $D \propto \log(\sigma_R)$. It seems possible that these results are due to an increase in number of bonds between an individual nanostar and linker receptor, leading to a decrease in D. In contrast to earlier findings, however, we expect the max-

imum number of bonds already being fully established at approximately 10^4 μm^{-2}, see Fig. 5.3e. Another possible explanation is that the increase of the number of nanostars on the surface reduces D. Studies on protein diffusion on membranes reported that an increase in protein concentration on the membrane leads to increasing steric interactions and hence reduces the lateral diffusion [12]. We know from the data reported in chapter 4 that an increase in σ_R leads to an increase in the number of nanostars adsorbed to the surface. We thus suggest that they might be closely packed on the surface, significantly restricting the space they can explore, nearly leading to a complete arrest of motion.

This section has demonstrated that reversible nanostar binding depends on the interaction strength as pointed out in chapter 2 and chapter 4. What is interesting is that the adsorption of nanostars leads to increased steric interactions between them that causes a reduction in lateral diffusion.

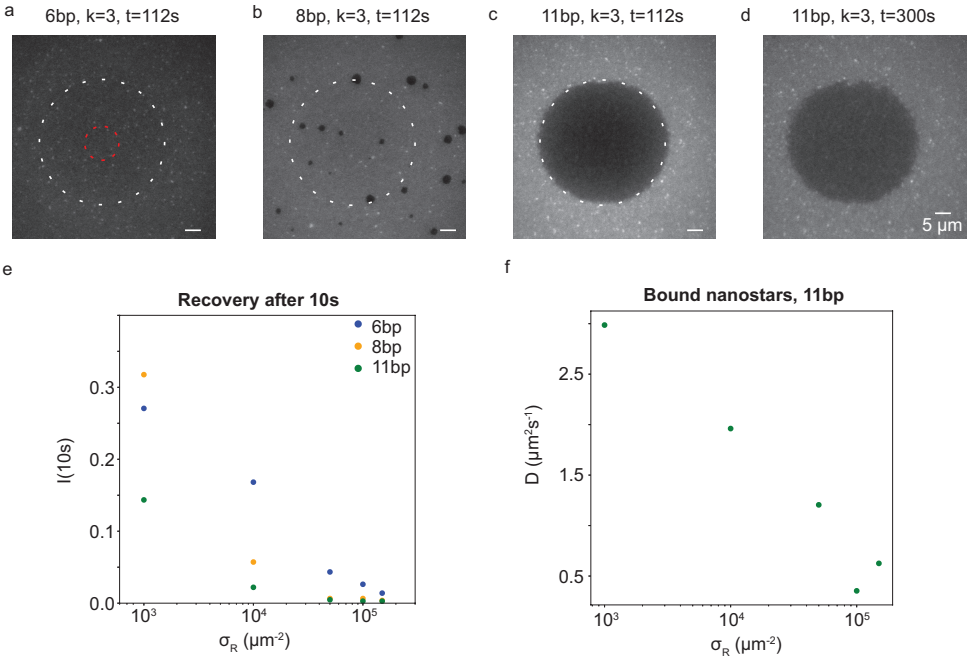

Figure 5.3: **Trivalent nanostar FRAP.** Fluorescent images of trivalent nanostars with 6 bp (a), 8 bp(b) and 11 bp sticky ends after 112 s after photobleaching. d) The same sample as in (c) after 300 s. e) Intensity measured at the centre (red dashed circle in (a)) after 10 s after photobleaching. f) Since the 11 bp trivalent nanostars barely show any dynamic binding and unbinding, we extract D of the whole bleached area (white dashed circle).

5.1.3. CONCLUSION

The main goal of this chapter was to assess multiple questions: First, does the diffusion of receptors depend on the number of embedded molecules in the SLB? Second, can we quantify the number of bonds formed between a multivalent particle by evaluating the diffusion of bound and unbound receptors? And last, what dictates the lateral diffusion of surface bound nanostars?

The investigation of D of the receptors has shown that the presence of passive receptors decreases the diffusive motion drastically. These findings suggest that the DNA packing fraction changes the membrane fluidic property and hence decreases D of the integrated molecules. It remains unclear what the exact mechanism behind the decrease of D is. There is some evidence to suggest that the cholesterol anchor stiffens the membrane [22, 29]. The second major finding was that the adsorption of multivalent nanostars decreases the receptors diffusion. The change in D between bound and unbound receptor strongly depended on the sticky end: The shorter the sticky end, the less severe is the decrease in D after the nanostar adsorption. The relevance of the number of interacting arms and strength during the nanostar adsorption is supported by the FRAP measurements of adsorbed nanostars for different sticky ends. An implication of this is the possibility that the stronger nanostars bind with more arms and the presence of nanostars on the surface restricts their motion due to limited space.

Although the findings are based on a small sample size, it offers insights into the diffusive motion with surface mobile DNA and additionally in multivalent binding on the molecular level. An implication of the change of D in the presence of additional biomolecules in the SLB should be taken into account when building structures with mobile DNA-DNA interactions. The present study confirms previous findings in chapter 4 and provides additional evidence with respect to the average number of bound arms of a nanostar. Further work needs to be done to establish whether the diffusion of receptors scales with the number of interactions with a nanostar. Comparing the change in D before and after binding for different nanostar valencies can give a more detailed understanding.

5.2. CONCLUSION AND OUTLOOK

In this thesis, the aim was to study multivalent binding with a focus on superselective surface targeting. Multivalency defines a system with more than one binding site. In comparison to monovalent binding, a multivalent particle therefore has different possibilities to form a bond. The combination of weak interactions and different ways of binding leads to a sharp response in the binding probability as a function of receptor density, known as superselectivity. The ideal superselective particle does not bind at low receptor densities and at a specific receptor density all superselective particles in solution bind to the receptors. Superselectivity controls biological adhesion processes on different length scales ranging from multidomain proteins to cells. Generally, surface mobile receptors generate binding as a result of receptor accumulation. Frenkel and coworkers proposed the optimal design rules for a superselective system: high valency and weak interactions. To deepen the understanding of superselectivity, we experimentally investigated multivalency with two experimental model systems: DNA functionalized colloidal particles and multibranched DNA nanostars.

The first experimental model system was used to mimic the multivalent nature of cell-cell adhesion. The system consists of DNA functionalized membrane coated colloidal particles that target a supported lipid bilayer functionalized with complementary DNA. This research has shown that weak interactions and a large density of both ligands and receptors increases the selectivity of a system and confirmed the design rules for a superselective system of Frenkel and coworkers [34] and supports the findings of exper-

imental model systems [35–38]. The key aspect of this study is the direct visualization of the DNA-DNA interactions that provides insights in the accumulation of receptors and ligands in the colloid contact area. Previous studies have reported that the multivalent bond results from the recruitment of ligands and receptors [36, 39]. Our experimental model system directly visualizes the dynamic bond formation over time and links the patch size to the colloid motion. A number of studies have examined the diffusion of multivalently bound particles but to date none has made a direct link between the patch size and diffusion [40, 41]. This study has demonstrated, for the first time, that the multivalent bond is a highly dynamic process with constant unbinding and binding of receptors and ligands. Previous research has found that the receptor and ligand density regulate the size of the multivalent patch [42]. Our findings add to existing research by the investigation of different interaction strength and the observation of a decrease of the patch size at large ligand densities. Our study has reviewed superselectivity and multivalent binding on the microscale, including hundreds of interactions. Next, we raised the question how multivalency regulates superselectivity and diffusion on the nanoscale.

Another multivalent experimental model system presented in this thesis is multivalent DNA nanostars that bind to receptors integrated in a supported lipid bilayer on a target surface. A DNA nanostar is a multi branched nanostructure and results from ssDNA hybridization [43]. The choice of DNA sequence allows for unique designs of the nanostars and gives precise control of the number of arms ranging between $1-10$. This is the first study to experimentally assess superselectivity on the nanoscale to mimic virus-cell or multi-domain protein-cell interactions. The importance of weak interactions for superselectivity is also here supported by our findings and again, confirms the theoretical design for superselective targeting [34]. This study provides an exciting opportunity to advance our knowledge on superselectivity with respect to chemical rate constants. One of our major findings is that a superselective system has a low probability of forming the first bond but after the first bond forms it subsequently binds with as many arms possible. From experimental measurements of the binding kinetics, we conclude that weak multivalent interactions tend to bind more strongly compared to strong interactions. So far, no study has elaborated on the strength of a multivalent bond. The number of interactions are crucial for the strength of a multivalent bond and despite its exploratory nature, the study in chapter 5 provides useful insights in the receptor mediated diffusion with only few interactions and related the receptor cluster diffusion to the number of interactions.

A comparison between the two experimental systems highlights the different behavior due to the length scales ranging from nanometer to micrometer. Each system advances our knowledge of superselectivity from a different view. On the microscale, hundreds of interactions form the multivalent bond between the particle and target surface. This large number of interactions provides many different ways of binding and therefore contributes significantly to the entropy that is important for superselectivity. On the nanoscale, however, only few interactions bind the particle to the target. Hence, the interactions need to be much weaker compared to a system with more interaction sites. That is also what we observed: The colloidal system expressed superselectivity with enthalpies around $-17\ k_BT$, whereas DNA nanostars needed much weaker interactions of $-7\ k_BT$. This remarkable difference in enthalpy stems from the large entropic contri-

bution in the colloidal system. Furthermore, the length scale of the systems dictate the influence of additional parameters like salt contribution, gravitation or ligand flexibility. Because the number of interactions are much lower for the nanostars, additional parameters like salt, inert strands and arm flexibility contribute stronger to the adsorption properties.

Alltogether, this thesis has provided key insights in the superselective targeting of multivalent particles on the nano- and microscale. The key strength of these experimental systems are the direct visualization of the multivalent binding and the high control of valency, interaction strength and particle concentration. It would be interesting to assess the effect of steric repulsion by adding inert strands that are longer compared to receptors. Introducing steric repulsion lowers the effective binding strength of the particle and therefore increase the selectivity. A further study with the DNA nanostars could assess the impact of different types of ligands and receptors on superselectivity [44]. An implication of these findings is that both weak interactions and a high valency should be taken into account in the self-assembly of higher order structures or the design of targeted drug-delivery platforms, where a high selectivity and strong interaction is desired.

REFERENCES

[1] G. Vereb, J. Szöllosi, J. Matkó, P. Nagy, T. Farkas, L. Vígh, L. Mátyus, T. A. Waldmann, and S. Damjanovich, *Dynamic, yet structured: The cell membrane three decades after the singer-nicolson model,* Proc Natl Acad Sci USA **100**, 8053 (2003).

[2] P. L. Yèagle, *Lipid regulation of cell membrane structure and function,* The FASEB Journal **3**, 1833 (1989).

[3] S. J. Singer and G. L. Nicolson, *The fluid mosaic model of the structure of cell membranes,* Science **175**, 720 (1972).

[4] B. Dzikovski and J. H. Freed, *Membrane fluidity,* Wiley Encyclopedia of Chemical Biology , 1 (2008).

[5] A. Cossins, *Membrane fluidity in biology, vol. 4, cellular aspects,* International Journal of Radiation Biology and Related Studies in Physics, Chemistry and Medicine **50**, 756 (1986).

[6] V. M. Braga, *Cell–cell adhesion and signalling,* Current Opinion in Cell Biology **14**, 546 (2002).

[7] L. Shapiro, A. M. Fannon, P. D. Kwong, A. Thompson, M. S. Lehmann, G. Gerhard, J. Als-Nielsen, J. Als-Nielsen, D. R. Colman, and W. A. Hendrickson, *Structural basis of cell-cell adhesion by cadherins,* Nature **374**, 327 (1995).

[8] J. F. Hancock and R. G. Parton, *Ras plasma membrane signalling platforms,* Biochemical Journal **389**, 1 (2005).

[9] M. Cebecauer, M. Spitaler, A. Sergé, and A. I. Magee, *Signalling complexes and clusters: functional advantages and methodological hurdles,* Journal of Cell Science **123**, 309 (2010).

[10] D. Bray, M. D. Levin, and C. J. Morton-Firth, *Receptor clustering as a cellular mechanism to control sensitivity,* Nature **393**, 85 (1998).

[11] S. Ramadurai, A. Holt, V. Krasnikov, G. V. D. Bogaart, J. A. Killian, and B. Poolman, *Lateral diffusion of membrane proteins,* Journal of the American Chemical Society **131**, 12650 (2009).

[12] K. Jacobson, A. Ishihara, and R. Inman, *Lateral diffusion of proteins in membranes,* Ann. Rev. Physiol **49**, 163 (1987).

[13] P. Dragsten, P. Henkart, R. Blumenthal, J. Weinstein, and J. Schlessinger, *Lateral diffusion of surface immunoglobulin, thy-1 antigen, and a lipid probe in lymphocyte plasma membranes.* Proceedings of the National Academy of Sciences of the United States of America **76**, 5163 (1979).

[14] N. Kotani, J. Gu, T. Isaji, K. Udaka, N. Taniguchi, and K. Honke, *Biochemical visualization of cell surface molecular clustering in living cells,* Proceedings of the National Academy of Sciences **105**, 7405 (2008).

[15] B. R. Caré and H. A. Soula, *Impact of receptor clustering on ligand binding,* BMC Systems Biology **5**, 1 (2011).

[16] Q. Xiao, C. K. McAtee, and X. Su, *Phase separation in immune signalling,* Nature Reviews Immunology 2021 , 1 (2021).

[17] P. G. Saffman and M. Delbrueck, *Brownian motion in biological membranes,* Proceedings of the National Academy of Sciences **72**, 3111 (1975).

[18] G. Guigas and M. Weiss, *Effects of protein crowding on membrane systems,* Biochimica et Biophysica Acta (BBA) - Biomembranes **1858**, 2441 (2016).

[19] R. A. Cooper, *Influence of increased membrane cholesterol on membrane fluidity and cell function in human red blood cells,* Journal of Supramolecular Structure **8**, 413 (1978).

[20] S. Kaddah, N. Khreich, F. Kaddah, C. Charcosset, and H. Greige-Gerges, *Cholesterol modulates the liposome membrane fluidity and permeability for a hydrophilic molecule,* Food and Chemical Toxicology **113**, 40 (2018).

[21] I. Chakraborty, V. Meester, C. V. D. Wel, and D. J. Kraft, *Colloidal joints with designed motion range and tunable joint flexibility,* Nanoscale **9**, 7814 (2017).

[22] S. Chakraborty, M. Doktorova, T. R. Molugu, F. A. Heberle, H. L. Scott, B. Dzikovski, M. Nagao, L. R. Stingaciu, R. F. Standaert, F. N. Barrera, J. Katsaras, G. Khelashvili, M. F. Brown, and R. Ashkar, *How cholesterol stiffens unsaturated lipid membranes,* Proceedings of the National Academy of Sciences of the United States of America **117**, 21896 (2020).

[23] G. V. Dubacheva, T. Curk, D. Frenkel, and R. P. Richter, *Multivalent recognition at fluid surfaces: The interplay of receptor clustering and superselectivity,* Journal of the American Chemical Society **141**, 2577 (2019).

[24] H. X. Zhou, *Crowding effects of membrane proteins,* The journal of physical chemistry. B **113**, 7995 (2009).

[25] M. Javanainen, H. Martinez-Seara, R. Metzler, and I. Vattulainen, *Diffusion of integral membrane proteins in protein-rich membranes,* Journal of Physical Chemistry Letters **8**, 4308 (2017).

[26] S. A. V. D. Meulen and M. E. Leunissen, *Solid colloids with surface-mobile dna linkers,* Journal of the American Chemical Society **135**, 15129 (2013).

[27] S. A. V. D. Meulen, G. V. Dubacheva, M. Dogterom, R. P. Richter, and M. E. Leunissen, *Quartz crystal microbalance with dissipation monitoring and spectroscopic ellipsometry measurements of the phospholipid bilayer anchoring stability and kinetics of hydrophobically modified dna oligonucleotides,* Langmuir **30**, 6525 (2014).

[28] F. Pincet, V. Adrien, R. Yang, J. Delacotte, J. E. Rothman, W. Urbach, and D. Tareste, *Frap to characterize molecular diffusion and interaction in various membrane environments,* PLoS ONE **11** (2016).

[29] H. A. Scheldt, D. Huster, and K. Gawrisch, *Diffusion of cholesterol and its precursors in lipid membranes studied by 1h pulsed field gradient magic angle spinning nmr,* Biophysical Journal **89**, 2504 (2005).

[30] M. Löwe, M. Kalacheva, A. J. Boersma, and A. Kedrov, *The more the merrier: effects of macromolecular crowding on the structure and dynamics of biological membranes,* The FEBS Journal **287**, 5039 (2020).

[31] J. SantaLucia, *A unified view of polymer, dumbbell, and oligonucleotide dna nearest-neighbor thermodynamics,* Proceedings of the National Academy of Sciences **95**, 1460 (1998).

[32] M. Müller, D. Lauster, H. H. Wildenauer, A. Herrmann, and S. Block, *Mobility-based quantification of multivalent virus-receptor interactions: New insights into influenza a virus binding mode,* Nano Letters **19**, 1875 (2019).

[33] N. Peerboom, S. Block, N. Altgärde, O. Wahlsten, S. Möller, M. Schnabelrauch, E. Trybala, T. Bergström, and M. Bally, *Binding kinetics and lateral mobility of hsv-1 on end-grafted sulfated glycosaminoglycans,* Biophysical Journal **113**, 1223 (2017).

[34] F. J. Martinez-Veracoechea and D. Frenkel, *Designing super selectivity in multivalent nano-particle binding,* Proceedings of the National Academy of Sciences **108**, 10963 (2011).

[35] M. R. W. Scheepers, L. J. van IJzendoorn, and M. W. J. Prins, *Multivalent weak interactions enhance selectivity of interparticle binding,* Proceedings of the National Academy of Sciences **10**, 202003968 (2020).

[36] R. Lanfranco, P. K. Jana, L. Tunesi, P. Cicuta, B. M. Mognetti, L. D. Michele, and G. Bruylants, *Kinetics of nanoparticle-membrane adhesion mediated by multivalent interactions,* Langmuir **35**, 2002 (2019).

[37] G. V. Dubacheva, T. Curk, R. Auzély-Velty, D. Frenkel, and R. P. Richter, *Designing multivalent probes for tunable superselective targeting,* Proceedings of the National Academy of Sciences **112** (2015).

[38] G. V. Dubacheva, T. Curk, B. M. Mognetti, R. Auzély-Velty, D. Frenkel, and R. P. Richter, *Superselective targeting using multivalent polymers,* Journal of the American Chemical Society **136**, 1722 (2014).

[39] D. D. Iorio, Y. Lu, J. Meulman, and J. Huskens, *Recruitment of receptors at supported lipid bilayers promoted by the multivalent binding of ligand-modified unilamellar vesicles,* Chemical Science **11**, 3307 (2020).

[40] S. Merminod, J. R. Edison, H. Fang, M. F. Hagan, and W. B. Rogers, *Avidity and surface mobility in multivalent ligand-receptor binding,* **13**, 12602 (2021).

[41] S. Block, V. P. Zhdanov, and F. Höök, *Quantification of multivalent interactions by tracking single biological nanoparticle mobility on a lipid membrane,* (2016).

[42] A. McMullen, S. Hilgenfeldt, and J. Brujic, *Dna self-organization controls valence in programmable colloid design,* Proceedings of the National Academy of Sciences **118** (2021).

[43] R. A. Brady, W. T. Kaufhold, N. J. Brooks, V. Foderà, and L. D. Michele, *Flexibility defines structure in crystals of amphiphilic dna nanostars,* Journal of Physics: Condensed Matter **31**, 074003 (2019).

[44] T. Curk, J. Dobnikar, and D. Frenkel, *Optimal multivalent targeting of membranes with many distinct receptors,* Proceedings of the National Academy of Sciences of the United States of America **114**, 7210 (2017).

ACKNOWLEDGEMENTS

I would like to thank my family, friends and colleagues that kept me motivated and supported me to achieve this milestone. First, I would like to thank my supervisors Liedewij and Daniela for giving me the opportunity to work on this interesting topic and for their guidance throughout the last four years. You two make a great team, I very much enjoyed our meetings and scientific discussions with your optimistic and supportive attitude.

I would like to thank my committee members Prof. dr. Daan Frenkel, Dr. Lorenzo Di Michele, Prof. dr. Cees Dekker, Prof. dr. Marileen Dogterom, Dr. Jos Zwanikken and Dr. Marie-Eve Aubin-Tam for their critical assessment of my work.

Parts of this work has been done together with my collaborators Stefano Angioletti-Uberti and Daniele Visco. Thank you both for helping us understand our experimental findings with your theory support and scientific discussions. I would also like to thank Jos Zwanikken for insightful comments and suggestions.

Throughout my PhD I had the pleasure to supervise Laurie, Thijs and Constant. Thank you all for your contribution.

Further, I would like to thank the Laan and Kraft lab. It was great to be part of two labs in Leiden and Delft. Thank you all for the scientific discussions, nice lunch times, coffee breaks and lab-outings. In particular, I am very thankful to Ruben, who showed me how to make DNA functionalized colloids. Ramon, thank you for your lab support and showing me how to pipette on my very first day.

Special thanks go to the support staff. Nadine and Amanda, thank you for helping out in all bureaucratic matters. Jérémie, thanks a lot for your support with microscopy and Anne, thanks for showing me how to make flow channels. Sasha, Susanne, Jan and Anke, thank you for your support to keep the labs running smoothly.

I am very grateful to my friends for their support. Tobi, thank you so much for the beautiful piece of art that you designed for the cover. Samia, thank you for your support and being my paranymph.

Finally, I thank my family for their support and encouragement through all ups and downs during this exciting journey.

CURRICULUM VITÆ

Christine LINNE

02-02-1993 Born in Oldenburg, Germany.

EDUCATION

2005–2011 Secondary school
Felix Klein Gymnasium, Göttingen, Germany

2011–2015 B. Sc. in Physics
Georg August Universität, Göttingen, Germany

2015–2017 M. Sc. in Physics
Georg August Universität, Göttingen, Germany

2017 - 2022 PhD. Physics
Delft University of Technology, the Netherlands
Thesis: To bind or not to bind. DNA mediated multivalent interactions lead to superselectivity
Promotor: Dr. D. J. Kraft
Copromotor: Dr. ir. L. Laan

LIST OF PUBLICATIONS

In this thesis:

1. **C. Linne**, D. Visco, S. Angioletti-Uberti, L. Laan and D. J. Kraft, *Direct visualization of super-selective colloid-surface binding mediated by multivalent interactions*, PNAS **118** (2021).

Other:

1. C.T. Kreis, M. Le BLay, **C. Linne**, M.M. Makowski and O. Bäumchen, *Adhesion of Chlamydomonas microalgae to surfaces is switchable by light*, Nature Phys **14**, 45-49 (2018).

2. M. Rivetti, V. Bertin, T. Salez, C.-Y. Hui, **C. Linne**, M. Arutkin, H. Wu, E. Raphaël and O. Bäumchen, *Elastocapillary levelling of thin viscous films on soft substrates*, Phys. Rev. Fluids **2**, 094001 (2017).